# Chapter 15

# The Precision Magnetic Field: $\omega_p$

In this chapter the requirements and design for the precision magnetic field measurement system are presented, followed by the requirements and procedures for shimming the storage ring magnetic field.

## 15.1 Precision Magnetic Field Measurement

### 15.1.1 Relation between $a_\mu$ and $\omega_p$

In an idealized experiment, the anomaly $a_\mu$ could be extracted by measuring the difference frequency $\omega_a$ between the muon spin $\omega_s$ and cyclotron frequencies $\omega_c$ in a storage ring with a perfectly homogeneous magnetic field $B$ without focusing fields (see Eqn. 3.6):

$$\omega_a = -\frac{Qe}{m_\mu}a_\mu B, \tag{15.1}$$

where $e > 0$ and $Q = \pm 1$. The lab-frame magnetic field $B$ is measured using proton nuclear magnetic resonance (NMR) and expressed in terms of the free proton angular precession frequency $\omega_p$, via $\hbar\omega_p = 2\mu_p|\vec{B}|$. The proton gyromagnetic ratio $\gamma_p \equiv 2\mu_p/\hbar = 2\pi \times 42.577\,4806(10)$ MHz/T [1], so $\omega_p \approx 2\pi \times 61.79$ MHz in the $1.45\,\mathrm{T}$ field. Expressing $B$ in terms of $\omega_p$, the muon anomaly $a_\mu$ is:

$$a_\mu = \frac{\omega_a}{\omega_p}\,\frac{2\mu_p}{\hbar}\,\frac{m_\mu}{e} = \frac{\omega_a}{\omega_p}\,\frac{\mu_p}{\mu_e}\,\frac{m_\mu}{m_e}\,\frac{g_e}{2}, \tag{15.2}$$

using $\mu_e = g_e e\hbar/4m_e$. Experiment E989 will measure $\omega_a/\omega_p$, the additional ratios appearing in Eqn. 15.2 are well known from other experiments: $\mu_e/\mu_p = -658.210\,6848(54)$ (8.1 ppb) [1], $g_e/2 = 1.001\,159\,652\,180\,73(28)$ (0.28 ppt) [2], and $m_\mu/m_e = 206.768\,2843(52)$ (25 ppb) [1] [1]. The latter ratio is extracted using Standard Model theory from the E1054 LAMPF measurement of the ground state hyperfine interval in muonium $\Delta\nu_{\mathrm{Mu}}(\text{E1054}) =$

---

[1]Recently the magnetic moment of the proton was measured with a factor of 3 greater precision [4], which may further reduce the uncertainties in Eqn. 15.2.

$4\,463\,302\,765(53)$ Hz (12 ppb) [3]. The measurement is compared with the SM theoretical prediction to extract $m_e/m_\mu$, which appears as a parameter in the prediction [1] :

$$\Delta\nu_{\mathrm{Mu}}(\mathrm{Th}) \;=\; \frac{16}{3}cR_\infty\alpha^2\frac{m_e}{m_\mu}\left(1+\frac{m_e}{m_\mu}\right)^{-3} + \text{higher order terms.} \qquad (15.3)$$

The theory uncertainty has a 101 Hz (23 ppb) contribution from uncertainty/incompleteness in the theory calculation, but is dominated by the uncertainty in the mass ratio $m_e/m_\mu$. The uncertainties on the Rydberg $R_\infty$ and fine structure constant $\alpha$ (extracted using QED theory from a measurement of $a_e$ [1]) are negligible in comparison. The hyperfine interval is dominated by QED contributions, but there are higher-order corrections including a weak contribution $\Delta\nu_{\mathrm{Weak}} = -65$ Hz from $Z^0$ exchange, a hadronic contribution $\Delta\nu_{\mathrm{Had}} = 236(4)$ Hz, and a hadronic light-by-light contribution of 0.0065 Hz (see references in [1]). Setting $\Delta\nu_{\mathrm{Mu}}(\mathrm{E}1054) = \Delta\nu_{\mathrm{Mu}}(\mathrm{Th})$ determines the mass ratio $(m_\mu/m_e)$ to 25 ppb, but the result is the theory-dependent.

Arguably, the line of arguments above could be broken by new physics that may contribute to $a_\mu$. This new physics might also contribute to $\Delta\nu_{\mathrm{Mu}}$ and must be included for consistency when extracting $m_\mu/m_e$. For instance, given that the difference between $a_\mu^{\mathrm{E}821}$ and $a_\mu^{\mathrm{SM}}$ is roughly twice the weak contribution to $a_\mu$, a comparable new physics contribution to $\Delta\nu_{\mathrm{Mu}}$ would perturb the extracted value of $m_\mu/m_e$ by almost 30 ppb.

To extract a value of $a_\mu$ less dependent on assumptions, note the ratio of muon to electron masses can be expressed as $m_\mu/m_e = (g_\mu/g_e) \times (\mu_e/\mu_\mu)$, so Eqn. 15.2 becomes:

$$a_\mu = \frac{\omega_a}{\omega_p}\frac{\mu_p}{\mu_\mu}(1+a_\mu) \;=\; \frac{\omega_a/\omega_p}{\mu_\mu/\mu_p - \omega_a/\omega_p}. \qquad (15.4)$$

The advantage is that the quantities on the right-hand side are determined experimentally with a minimum of theory. The magnetic moment ratio $\mu_{\mu^+}/\mu_p = 3.183\,345\,24(37)$ was determined to 120 ppb essentially directly by E1054 from muonium Zeeman ground state hyperfine transitions measured in a 1.7 T field [1, 3]. The result is based solely on measured quantities, the validity of the Breit-Rabi Hamiltonian to describe the experiment, and a small (17.6 ppm) bound-state QED correction to the $g$-factor for a muon bound in muonium (where the uncertainty on the correction is sub-ppb). In this approach, $a_\mu$ is extracted solely from measured quantities, but limited by the experimental precision on $\mu_\mu/\mu_p$ of 120 ppb. A more precise, independent measurement of $\mu_\mu/\mu_p$, planned at J-PARC, would be very helpful. Note however, that even in the absence of a new measurement, any BSM theory can be tested against E989 at the 140 ppb level as long the potential BSM contributions to $\Delta\nu_{\mathrm{Mu}}$ are considered simultaneously.

## 15.1.2   Physics Requirement on $\tilde{\omega}_p$

Based on the above approach for $a_\mu$, our goal for the total uncertainty on $\tilde{\omega}_p$ in E989 is $\delta\tilde{\omega}_p \leq 70$ ppb, roughly a factor of 2.5 times smaller than was achieved in E821. Here $\tilde{\omega}_p$ refers to the free proton precession frequency $\omega_p$ weighted by the muon distribution in the storage ring.

## 15.1.3 Design of the E989 Field Measurement System

E989 will largely use the principles and field measurement hardware originally developed at the University of Heidelberg and Yale which were employed successfully in E821 at BNL [7] and E1054 at LANL [3]. The E821 field measurement electronics and the underlying physics are described in [5]. The calibration of the field measurements in terms of the equivalent free proton precession frequency using an absolute calibration probe is described in [6]. Details of the E821 field analysis, systematics, and of the hardware are described in the final E821 paper [7], and in several theses and notes [8, 9, 10, 54].

While E821 achieved an uncertainty $\delta\omega_p \approx 170$ ppb, E989 will have to implement specific changes to the hardware and techniques to reduce the systematic errors to the final goal of $\delta\omega_p \approx 70$ ppb. The E989 field measurement hardware, techniques, and changes from E821 will be discussed in the rest of this chapter.

## 15.1.4 Error budget for the $\omega_p$ measurement

The systematic errors on the field measurement from E821 are listed below in Table 15.1. The last two columns list the uncertainties anticipated for E989 and the sections in this chapter where these uncertainties are discussed in detail.

| Source of uncertainty | R99 [ppb] | R00 [ppb] | R01 [ppb] | E989 [ppb] | Section |
|---|---|---|---|---|---|
| Absolute calibration of standard probe | 50 | 50 | 50 | 35 | 15.4.1 |
| Calibration of trolley probes | 200 | 150 | 90 | 30 | 15.4.1 |
| Trolley measurements of $B_0$ | 100 | 100 | 50 | 30 | 15.3.1 |
| Interpolation with fixed probes | 150 | 100 | 70 | 30 | 15.3 |
| Uncertainty from muon distribution | 120 | 30 | 30 | 10 | 15.3 |
| Inflector fringe field uncertainty | 200 | – | – | – | – |
| Time dependent external $B$ fields | – | – | – | 5 | 15.6 |
| Others † | 150 | 100 | 100 | 30 | 15.7 |
| Total systematic error on $\omega_p$ | 400 | 240 | 170 | 70 | – |
| Muon-averaged field [Hz]: $\widetilde{\omega}_p/2\pi$ | 61 791 256 | 61 791 595 | 61 791 400 | – | – |

Table 15.1: Systematic errors for the magnetic field for the different run periods in E821. R99 refers to data taken in 1999, R00 to 2000, R01 to 2001. The last two columns refer to anticipated uncertainties for E989, and the section in this chapter where the uncertainty is discussed in detail. †Higher multipoles, trolley temperature and its power supply voltage response, and eddy currents from the kicker.

It is important to note the steady reduction in uncertainties achieved in E821. The goal of 70 ppb uncertainty on $\omega_p$ for E989 in Table 15.1 reflects the current estimates of what can be achieved based on the experience in E821.

## 15.1.5   Overview of Precision Magnetic Field Measurement

Pulsed Nuclear Magnetic Resonance (NMR) is at the heart of the magnetic field shimming, measurement and control systems, since it can measure magnetic fields to absolute accuracies of tens of parts per billion (ppb).

The pulsed NMR hardware developed for E821, which produced and detected the free induction decay (FID) signals from protons in water or in petrolatum, has already demonstrated single shot precision at the level of 20 ppb [5], and absolute calibration in terms of the free proton precession frequency with an accuracy of of 35 ppb [6]. The challenge of the field measurement is to effectively transfer this absolute calibration to the many NMR probes required to monitor the field in the large volume and over the long periods of time during which muons are stored.

There are four major tasks required from the NMR system:
(1) Monitoring the field when muon data are being collected using fixed probes [15.2.1];
(2) Mapping the storage ring field when the beam is off using the NMR trolley [15.3];
(3) Providing an absolute calibration chain relating field measurements to the Larmor frequency of a free proton [15.4.1];
(4) Providing feedback to the storage ring power supply when muon data are collected [15.5].

We start with a brief description of NMR, explain the field measurement principles in more detail, then describe the required hardware.

### Field Measurement with Pulsed NMR

Precision measurements of the magnetic field are made by detecting the free induction decay (FID) signal of protons in materials containing hydrogen such as water or petrolatum[2] using pulsed NMR [11, 12, 5]. The probes used in E821 for these purposes are shown in Figs. 15.1 and 15.2. The material samples are located in small volumes (typically <1 cm$^3$) surrounded by a coil $L_s$ and the rest of the body of an NMR probe. Several hundred fixed probes are located around the azimuth of the ring, just above and below the muon storage volume. Other sets of probes are pulled through the storage volume in a trolley used to determine the field seen by the muons. A final set of probes is used for calibration.

In a typical measurement, an RF pulse at $\omega_{\mathrm{ref}} = 2\pi \times 61.74$ MHz, is used to produce a linearly polarized rf magnetic field in the coil $L_s$, orthogonal to the storage ring dipole field. This rotates the magnetization of the protons in the sample so that it is perpendicular to the main field of 1.45 T. After the $\pi/2$ pulse, the proton spins precess coherently in the external field at the proton magnetic resonance (Larmor) frequency $f_{\mathrm{NMR}} \approx 61.79$ MHz. The magnetic field from the rotating magnetization induces an EMF in the coil $L_s$ which is called the NMR signal. This signal typically decays exponentially with a time constant $T_2^*$ of several ms. The coil (which is used for both excitation and detection) is part of a circuit with a capacitor $C_s$ in series to form a resonant circuit at the NMR frequency $f_{\mathrm{NMR}}$ with

---

[2]The default is to use petrolatum as the NMR sample in the E989 fixed probes. We will refine and complete the studies of the temperature dependence of the susceptibility and shielding in petrolatum before the end of 2014.

(a)  Absolute calibration probe

(b)   Spherical  Pyrex container
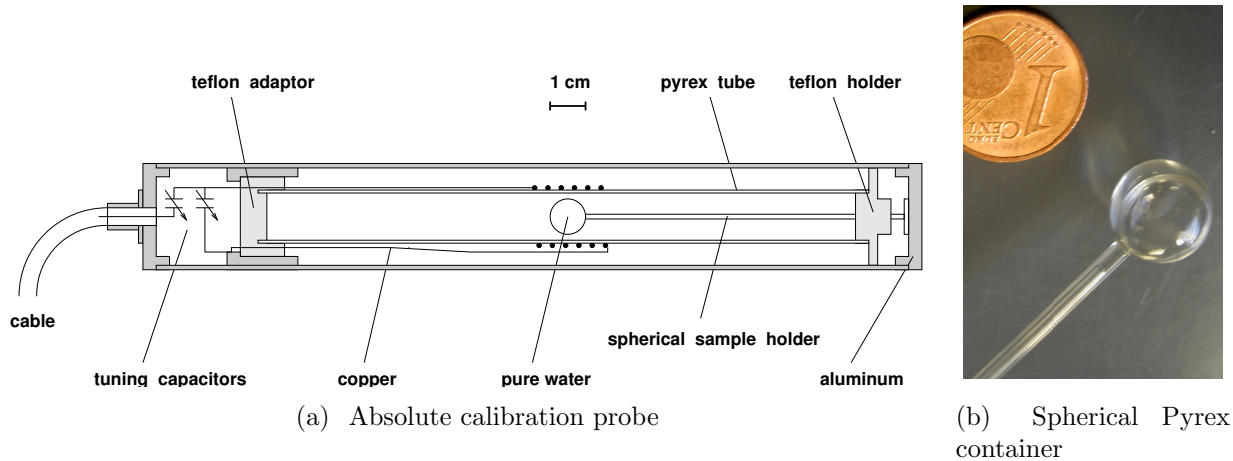
Figure 15.1: (a) Absolute calibration probe featuring a spherical sample of water. This probe and its driving and readout electronics are the very same devices employed in reference [3] to determine $\lambda$, the muon-to-proton magnetic-moment ratio. (b) The spherical Pyrex container for the absolute probe.

a quality factor $Q$ typically between 30 and 100. An additional parallel coil, $L_p$ or series capacitor is used to match the impedance of the probe at $f_{\mathrm{NMR}}$ to the 50 $\Omega$ impedance of the cable. The NMR signal propagates through a cable to a duplexer which directs the signal to a low-noise preamplifier. The amplified signal is mixed with the synthesizer frequency $\omega_{\mathrm{ref}}$, and the difference frequency $f_{\mathrm{NMR}} - f_{\mathrm{ref}} \equiv f_{\mathrm{FID}}$ goes through a low pass filter and is amplified and digitized. This signal is referred to as the FID (free induction decay). The frequency of the FID, $f_{\mathrm{FID}}$, is sensitive to the local field value and is of order 50±5 kHz. The exact frequency can be determined from the digitized signal by identifying and counting zero crossings of the FID and counts of the digitizer clock until the signal has decayed to about $1/e$ of its peak value, which typically takes several ms [3]. Other analysis techniques are under development. The local magnetic field is then characterized by the frequency $f_{\mathrm{NMR}} = f_{\mathrm{ref}} + f_{\mathrm{FID}}$ with resolution approaching 20 ppb.

As discussed below, the reference frequency $f_{\mathrm{ref}} = 61.74$ MHz is chosen such that $f_{\mathrm{ref}} < f_{\mathrm{NMR}}$, and is obtained from a frequency synthesizer phase locked to a Rb frequency standard stabilized by GPS (see section 15.2.4). The same Rb standard will provide the time base for the $\omega_a$ measurement.

## 15.2   The Fixed Probe NMR system

The purpose of the fixed probe system is to accomplish the first major field measurement task of Sec. 15.1.5; monitoring the field continuously while muon data are being collected. The fixed probe system consists of the fixed NMR probes and the accompanying VME system,

---

[3]Corrections are applied to handle lineshapes for which the instantaneous FID frequency varies with time [13].

(a)  Plunging probe



(b)  Trolley and fixed probe
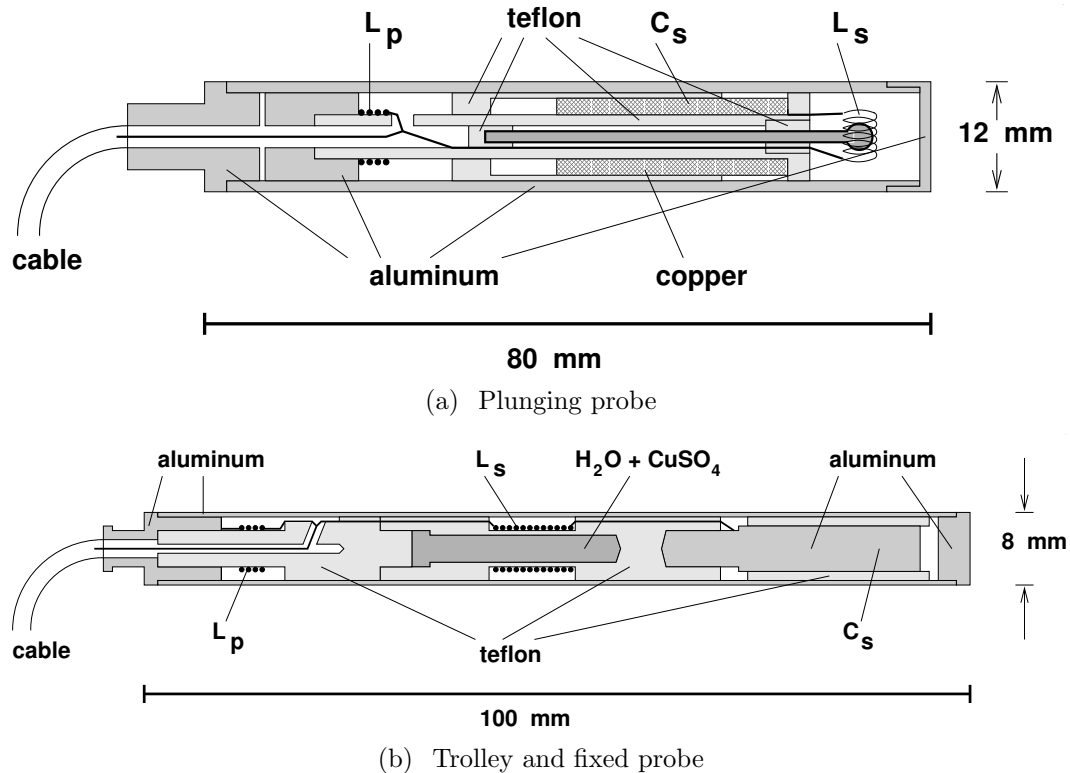
Figure 15.2: (a) Plunging probe, which can be inserted into the vacuum at a specially shimmed region of the storage ring to transfer the calibration to the trolley probes. (b) Schematic of the probes used in the trolley and as fixed probes in E821. The resonant circuit is formed by the two coils with inductances $L_s$ and $L_p$ and a capacitance $C_s$ made by the aluminum housing and a metal electrode. The active sample volume has a diameter of 2.5 mm and a length determined by the coil $L_s$ of 15 mm.

DAQ, pulser, mixer, multiplexers, and digitizers. A block diagram of the recommended system is shown in Fig. 15.3.

The design consists of a set of 378 NMR probes at 72 locations in azimuth around the ring. The number of probes at each azimuthal position alternates between two probes at radii of 7112 and 7142 mm, or three probes at radial positions of 7082, 7112, and 7142 mm, where the probes are placed in matching grooves on the upper and lower surfaces of the storage ring vacuum chambers. From this geometry the fixed probes provide a good monitor of the dipole field around the ring, with some sensitivity to changes in the skew and normal quadrupole components.

Groups of 20 probes are connected to a single analog multiplexer. Twenty multiplexers are required to handle all of the fixed probes, the plunging probe and the absolute calibration probe (see below). In a typical BNL E821 measurement sequence, one probe from each multiplexer was excited and its FID passed to a frequency counting module (there were 20 of these). Roughly 0.2 s later, a second probe from each multiplexer was selected, excited, and read out. Given there were 5 probes read out per second per multiplexer and 20 multiplexers,
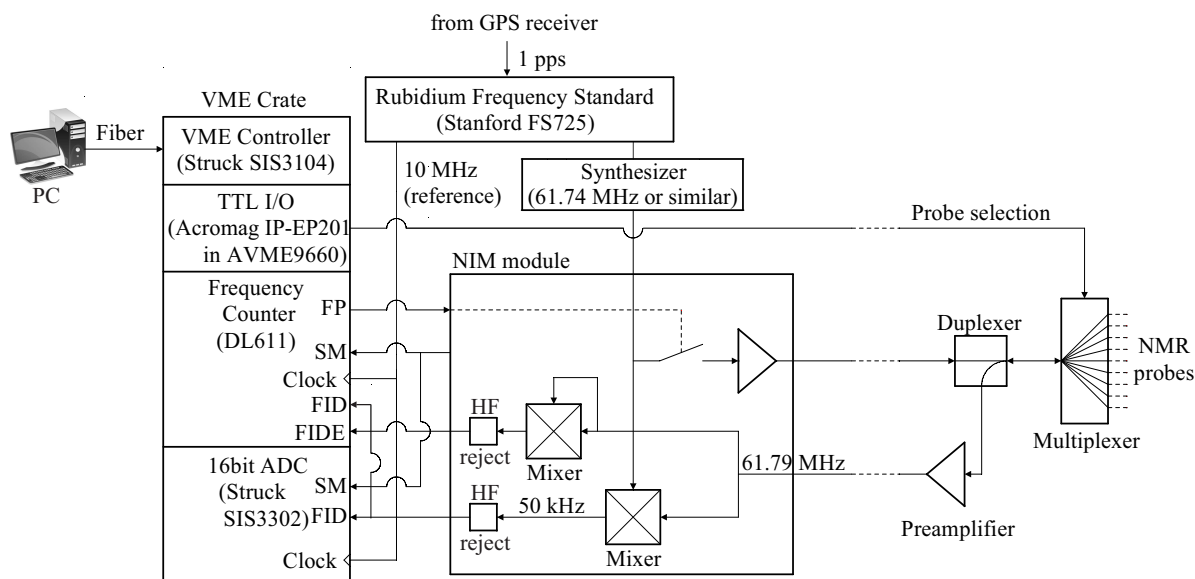
Figure 15.3: A schematic of the fixed probe system. The system consists of a set of NMR probes close to the muon storage volume connected to multiplexer boxes that sit on the storage ring magnet. The multiplexers, which contain the duplexers and preamplifiers, are connected to NIM modules and a VME system and DAQ that sit in the counting house. The functions of each element are described in the text.

100 probes were read out per second. The complete set of fixed probes was read out every 4 seconds during data-taking periods when muons are stored. For E989, with current PCs and faster VME64 hardware, all probes can now be digitized and read out within the 1.33 second beam supercycle.

In E821, roughly half of these fixed probes were used to monitor the storage ring field. Of the remaining probes, some were noisy, and a significant number were located in regions near the pole-piece boundaries, where local magnetic field gradients were sufficiently large that they reduced the free induction decay time $T_2^*$ in the probes to a millisecond or less.

In E989 several steps will be taken to increase the number of useful probes. First, finite element analysis of the vacuum chambers indicates that the grooves containing the probes can be extended without significantly increasing the deflection of the chambers under vacuum. This will allow probes to be moved farther from pole boundaries, increasing the number of useful probes. Second, in E821, at least initially, many of the fixed probes used water in their sample volumes and over the course of the experiment experienced loss of the water. In E989, the water samples will be replaced with petrolatum (CAS 8009-03-8). Petroleum jelly was observed in E821 to have low evaporation while providing a proton NMR signal comparable in magnitude and frequency to water. It has favorable relaxation times; measurements at U. Michigan indicate $T_2$ of order 40 ms. A third factor contributing to a more robust fixed probe measurement comes from the refurbishment of the E821 probes (see below), in which defective electrical contacts which led to poor signal quality will be improved. Finally, the NMR electronics of E821, which extracted precession frequencies by counting zero-crossings of FIDs mixed down to the 50 kHz range, will be replaced with a high-performance set of

digitizers. The 16 bit (13 bits effective), 10 MS/sec digitizers (Struck SIS 3302) will allow useful information to be extracted from probes with short signals. In addition, as explained below, higher resolution is made possible by extracting frequency information from the entire FID rather than just the zero crossings.

## 15.2.1  Fixed Probes for E989

The same basic probe design from E821 will be used for E989 (see Fig.15.2(b)). Materials used to construct the probes, mostly aluminum and teflon (PTFE), have low susceptibility and the coax cable has copper conductors instead of the more common copper-plated steel. Each probe's outer aluminum shell has a diameter of 8 mm, which fits in grooves machined into the outside surface of the top and bottom plates of the vacuum chamber. The probe's outer shell and the inner body form the capacitor $C_s$, which is in series with $L_s$ and makes a resonant circuit. $C_s$ is adjusted by moving a PTFE sleeve in and out to tune the circuit to the frequency $\omega_p/2\pi$. A circuit quality factor $Q \approx 30$ corresponds to a bandwidth of 3% which is the range over which the magnetic field can be measured without retuning the probes. A parallel coil $L_p$, allows for matching the impedance of the probe to 50 $\Omega$ for optimal transmission.

**Refurbishing existing probes:**

Resurrecting the existing E821 measurement system requires a complete working set of probes provided either by refurbishing existing ones or constructing new ones. In E821 the sample volume was filled with water doped with $CuSO_4$. This dopant is paramagnetic and is used to shorten the magnetization recovery time $T_1$ so measurements can be made more frequently. For pure $H_2O$, $T_1 \approx 3.5s$, so consistent free-induction-decay NMR measurements could only be taken every 30 seconds. However, paramagnetic impurities also shift the measured frequency, and changes in the $CuSO_4$ concentration, for example due to slow evaporation of the water, will affect the stability of the measurement. An examination of probes from E821 indicated that in some probes water had leaked and corroded part of the probe. These probes will be rebuilt. To prevent similar difficulties in E989, we will use petroleum jelly in place of the $CuSO_4$-doped water. This idea was implemented in some fixed probes of E821 by R. Prigl. We have recently measured the NMR relaxation times of a sample of petrolatum at 0.4 T using saturation-recovery (for $T_1$) and a standard spin-echo sequence (for $T_2$) at Michigan. We find $T_2 \approx T_1 \approx 40$ ms, which is long enough for very high resolution frequency determination, and will not restrict $T_2^*$ which is typically limited to a few milliseconds by local field gradients. The temperature dependence of the diamagnetic shielding is also crucial. Preliminary work in E821 indicated the temperature coefficient of the chemical shift $d\sigma/dT$ is smaller than the shift in water, providing greater stability. Recently at Washington, $d\sigma/dT$ for petrolatum was measured to be $\approx +1$ ppb/K, roughly a factor of 10 smaller than in water. The volume magnetic susceptibility $\chi_V$ of petrolatum was measured to be roughly -8$\times 10^{-6}$ in SI units, with temperature dependence $d\chi_V/dT$ roughly $-1 \times 10^{-9}$. The overall temperature dependence of petrolatum probes should be more than a factor 4 smaller than the fixed probes with water samples of E821.

The scale of the refurbishing effort was estimated from tests on about 40 fixed probes from

E821. The results indicated that about 1/4 of the probes had water leaks and corrosion, and will need to be rebuilt. Another area of some concern occurs where the coil wire is bonded to the aluminum parts with low temperature solder. This connection requires inspections and probes with broken connections will require re-soldering. All probes will be filled with petroleum jelly from a single source, tuned, and checked for correct functioning.

An existing dipole magnet at University of Washington (see figure 15.4) has been repurposed to provide the 1.45 Tesla field required for testing the NMR probes. The nominal field uniformity is 100 ppm/cm over the entire pole face but there are regions with better than 10 ppm uniformity over the active volume of the probe. Active shimming with opposing Helmholtz coils further cancels linear gradients and FIDs lasting 4 to 5 ms can be obtained. A subset of the E821 electronics initiates and reads out the free induction decays. The magnet permits testing the entire fixed probe system over a wide range of field gradients.
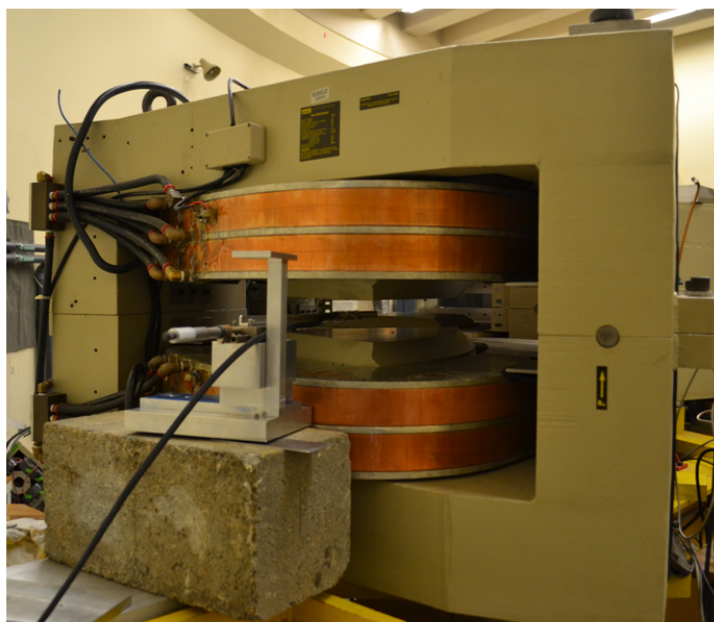


Figure 15.4: Dipole magnet at the University of Washington shown with field mapping in progress. It provides a 1.45 Tesla field sufficiently uniform for testing probes and electronics for the E989 fixed probe system.

**Constructing new probes:**

Any new probes constructed are required to fit in grooves machined in the vacuum chambers. The E821 probes were reverse engineered and CAD drawings produced. In consideration of the quantity, new parts will be produced using computer numerically controlled mills and lathes at the UW machine shop. Metric sized aluminum tubing 8 mm × 0.5 mm and 7 mm

(a)  Slotted PTFE dielectric



(b)  pNMR probe with crimp connection

Figure 15.5: (a) The position of the PTFE dielectric can be adjusted within the assembled probe by using a hollow core screwdriver. (b) An assembled NMR probe during frequency tuning with the new crimp type connection for the coax cable.

PTFE rods are available in the European market. The new design concentrates on three parts of the probe. Firstly, as in the E821 design, the resonant frequency of the LC circuit is tuned by adjusting the position of a PTFE dialectric cylinder on the threaded inner conductor of the capacitor $C_s$. In the new design, only the end cap shown in figure 15.2(b) needs to be removed. Milling a slot in the end face of the PTFE capacitor dialectric allows it to be adjusted with the hollow core screw driver shown in figure 15.5(a). The resonant frequency is tuned while observing the reflection coefficient on a vector network analyzer.

Secondly, we use an ultrasonic flux free soldering iron to connect $L_s$ and $c_S$. Ultrasonic sound replaces the flux normally used to clean surfaces while soldering. The third improvement is the way the electrical connections a re made between the coax braid, probe end cap and coil $L_p$. We have successfully demonstrated mechanical crimp connections that will replace the conducting epoxy used in E821 probes.There are major advantages to crimp type connections. The electrical contact between the cable braid and the probe end cap are significantly improved. During the process of crimping the insulating aluminum oxide layer is mechanically broken which results in a low ohmic joint. In addition, the crimped connection is protected from corrosion since it is air tight and thus keeps oxygen away from the contact areas. It is mechanically strong. The crimp includes the coax outer jacket in the same manner as the commercial SMA connector on the other end of the cable and provides strain relief (see figure 15.5(b)). In the E821 design, strain relief was provided by a shrink tube which was sometime not sufficient to prevent the epoxy joint from breaking. Where possible we intend to reuse the proton sample holders from the old probes to reduce the number of these complex parts that have to be made. After new parts are completed coils will be wound and the same procedure as for refurbishing will be followed.

**Testing the probes:**

For each probe, the resonant circuits are tuned to 61.79 MHz and 50 $\Omega$ impedance using a vector impedance meter. The resonance is then excited in the probe and if the free induction decay (FID) is observed with sufficient signal to noise ratio SNR, the probe passes the test. In the E821 system the SNR at the beginning of the FID was $\approx$ 300:1.

## 15.2.2 Multiplexers

Groups of up to 20 fixed probes are connected to a single multiplexer located a few meters away (probes have 5 meter cable lengths), which sits on top of the magnet. The multiplexer design is described in [5, 8]. It is a self-contained electronic module that selects one of 20 NMR probes based on a 5 bit address set by the NMR DAQ. A cable terminated with DB-9 connectors connects the multiplexer to TTL level digital output lines from the VME subsystem. The TTL signals control PIN diodes in the multiplexer that direct a $\pi/2$ RF pulse from the NIM pulser/mixer module to tip the spins in the selected NMR probe. When the circuit is closed, there is a measured 2.5 dB insertion loss. To improve the isolation when the circuit is open, effective-$\lambda/4$ lines are incorporated into the switches. A duplexer (basically a transmit/receive switch) in the multiplexer directs the high power RF pulse towards the selected NMR probe, while isolating the sensitive low-noise preamplifier. After the RF pulse, the duplexer directs the returning low-level FID precession signal to a low-noise preamplifier with a gain of approximately 60 dB. The switches, duplexer, and TTL integrated circuits are fabricated with discrete surface mount components, and replacements are readily available.

The preamplifier consists of two RF amplifier modules, a UTO-101 and GPD-201 connected in cascade. These were made by Avantek at the time the multiplexers were developed and are currently sourced by Teledyne-Cougar. The first stage has a noise figure of 1.7 dB with a typical gain of 27 dB. The wireless communication industry has advanced the state of the art in RF amplifiers since the days when the multiplexers were designed providing many more options. For example, the Minicircuits ultra low noise MMIC amplifier PSA4-5043+ has an equivalent gain and an improved noise figure of 0.7 dB and also recovers rapidly from an overload condition such as is experienced when probes are excited. The amplifier is available both as a surface mount chip and as an evaluation module (TB-653+) with connectors that could be used in the multiplexer with minor circuit board modifications. This preamplifier has the dual advantage of better noise performance which leads to longer useful FID times and no longer having to rely on obsolete parts. We plan to evaluate the unit in the near future.

## 15.2.3 Pulser and Mixer

The Pulser and Mixer is a single width NIM module located adjacent to the VME crate and connected by cables to a single multiplexer. This functions as the receiver and transmitter (pulse generator) for the NMR fixed probes. One shot multivibrators triggered by the fire pulse (FP) from the VME subsystem generate a logic pulse with a width adjusted to the desired length for the $\pi/2$ pulse. A jumper on the circuit board determines whether this

generated logic pulse or the input FP pulse determines the duration of the $\pi/2$ pulse which then gates on the $f_{\text{ref}} = 61.74$ MHz reference and sends it through a custom made class-C amplifier to the multiplexer. The measured RMS power in a 50 ohm load is about 0.8 Watts and length of the $\pi/2$ pulse is 7 $\mu s$. In the receiver part of the module, the amplified probe signal from the multiplexer is mixed with the reference frequency $f_{\text{ref}}$ and the difference frequency (about 50 kHz) is the free induction decay signal (FID). In a second branch of the receiver, the envelope of the probe signal (FIDE) is obtained by mixing the preamplifier output with itself and filtering out the $2\omega_L$ component. The $\pi/2$ pulse causes some saturation in the preamplifier and a TTL signal (SM) is provided to delay processing the FID for roughly 10 $\mu s$ after the end of the RF pulse. In E821 this pulse was used by the custom Heidelberg DL611 frequency counter module to enable the start of the zero crossing counter. The delay accommodates both the dead time in the preamplifier and transients such as those from ringdown of the $L_s$ coil and decay of the transient response in the low-pass filter after the mixer.

The inputs and outputs of the NIM modules are shown in Fig. 15.3. The inputs are the fire pulse (FP) which initiates the free induction decay, the synthesizer reference $f_{\text{ref}}$ and the returning FID signal from the multiplexer preamplifier. The outputs are the high power $\pi/2$ pulse, the SM signal, the envelope function (FIDE) and two channels of FIDs, one for the DL611 zero-crossing counter and one for the waveform digitizer. This module contains mostly surface mount and integrated circuit components and replacements are readily available. RF amplifiers GPD-201, GPD-202, and 3 GPD-462 were made by Avantek when this board was designed and they continue to be sourced by Teledyne-Cougar. The most likely point of failure in the class C amplifier is a DU2820S MOSFET, which is still available and could be replaced if necessary with little difficulty. Replacement amplifiers exist but they tend to be wide band class A amplifiers, which are less efficient. In constructing new pulser/mixer modules, using class-A or class-AB amplifiers would require mounting external to the NIM module to dissipate the additional heat. Modular high performance commercial RF amplifiers are available from Amplifier Research and other vendors.

## 15.2.4    Frequency Reference

The NMR system requires a frequency synthesizer at 61.74 MHz, which is amplified and pulsed for manipulating the proton spins in the NMR probes and a 10 MHz clock for the waveform digitizers. Since the NMR clocks and the clock used by the waveform digitizers to determine the muon spin precession frequency are phase-locked to the same master clock, the variations in the master clock frequency drop out to first order, and the ppb-level accuracy requirement is reduced to be less than about $10^{-5}$. Nevertheless, to simplify the study of systematic uncertainties in the magnetic field, our goal is to have relative uncertainties in the reference clock frequencies be less than 1 ppb. This uncertainty must be achieved for short times, that is a few milliseconds for a single NMR measurement where phase noise is the limiting factor and long times over the course of the experiment.

Figure 15.6 shows how the reference frequencies are generated. The master clock, an EndRun Technologies Meridian Precision GPS Frequency Standard, is an atomic rubidium oscillator disciplined by GPS for better long-term stability. It generates a master frequency that is a sine wave at 10 MHz and an IRIG time code signal used by DAQ computers for
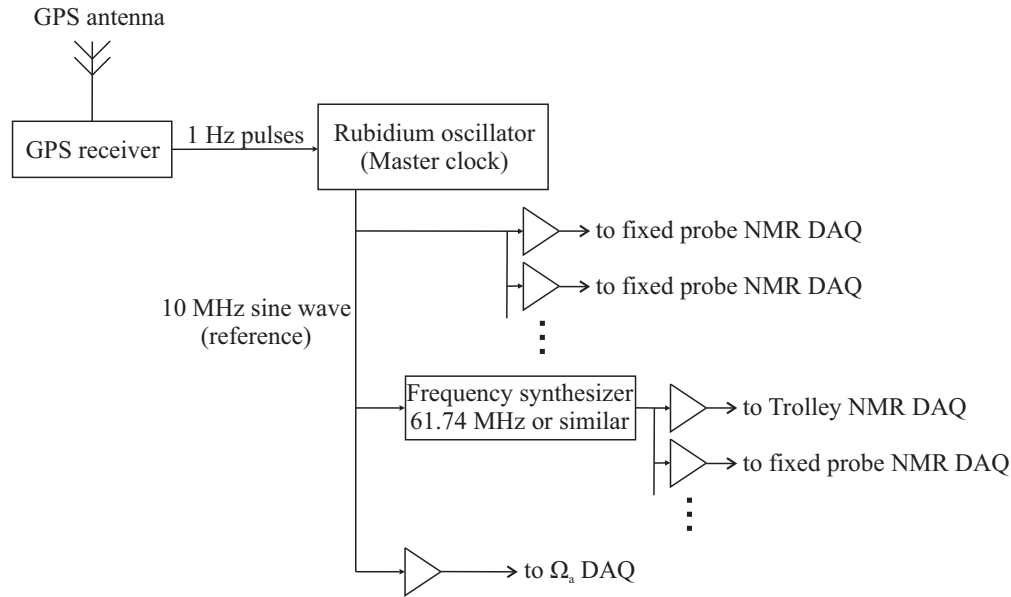
Figure 15.6: Scheme for common master-clock.

their time stamps. The master frequency is distributed to the data acquisition system for $\omega_{\mathrm{a}}$, where frequency synthesizers are used to transfer the master clock frequency to the clock frequency needed by the waveform digitizers. It is also used as input for the frequency synthesizer responsible for the NMR reference frequency $\omega_{\mathrm{ref}}$. Frequency synthesizers in both systems should have resolutions of about 1 ppb, to allow for some variability in the frequency that can be used for blinding schemes and for tests of systematics. It is the synthesized frequencies that must fulfill the accuracy requirement discussed above. Synthesizers that fulfill the requirements given above are available from vendors including Precision Test Systems, Symmetricon, Agilent, and Stanford Research Systems. Distribution amplifiers from vendors including Stanford Research Systems and Mini-Circuits can distribute the master clock and the needed reference frequencies to the places where they are needed. There is experience in the collaboration in the specification and use of these systems from E821 and, more recently, from the clock system used for the MuLan experiment at PSI in Switzerland.

## 15.2.5 NMR VME System and DAQ

The fixed probe NMR system will be controlled from a VME crate performing similar functions as in E821 but with different hardware.

The NMR DAQ system (see Fig. 15.3) performs the following tasks: (1) Selects probes in the multiplexers, (2) Initiates Free Induction Decays (FID) in selected probes, (3) Digitizes the mixed down FID waveforms from the NIM modules, (4) Extracts frequencies $\omega_p$ from the digitized waveforms for displaying and controlling the field and (5) Records frequencies and selected digitized waveforms along with a timestamp.

Hardware for the new system includes a 6U VME 64x crate and Struck SIS1100 VME crate controller which connects via a fiber optic cable to a Struck SIS3104 PCIe card on a

PC running Scientific Linux. This allows the VME crate to be placed in the experimental hall and controlled by the PC in the control room. The new controller is compatible with the VMEbus IEEE-1014 standard E821 crate, and with the faster 2eVME bus cycles of VME64x system of E989. The 5 bit multiplexer addresses are provided by an Acromag AVME9660 VME carrier card with four 48 line digital I/O daughter boards. One of these, an IP-EP201 includes a programmable Altera Cyclone II FPGA controller and clock. Acquisition code executes in the PC under LINUX, which is not a real time operating system. Critical timing requirements are achieved with the FPGA controller which will be programmed to sequence through probe addresses and trigger the waveform digitizers. The controller can also generate the appropriate length $\frac{\pi}{2}$ pulse to initiate free induction decays in the probes which can be varied to maximize the amplitude of the FID. A jumper selectable option will be added to the NIM modules to allow the width of this pulse to be controlled directly or from the default internal logic. Programming the FPGA controller requires some familarity with VHDL, its native language. Example software exists to map VME registers directly to the 48 lines of digital I/O so they may be controlled from code in the PC. FPGA sequencer code can be developed and debugged in C++ and then translated into native VHDL code for compiling and down loading to the FPGA. A custom breakout panel maps the 50 pin ribbon cable connectors on the VME module to independent DB-9 connectors for cabling to the multiplexer units. The mixed down FID waveform signals are read by 3 Struck SIS3302 8 channel 16 bit waveform digitizers to complete the complement of VME modules. These digitizers are described in section 15.2.6. A Meinberg TCR170PEX IRIG Time Code Receiver provides a timebase for the PC disciplined by the Meridian master GPS receiver. This PCIe board has a kernel driver which allows it to be used as a reference source for the NTP daemon and LINUX file system timestamp. A timestamp with accuracy better than a millisecond will be recorded with each set of NMR measurements.

Data acquisition software will be based on MIDAS, a system developed at TRIUMF and PSI that supports VME, RS232, GPIB, ethernet and USB hardware. It is used by many groups in the collaboration, integrates with ROOT for analysis and is officially supported by Fermilab under Scientific Linux. The MIDAS architecture supports multiple Front End modules that interface with the hardware and allow multiple data streams to be associated with a single event. While NMR measurements are in principle asynchronous with respect to accelerator operations, they can be synchronized to beam delivery events using available timing signals from the accelerator. The FPGA sequencer can vary the start delay so measurements can be made in quiet times as well as during beam spills and kicker events. Field measurements average the field over 5 ms. Measurement start times can be varied relative to the 17 millisecond period of ambient 60 Hz fields for a high precision determination of their contribution to the ring field.

In E821, the DL611 modules, which are described in [5], counted the number of zero crossings, $k$, of the FID until its envelope represented by the FIDE signal fell below an adjustable threshold or until a maximum time had elapsed. Over the same interval the ticks, $N$, of an external stabilized clock at $\nu_{\text{clock}}$=20 MHz were counted. For both counters the start and stop coincided with a positive zero crossing of the FID. The frequency of the FID is $\nu_{\text{FID}} = k \times \nu_{\text{clock}}/N$. For FID signals exceeding 1 ms, the uncertainty on the frequency due to the discretization of the clock counts is roughly 8 ppb or less. The uncertainty on the frequency due to the finite signal-to-noise of the FID (typically $S/N \approx 100$ when FIDE falls

below threshold) is given roughly by $\sigma_s/(S/N)$ where $\sigma_s$ is the signal line width, and $S/N$ is the signal-to-noise ratio. This is typically of order 25 ppb on a single NMR FID above threshold for a millisecond or more [5]. This motivated the decision to replace the DL611 hardware with waveform digitizers in E989.

A second MIDAS DAQ system will be assembled around E821's VME crate and DL611 zero crossing counters. The crate and some modules are known to work and code to access them has already been written. Given the modular nature of MIDAS an additional Front End module developed from the existing code base is all that is required to add the DL611s to the event stream. With this system in place, frequency readouts using both waveform digitizers and DL611 hardware can be compared.

## 15.2.6 Digitizer

With the DL611 hardware, the precession frequency is obtained directly from internal registers in the module. A more precise frequency determination can be achieved by first acquiring FID waveforms with fast, low-noise digitizers, such as the Struck SIS3302. These VME modules can simultaneously digitize 8 independent channels (8 multiplexers) with 16-bit ADCs (13 effective bits). The digitizers get their signals from the FID outputs on the NIM Pulser and Mixer modules, and sample at a frequency of 10 MHz for roughly 5 ms. Digitized waveforms require additional processing for frequency determination and various algorithms were explored for frequency extraction. One of these is a software version of the DL611 hardware where the digitizer's sample rate replaces the external clock, but with enhanced zero-crossing resolution, below the clock period, by interpolating between points on the waveform. Other methods use an FFT algorithm and extract frequencies from peaks in the power spectra. The most robust method found performs a 90 degree rotation in the complex frequency domain followed by an inverse FFT to transform back to the time domain which gives a function orthogonal to the original FID. The arctangent of this orthogonal pair gives the instantaneous phase advance of the precessing protons. With homogeneous fields, there is a linear relationship between phase and time in the FID, and frequency is just the slope of this line (from a least squares fit).

Figure 15.7 Compares the frequencies extracted from simulated FID waveforms by counting zero crossings with the method using continuous phase advance. Simulated waveforms have identical frequencies and differ only in Gaussian noise. The $x$ scales extend from -50 ppb to +50 ppb on both plots. The widths of the histograms represent the precision by which each method can extract the frequency in the presence of noise. The width from counting zero crossings (left) is about an order of magnitude larger and like the actual DL611 hardware, is dominated by uncertainties in the times of the last zero crossings where the signal to noise ratio is smallest. These plots show the advantage of using the entire digitized FID waveform in determining the frequency.

Linear gradients in the magnetic field over the probe volume reduce the precision of frequency measurements by decreasing the length of time the protons precess coherently ($T_2^*$). With non-linear gradients the lineshape is asymmetric and the relationship of phase with time is no longer linear so the instantaneous FID frequency varies with time. The average field, which is the field seen by the muons, corresponds to the centroid of the line. This can be determined by extrapolating the instantaneous FID frequency to its value at t=0 [13]. The

FID frequency variation can be of order 15 ppb [13], and is relevant primarily for the absolute calibration. Digitization of FIDs from the abolute calibration probe is essential to reduce possible systematic uncertainties on the $B$ field measurement from lineshape asymmetries and field inhomogeneities.
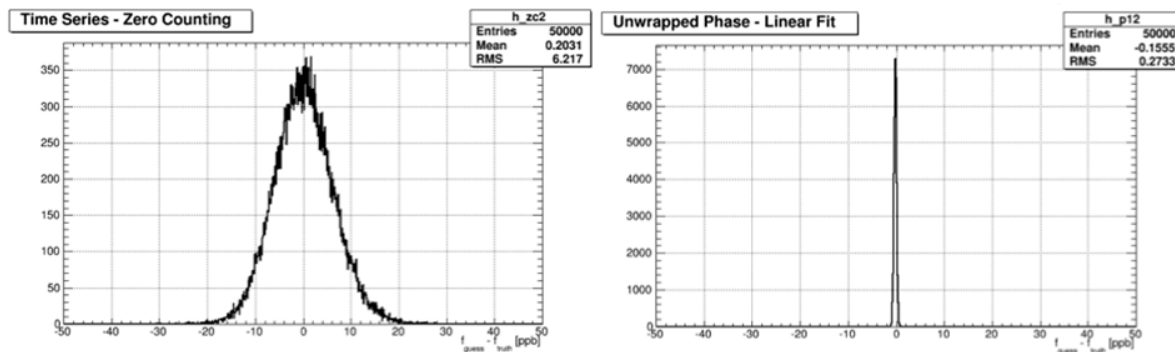


Figure 15.7: The figure shows histograms of frequencies extracted from simulated free induction decays with added Gaussian noise. In the left plot frequencies are determined from counting zero crossings (a software implementation of the DL611 hardware counters used in E821). In the plot on the right frequencies are determined from the phase advance of precessing protons vs. time in the FID waveform.

The digitizers will only provide these benefits if the digitization noise is comparable or less than the noise on the signal. For E821, FID signals were of the order of a volt. When the FID envelope (FIDE) dropped below threshold at $\approx$ 100 mV, the $S/N$ of 100 implies signal noise was of order 1 mV. For the SIS3302, with a -1V to 1V full scale range, and minimum 13 effective bits, the digitization noise is predicted to be 0.24 mV, safely below the FID noise.

With a sampling frequency of $10 \times 10^6$ samples/s, 16-bit resolution, and a period of $5 \times 10^{-3}$ s, the waveform from a single probe produces $\approx$ 100 kB of data. Muons are injected into the storage ring in the first 0.5 seconds of the 1.33 second beam supercycle. This leaves a quiet period of 0.82 seconds without field perturbations from the kicker field. Reading 400 probes once in half of the beam cycle would require a data rate of about $2 \times 30$ MBytes/s (40 MBytes/1.33s) which is well within the 80 MBytes/s bandwidth that can be achieved with VME64x crates. Varying the start time in the cycle allows the probes to be read in both quiet and kicker periods to study residual effects of the kicker fields. In addition, the T1 relaxation time for Petrolatum is about 40 ms permitting probes to be read out every 0.4 seconds. Acquiring waveforms continuously for a year at this rate would consume about a petabyte of storage. There would be no need to store all digitized waveforms. After the frequency information has been extracted, a smaller subset of the digitized FIDs would be retained for off-line analysis. Recording waveforms once per minute, for example, would

(a)  NMR Trolley

(b)  Distribution of NMR probes
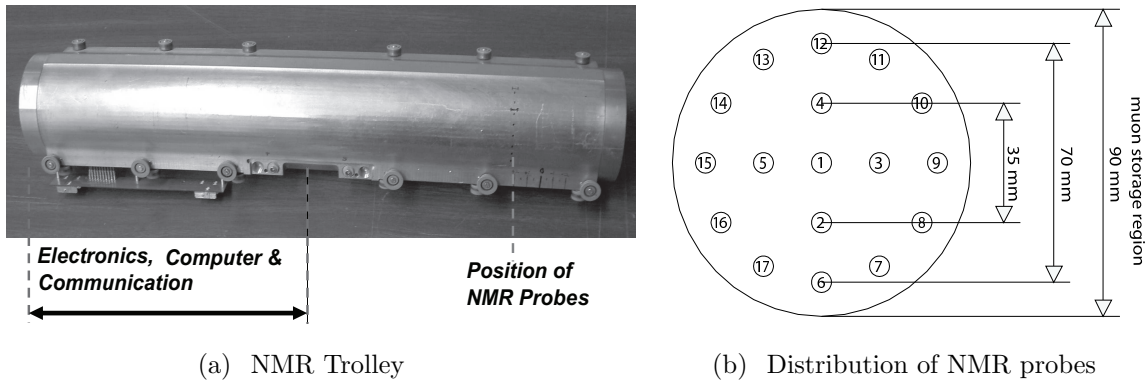
Figure 15.8: (a)Photograph of the $\sim$ 50cm-long NMR trolley, which measures the magnetic field in the storage ring. The array of 17 NMR probes, which are located inside the trolley housing, are 82(1) mm behind the front of the trolley. Electronics occupies one end of the device. At the other end where the probes are located, the field perturbation from the electronics is less than 2 ppm and is accounted for as part of the calibration procedure. (b) The probe numbers and placement are given by the schematic.

reduce the required yearly storage to 17 terabytes, an amount easily obtained on todays modern servers. The actual rate would be determined by the needs of the analysis.

We also note that a high performance digitizer is also useful in analyzing the lineshapes of the calibration probes. These lineshapes contain information about perturbations due to probe materials, the amount of water in the thin neck of the spherical water sample and other effects. This information can be used to reduce the uncertainties in the absolute calibration.

## 15.3   Trolley

The trolley performs the second major task of the field measurement system in Sec. 15.1.5: it determines the magnetic field distribution over the muon storage volume around the ring intermittently when the beam is off. It uses an in-vacuum NMR trolley system developed for E821 at the University of Heidelberg [9], shown in Fig. 15.8(a). This trolley contains 17 NMR probes arranged in concentric circles as shown in Fig. 15.8(b). Each probe measures the field at several thousand points around the ring. The trolley was designed and built to minimize distortions of the magnetic field in the ring. On board is a fully functional CPU which controls the FID excitation and FID zero crossing counter. Additional sensors connected to the microcontroller are used to measure position, pressure, and temperature. The trolley is pulled around the storage ring by two cables, one from each direction circling the ring. One of these cables is a thin co-axial cable with only copper conductors and Teflon dielectric and outside protective coating (Suhner 2232-08). It carries simultaneously the dc supply voltage, the reference frequency $f_{\text{ref}}$ and two-way communication with the spectrometer via RS232 standard. The other cable is non-conducting nylon (fishing line) to eliminate pickup from the pulsed high voltage on the kicker electrodes.

**Magnetic Field Maps**

From the trolley field measurements, the multipole composition of the field averaged over the ring azimuth is extracted, then folded with the multipole expansion of the measured stored muon beam profile. Because muons cannot be stored while the trolley is in the storage volume, trolley field maps must alternate with periods in which muon spin precession data are taken. Over the duration of E989, trolley runs will be executed on intervals of non-integer diurnal cycles such that the overall distribution of trolley runs versus time is uniform. This reduces correlations between trolley runs and possible biases from day/night or other potential periodic changes in the storage ring field.

During mapping, the trolley is moved into the storage ring and pulled continuously clockwise or counterclockwise through the entire storage volume over the course of roughly 2 hours. The field is sampled at 6000 locations in azimuth by each of the 17 probes (which are cycled through continuously) for a total of 100,000 field points. During these runs, a cross-calibration of the field observed by the fixed probes and the field measured by the trolley probes is performed. This is required to determine the magnetic field encountered by the stored muons in the storage volume from the measurements of the surrounding fixed probes taken at the same time. Because this cross-calibration between the trolley measurements and fixed probes will be slightly different each time the magnet is powered up or down (because the field shape changes slightly), trolley runs must be taken every time the magnet current is changed. This cross-calibration is sensitive to magnet temperature and current, both of which also change the field shape slightly. Improved insulation of the magnet and experimental hall floor, as well as the more uniform thermal environment in the E989 experimental hall versus E821 should keep the magnet temperature more stable and uniform. This will also reduce the magnitude of changes to the current required to stabilize the field. Reductions in both factors will reduce changes in the cross-calibration and allow better tracking of the storage ring field between trolley runs. Note that these changes in cross-calibration can be determined in advance of data-taking by measuring the difference in fixed probe and trolley probe measurements as the current in the magnet is changed deliberately, and as a function of the experimental hall/magnet temperature. Finally, the frequency of trolley runs will be adjusted and additional insulation can be used to ensure that the uncertainty on the field tracking goals are met.

The performance of the system can be gauged from E821. The magnitude of the field measured by the central trolley probe is shown as a function of azimuth in Fig. 15.9 for one of the trolley runs in E821. The inset shows that the fluctuations in this map that appear quite sharp are in fact quite smooth, and that the noise is small in comparison.

Since the NMR frequency is only sensitive to the magnitude of $B$ and not to its direction, in addition to the main vertical field $B_y$, in principle there could be significant radial fields and fields in the azimuthal direction. In practice, the magnitude of radial field will be measured (see section 15.8.2), pole tilts will be measured with a precision electrolytic tilt sensor and adjusted, and surface correction coils will be used to ensure the local radial field is less than 50 ppm. In E821 the average radial field achieved was $20 \pm 10$ ppm [52]. Longitudinal components of the field will be similarly restricted, especially by improved shimming. Hall probe magnetometers will measure the radial and longitudinal field components prior to vacuum chamber installation, and the radial field will still be accessible via vacuum ports
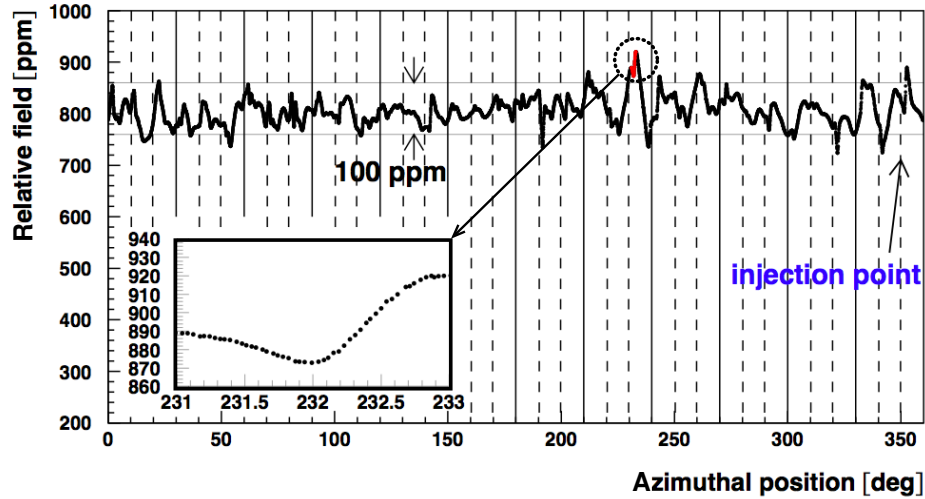
Figure 15.9: The trolley measurement of the magnetic field at the storage of the storage region vs. azimuthal position. Note that while the sharp fluctuations appear to be noisy, when the scale is expanded the variations are quite smooth and represent true variations in the field.

subsequent to chamber installation. This iterative sequence of measurements and corrective actions should ensure the difference between the azimuthally-averaged $|\vec{B}|$ and $|B_y|$ is less than 10 ppb.

Since the storage ring has weak focusing, the average over azimuth is the important quantity in the analysis. This is achieved using the trolley field maps by averaging the trolley probe measurements over azimuth. A contour plot for an azimuthally-averaged field map from E821 is shown in Fig. 15.10(b). Such azimuthally-averaged field maps are then expressed in a two-dimensional multipole distribution over the radial and vertical directions, $x$ and $y$. It is more natural to use cylindrical coordinates $(r, \theta)$ where $r = 0$ is the center of the storage region and $\theta = 0$ points radially outward from the center of the ring. This yields the expansion for the field components:

$$B_y(r, \theta) = \sum_{n=0}^{n=\infty} \left( \frac{r}{r_0} \right)^n [ \quad a_n \cos n\theta + b_n \sin n\theta] \tag{15.5}$$

$$B_x(r, \theta) = \sum_{n=0}^{n=\infty} \left( \frac{r}{r_0} \right)^n [-b_n \cos n\theta + a_n \sin n\theta], \tag{15.6}$$

where the normal multipoles, $a_i$, and skew multipoles, $b_i$ are normalized at $r_0 = 45$ mm. In practice the $B_y$ series is dominated by the dipole term $a_0$ and the expansion is limited to $n \leq 4$. The radial field distribution $B_x$ is dominated by the radial dipole term $b_0$ which is measured separately with a Hall probe and is of order 20 ppm. NMR is nominally sensitive to the field magnitude, but effectively measures just the magnitude of the vertical field $|B_y(\vec{r})|$ since the orthogonal field components, which are of order 50 ppm or less, perturb the field magnitude by less than a few ppb.

(a) Calibration position                    (b) Azimuthal average
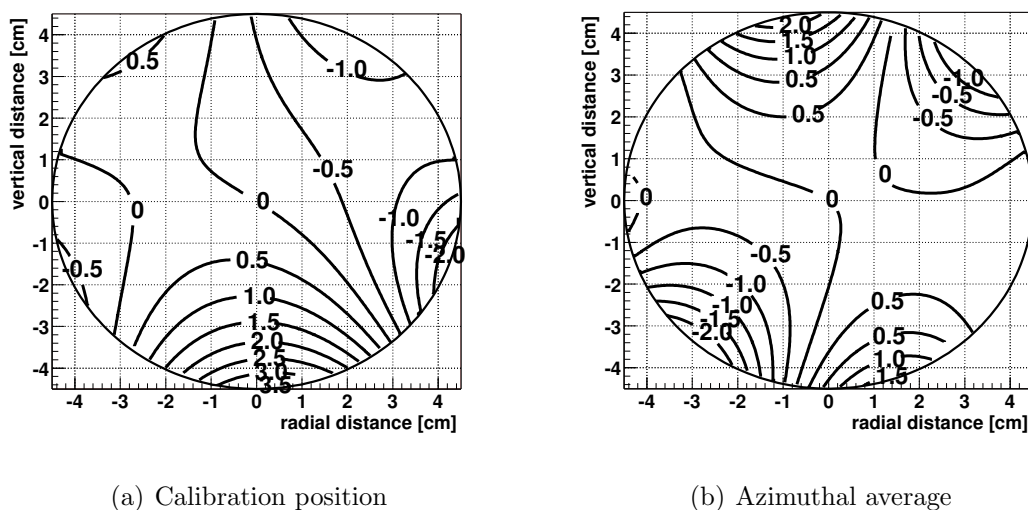
Figure 15.10: Homogeneity of the field (a) at the calibration position and (b) for the azimuthal average for one trolley run during the 2000 period. In both figures, the contour spacing is 500 ppb.

An example of the multipole decomposition from BNL E821 is shown in Table. 15.2.

Table 15.2: Azimuthally-averaged multipoles at the outer edge of the storage volume (radius = 4.5 cm) obtained in E821. The new experiment aims for a factor of two or better reduction in the average multipole amplitudes and also better azimuthal uniformity.

| Multipole | Azimuthal Average | |
| --- | --- | --- |
| [ppm] | Normal | Skew |
| Quadrupole | 0.24 | 0.29 |
| Sextupole | -0.53 | -1.06 |
| Octupole | -0.10 | -0.15 |
| Decupole | 0.82 | 0.54 |

**Fixed probe tracking of the magnetic field**

During data-collection periods the field will be monitored with the fixed probes. To determine how well the fixed probes allow monitoring the field in the storage ring acting on the muons, the field average determined by the trolley, and that predicted by the fixed probes will be compared for each trolley run. The results of this analysis for the E821 2001 running period is shown in Fig. 15.11. Disregarding hysteresis shifts identified in the figure with vertical lines, the RMS distribution of these differences is ~100 ppb.

The uncertainty in interpolating the storage ring field between trolley runs, by using the fixed probes, will be reduced from 70 ppb achieved in E821 to 30 ppb in E989 (see Table
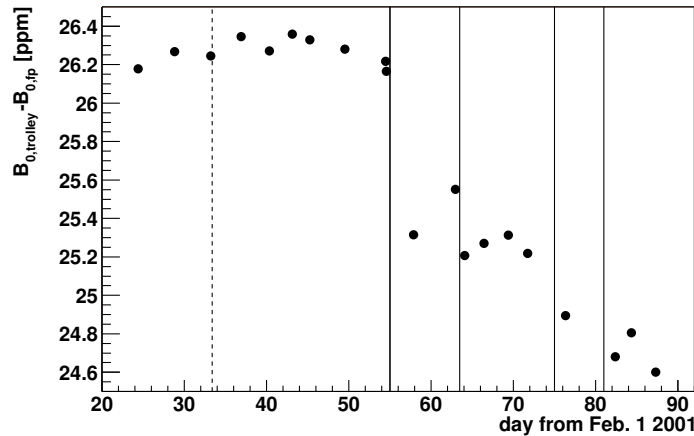
Figure 15.11: The difference between the average magnetic field measured by the trolley and that inferred from tracking the magnetic field with the fixed probes between trolley runs. The vertical lines show when the magnet was powered down and then back up. After each powering of the magnet, the field does not come back exactly to its previous value due to hysteresis, so that only trolley runs taken between magnet powerings can be compared directly.

15.1). The improvements are the result of several changes. First, the E989 experimental hall floor will be monolithic and much more mechanically stable than the E821 floor which was composed of three concrete sections. Second, the E821 experimental hall had very poor temperature control (day-night changes of nearly 4°C were common), poor insulation, and large changing temperature gradients across the magnet. In E989, temperature stability and uniformity in the hall is a high priority. The HVAC system will hold the hall stable and uniform to $\pm 1°$ C during data collection periods. This is at least a factor two more stable than E821. Also, the thermal insulation around the magnet will be improved, and heat flow from gaps around the magnet coil cryostats will be eliminated. These major improvements reduce the temperature-induced changes in the field by a factor of two.

The RMS difference in field average predicted from the fixed probes and that measured by the trolley was roughly 100 ppb in E821, where trolley runs were taken approximately every 3 days. For the same time interval between trolley runs in E989, this RMS difference should be reduced by a factor 2 given the improvements in the hall floor, HVAC, and insulation. Assuming the improvements only reduce the RMS difference to 70 ppb, the goal of 30 ppb on field interpolation with the fixed probes can be achieved by more frequent trolley runs. In E821 the interval between trolley runs was roughly 3 days, and did not need to be more frequent since the experiment was statistics limited. For E989, this interpolation uncertainty must be reduced significantly compared to E821. Trolley runs which are three times more frequent will reduce the interpolation uncertainty by approximately another factor of $\sqrt{3}$. Improvements in the fixed NMR probes as well as the trolley NMR probes (see Section 15.3.6) should render them less sensitive to temperature variations. OPERA studies of the magnet

indicate a small sensitivity of the difference between the fixed probes and trolley probes to small changes in the magnet current. This is due to nonlinearity in the $B - H$ curves of the yoke and pole pieces, leading to slight changes in the field shape. In E821, the current in the magnet was adjusted based on feedback from the NMR. In E989, due to improved climate control the magnetic field should be much more stable passively, and the feedback corrections (changes to the current) will be smaller. The effect of slight changes in the magnet current on the difference between trolley probes and fixed probes can be measured and compared with the OPERA model. The results of these studies and changes to the field due to temperature changes should allow corrections to be made to the fixed probe readings that incorporate changes to both the magnet temperature and the magnet coil current. The ensemble of these efforts should combine to further reduce the 100 ppb RMS uncertainty in E821 to 30 ppb in E989.

**Uncertainty from the muon distribution**

In the simplest approach, the value of $\omega_p$ entering into the determination of $a_\mu$ is the field profile weighted by the muon distribution. The multipoles of the field, Eq. (15.6), are folded with the muon distribution,

$$M(r, \theta) = \sum [\gamma_m(r) \cos m\theta + \sigma_m(r) \sin m\theta], \tag{15.7}$$

to produce the average field,

$$\langle B \rangle_{\mu-\text{dist}} = \int M(r, \theta) B_y(r, \theta) r dr d\theta, \tag{15.8}$$

where the moments in the muon distribution couple moment-by-moment to the multipoles of $B_y$ (expressed in terms of the free proton precession frequency). The determination of $\langle B \rangle_{\mu-\text{dist}}$ is more accurate if the field is quite uniform (with small higher multipoles) so the number of terms is limited, and the muons are stored in a circular aperture, thus reducing the higher moments of $M(r, \theta)$. This simple approach to determining a weighted average requires correction because closed-orbit distortions perturb the radius of the stored muon beam around the storage ring azimuth.

In E821 the weighted average was determined using two techniques. One used a muon tracking calculation and a field map to determine the field seen by each muon. The second determined the average field from the dipole and quadrupole components of the magnetic field coupled with the beam center determined from a fast-rotation analysis. These two agreed extremely well, validating the choice of a circular aperture and the $\pm 1$ ppm specification on the field uniformity that were set in the design stage of the experiment. Part of the E821 muon distribution uncertainty came from radial and vertical offsets of the beam. These offsets couple with normal and skew quadrupole moments of the field. For E821, these corrections were of order 12 ppb for the skew quadrupole (limited by the RMS scatter of the skew quadrupole), and 22 ppb for the normal quadrupole. The latter was limited primarily by a lack of knowledge of the muon beam radial position on a run by run basis. Sextupole and higher skew multipoles of the beam were less than $10^{-3}$ in E821 and did not require correction. No correction was made for the 11 ppb normal sextupole field contribution in

E821. These techniques worked quite well in E821, and the uncertainty on $\langle B \rangle$ weighted by the muon distribution was conservatively estimated as $\pm$ 30 ppb [7].

In E989 we anticipate several improvements. First, the muon beam distribution will be monitored every fill with higher precision by the fast rotation analysis and new muon trackers. Second, improved field uniformity and improved magnet stability (so the multipole decomposition is more stable) will couple with the improved knowledge of the beam. The combined improvements will reduce the normal and skew quadrupole uncertainties, which were 12 ppb and 22 ppb in E821, to below 10 ppb for E989. By measuring and correcting the normal sextupole contribution to 20% or better of its value (which was left as a 11 ppb uncertainty for E821), that contribution can be made negligible. The effects due to these higher multipoles should also be reduced due to higher field uniformity and stability, and by moving the outer trolley probes to a slightly larger radius. Measurements of the higher multipoles will also be made before the vacuum chambers are installed with the shimming trolley (discussed below), and the influence of the vacuum chambers on the field will be determined. The increased knowledge of the field and muon positions around the ring afforded by these system upgrades will be fully exploited with full tracking calculations in the analysis.

To summarize, improved field homogeneity and stability, as well as improvements in muon tracking techniques and efficiency afforded by considerable advancements in computing power since E821 should allow E989 to achieve 10 ppb uncertainty on the muon distribution contribution to the determination of $\omega_p$.

## 15.3.1 General trolley requirements

In the following sections, we will first specify the requirements on the trolley for E989 based on the field mapping tasks outlined above, then discuss the conceptual design of future upgrades and efforts related to the trolley system in detail.

As can be seen from Table 15.1, trolley related systematic errors in the BNL E821 experiment were significant and require improvement to meet the physics goals in E989. The two main sources of uncertainty stem from the calibration procedure of the trolley probes to the plunging probe (90 ppb) and errors related to position uncertainties during the actual trolley runs (50 ppb). Additional smaller effects (like temperature or voltage drifts) were grouped into one systematic error (Others) together with non-trolley related systematics in the field measurement. For the new E989 experiment, the trolley system will be used in a very similar fashion to E821. Given the required improvements in the overall systematic errors for the field measurement, we will need some changes for the new system.

**Trolley measurement of $B_0$**

In E821, the uncertainty on the trolley measurement of $B_0$ was 50 ppb (see Table. 15.1), due primarily to nonlinearities in the trolley position readout. This 50 ppb uncertainty will be reduced to 30 ppb in E989 by mitigating these nonlinearities with use of a barcode reader system. The uncertainty of this improved system will be less than 5mm, a considerable improvement over E821. Second, uncertainties due to trolley rail irregularities will be reduced, as discussed below. Third, a more sophisticated feedback algorithm to stabilize the magnet

during trolley runs will be developed. Fourth, the uncertainty on the field integral in azimuth depends on position uncertainty coupled with field gradients. In E989 we aim to reduce the field gradients in azimuth by a factor of two compared to E821. These steps should reduce the uncertainty on the trolley measurement of $B_0$ to 30 ppb in E989, as discussed in detail below.

The requirements for the actual measurement during a single trolley run remain the same as in E821. An individual NMR frequency measurement will have a precision at least as good as 20 ppb as was achieved in E821. The field will be measured at 6000 points around the ring for each probe. A single trolley run should be accomplished in at most two hours. While about 1 hour is required for the mapping of the 6000 data points for each probe, the return trip can be sped up to reduce the interruption of the spin frequency measurement. Trolley runs should be repeated more frequently than in E821 where an interval of 2-3 days was typical. Increased frequency of trolley measurements will reduce the error associated with the fixed probe interpolation and reduce uncertainties associated with temperature changes in the storage ring.

As mentioned above, uncertainties in the transverse position of the trolley and longitudinal nonlinearities coupled with field gradients are a major systematic error category in the measurement. While we plan on having improved overall shimming in E989 and hence reduced gradients, we will also put effort into reducing the position uncertainties. In E821 the longitudinal position of the trolley during field mapping was inferred from two sources. First, the unwinding of the trolley cable was measured by optical rotary encoders in the drums (see Fig. 15.13). Second, the observed change in the NMR frequency in the fixed probes due to the small but measurable changes in the magnetic field induced by the trolley (maximally in the vicinity of the onboard electronics). The optical encoder read out diverged from perfectly linear behavior maximally by a few cm, and this contributed a 50 ppb systematic uncertainty on $\omega_p$. Together with improved azimuthal field homogeneity (see section 15.8), a more precise longitudinal position resolution in E989 will reduce this uncertainty to negligible levels compared to the overall error on $\omega_p$.

During its movement, the trolley rides on two rails, which determine its transverse position with respect to the center of the muon distribution. The rails were not continuous at the junctions between adjacent vacuum chambers. Slight misalignment of neighboring rails at these gaps led to possible tranverse deviations of the trolley's center introducing an estimated systematic error of 10 ppb. In E989 we will reduce these misalignments and precisely verify the deviation of the rails from their nominal position around the full azimuth. Here, we will employ two methods, namely (1) optical survey with precision laser tracking and (2) the introduction of known (measured), transverse gradients by means of the pole surface coils during dedicated special trolley runs. Further considerations related to uncertainties due to the knowledge of the trolley's transverse position are discussed in Section 15.3.5.

During the calibration, relative position uncertainties between the plunging and trolley probes contribute to the overall systematic error. In E821, the transverse reproducibility was estimated to be 1 mm, whereas the relative position uncertainty in azimuth was determined to 3 mm. Together with field gradients, this resulted in systematic error contributions of 20 ppb and 30 ppb, respectively. For E989, we aim to cut these contributions in half (at least in the azimuthal direction) by more precise alignment of the probes' active volumes in a repeatable way. For this, we plan to allow positioning of the plunging probe in all

three directions and perform careful testing of the calibration transfer from the absolute calibration probe to the trolley in a homogeneous solenoid test magnet (see Section 15.3.9) before data taking. Additionally, precisely known gradients at the calibration station will be induced with the surface correction coils to allow systematic studies of the probes' active volumes.

Other effects contributed to the E821 measurement of $B_0$ with a summed contribution of 50 ppb. These included the temperature and trolley power supply voltage dependence of the NMR measurement and an estimate of the influence of higher multipoles. The dependence of the FID frequency measurement on the supply voltage of the trolley was measured to be 270 ppb/V and a voltage stability of 50 mV was achieved. In the new experiment, a modern power supply will significantly reduce the voltage drift and make this contribution totally negligible. We will also reduce the effects of external temperature changes on the extracted NMR frequency. The new NMR probes will be less sensitive to temperature variations. In addition, an increase in the heat dissipation of the trolley would reduce the change of its temperature during the measurement. Overall, temperature-related effects should be much smaller in E989, and we can carefully study them in the solenoid test magnet under controlled temperature conditions.

It should be noted that any additional modifications must not disturb the field observed by the trolley NMR probes at an appreciable level. The maximal distortion of the field caused by the trolley electronics in E821 was about 2 ppm and future changes cannot introduce any major additional magnetic contribution compared to this level.

In the following sections, we will describe the baseline design for future upgrades and activities that are aimed to meet the above outlined requirements for the E989 experiment.

## 15.3.2   Garage

The trolley garage shown in Fig. 15.12 is attached to one of the vacuum chambers and serves the purpose of storing the trolley inside the vacuum outside the muon storage aperture during the main periods of muon spin precession measurement. A set of threaded rods driven by a non-magnetic piezo motor provides the mechanism to move cut-outs of the rails into the muon storage region and retract them.

The system has been tested recently at Argonne National Laboratory and preliminary findings indicate the mechanical system is in good health and will not require repairs or major changes. More rigorous testing will be performed to understand if this level of mechanical integrity can be relied upon for the lifetime of the experiment. The lack of electronic motion stops at both end positions of the rails has possibly put stress on the mechanics over the course of the E821 operation. Adding position indicators at these two extreme positions of the garage with feedback into the new motion controller system (see Section 15.3.4) will allow for smooth stopping of the rails following translation from or to the parked position. We will use slotted optical sensors as position stops. Since this equipment will be housed near the storage volume, the elected option must comply with the non-magnetic and low-current requirements so that the magnetic field homogeneity is not disturbed. This will be verified with a combination of studies in the test magnet (see section 15.3.9) and calculations. In addition, the piezo-electric motor will be replaced with its successor model from the same company. Spare motors for both the garage and drive mechanism will provide redundancy

over the life of the experiment.
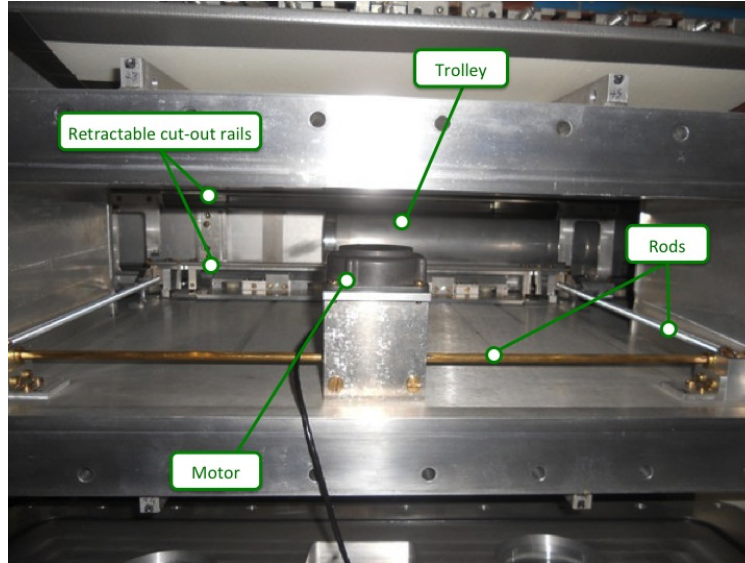


Figure 15.12: Trolley garage with the piezo motor, the driving rods, the rails and the trolley partially in the parking position where it can be retracted from the storage region.

As can be seen in Figure 3.5, the trolley garage is attached to one of the twelve vacuum chambers. Since the upgrades to other systems (such as the alignment of the trolley rails) will require work on the vacuum chambers, upgrades to the garage will be coordinated with these other activities over the next two years.

### 15.3.3  Drive

The trolley drive mechanism shown in Figure 15.13 is located about 120° away from the garage. It is connected to one of the vacuum chambers via a long port and sits on the inner side of the storage ring. It will be moved from its previous 1 o'clock location to a new 9 o'clock (see Fig. 11.1) location to accommodate the incoming muon tracker station. The drive contains two cable drums that are each driven by a piezo-electric motor. Two cables are required to pull the trolley a full 360 degrees in both directions during the NMR measurement of the storage field and the return trip. Since the cables remain attached to the trolley during its storage in the garage, one of the two cables passes through the kicker region. To prevent any damage to the onboard trolley electronics from electronic pickup on the cable from the kicker pulses, this cable is a non-conducting fishing line. The other cable is an all-copper double-shielded cable with an outer coating suitable for in-vacuum operation. This cable provides the power, reference frequency signal and the communication with the trolley microcontroller. The drive mechanism also incorporates one optical rotary encoder for each drum to monitor the angular motion and tension sensors measuring the pulling force on the cables.

All relevant mechanical and electrical components of the trolley drive have been tested individually and are in good health. The electrical components, their functions and planned
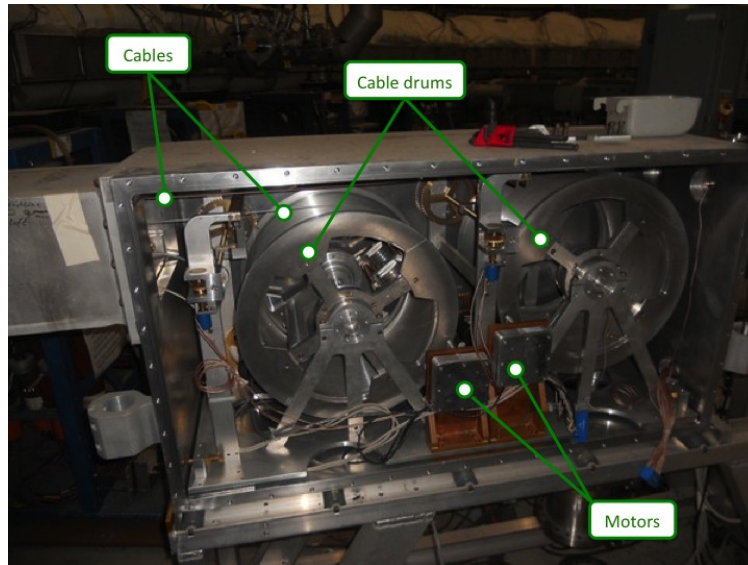
Figure 15.13: Trolley drive with the cable drums, motors and cables.

upgrades are described below:

- **Two piezo motors and drivers**: One motor controls the motion of each drum that houses either the coaxial cable or the non-conducting fishing line. These motors and their drivers will be upgraded to the most recent and supported commercial model. This upgrade will allow for a quicker return trip of the trolley and therefore an improved duty cycle for the muon spin precession measurement.

- **Two optical encoders**: These sensors record the rotation of each large drum. As they only communicate via RS232, we plan to replace them with units that can readily communicate with the new motion controller (see section 15.3.4) via the modern Synchronous Serial Interface (SSI) protocol. Due to the large size of the drum, the encoder position readings are not perfectly linearly related to the motion of the trolley. However, this system will only serve as a cross-check to the trolley's primary longitudinal position determination with a barcode reader (see section 15.3.5) and to verify the trolley's movement is as expected.

- **Two tension sensors**: These units monitor the force on a guiding wheel imparted by tension on the trolley cables. This will be used as-is in a feedback system with the motion controller to reduce the motor speed when the cable tension exceeds a defined threshold. The threshold will be set far below the point where any of the two cables could disconnect from the trolley which would require access to the vacuum chambers and cause a longer downtime during experimental data taking.

The above components have all been successfully tested independently, and in E989 the full system will be operated and moderated by the 8-axis commercial motion controller unit DMC-4183 from Galil as described next.

### 15.3.4   The new motion control system

The control of the piezo-electric motors and readback of associated sensors for the trolley garage, drive and the plunging probe was based on the Siemens SAB80C535 microcontroller in E821. As this microcontroller is obsolete today, we will replace the control system with one single 8-axis Galil DMC-4183 motion controller[4]. This new central unit is schematically depicted in Figure 15.14 and will interface with all five motors from the drive (2 motors), garage (1 motor), and the plunging probe (2 motors). Feedback from the additional sensors will allow to program appropriate operation for each system. Two additional axes are spares for future extension or as replacement in case of failure of one of the five motor channels.
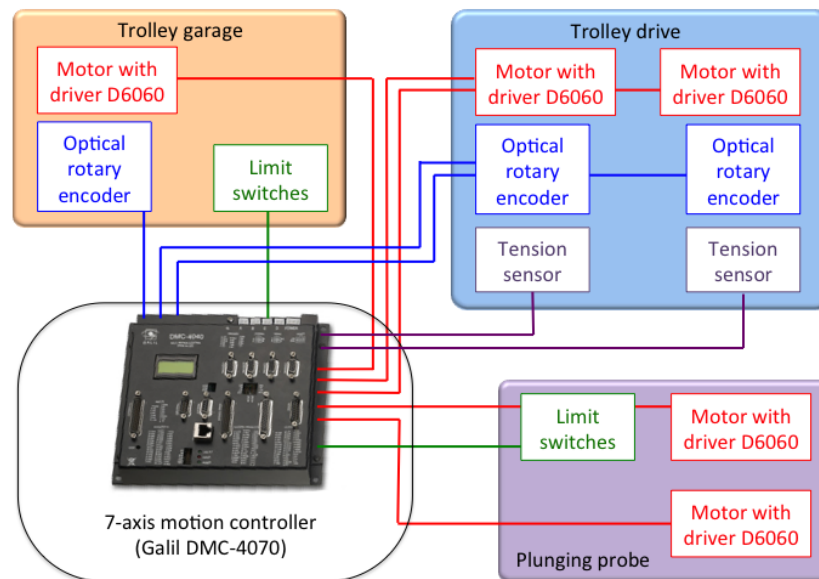


Figure 15.14: Schematics of the new integrated motion control system for the trolley garage, drive and the plunging probe. Central unit for the control is a 8-axis Galil DMC-4183 motion controller which also interfaces to the various feedback sensors.

The Galil motion controller was chosen based on its wide range of applications with motors and encoders and in-house experience with this specific device. The employed Shinsei non-magnetic piezo-electric motors (USR60) require a DC voltage of 12V (max. 4A current) which will be provided by separate power supplies. The control of the motor's spinning direction requires two TTL signals (clock- and counterclock-wise) and a variable DC voltage (0 - 3.2 V) sets its speed. Each axis on the Galil provides such signals in form of a $\pm 10$ V signal which can be split by a small adapter board built in-house to generate the two required signals for the driver. Replacements of the current 24-bit absolute rotary encoders will be interfaced by the motion controller by ordering its interconnect module with an available SSI option. The possibly added incremental encoder on the garage motor comes with an

---

[4]http://www.galilmc.com/products/dmc-41x3.php

ABZ-phase output which can be processed by the Galil DMC-4183 by default. Each axis of the motion controller has two limit switch inputs for the forward and reverse direction of the associatied motor. Their activation will immediately inhibit the current motion of the motor. This feature will be used for the trolley garage where we add new limit switches to allow for smooth stopping at the end positions of the rails and the plunging probe mechanism which is already equipped with such limit switches.

Once the motion controller has been purchased, we will start the implementation of the programming in conjunction with the integration of the above mentioned hardware. While the plunging probe is a system by itself, the garage and drive mechanisms can be interlinked in this new control scheme. Parking and restoring the trolley into the storage area requires the simultaneous movement of the garage motor as well as appropriate (un-)winding of the cables. In the implementation phase, we will program such integrated motion control for these systems and test their functionality with a mock setup of one vacuum chamber with the garage, the trolley drive and a dummy trolley. In the initial phase, programming of the Galil system will be facilitated by using the free GalilSuite software from the vendor. In-house experience at Argonne will help to develop a first version of a basic motion control quickly. In the long-term, integration into the MIDAS data acquisition will be achieved by using the C++ libraries for Linux available from Galil.

### 15.3.5   Position Measurement

The measurements of the trolley's position in both the longitudinal and transverse directions relative to its motion plays an important role in the evaluation of several systematic error sources. Uncertainties in the trolley's position convoluted with the local field gradients give rise to uncertainty in determining the average $B$ field over the ring. The same effects introduce uncertainty in the cross-calibration with the plunging probe.

As stated in the requirements section 15.3.1 above, some improvements in the determination of the trolley's position compared to the E821 experiment are necessary. Together with the better shimming of the magnet (see section 15.8) and hence reduced field gradients, this will significantly reduce position related systematic errors for E989.

During the calibration procedure of the trolley probes in a specially shimmed region in the ring, the plunging probe and the trolley probes (more precisely their active volumes) must be positioned repeatedly at the same position. The uncertainty in E821 for the relative azimuthal alignment was estimated to be 3 mm. The NMR probe active volumes relative to their trolley housing will be calibrated with deployment of precisely known gradients with active surface coils. The trolley itself was positioned by eye in E821, and so we foresee improvements here by means of a well-defined stop mechanism or an external laser survey system viewing a fine positioning grid through the viewing port. The plunging probe from E821 had motion limited to the vertical and radial directions. Adding motion in the azimuthal direction inside the vacuum chamber will also help in reducing position uncertainties in calibration (see Section 15.4.1).

While the trolley moves on the rails around the ring, the transverse position of the 17 NMR probes relative to the central muon orbit is mainly defined by the precision alignment of the rails. In a recent analysis with E821 trolley data, we have studied the effects of the azimuthal variations of the first higher multipoles of the field. Decomposition of these

multipole distributions into a finite series of orthogonal functions allowed an analytical study of the coupling with possible rail displacements. The worst-case scenario of in-phase coupling of rail distortions with the largest quadrupole moment while maintaining consistency with the E821 spec of less than 0.5 mm rail deviation gives a maximal systematic shift of 50 ppb. For E989, reduction of the azimuthal variation of the field by improved shimming will reduce this by a factor of 2 or more. Special focus during the shimming needs to be placed on the dominant quadrupole variation to significantly reduce this systematic uncertainty.

Since the rails are a mechanical system tied to the vacuum chambers, special focus in the chamber alignment will be needed to meet the precise rail alignment of $\pm 0.5$ mm or better. For that purpose, we have developed an alignment strategy for the rails together with the metrology group at Fermilab. After mechanical improvements of the rail fixture, curvature, and positioning inside the vacuum chambers are performed in conjunction with other work on the cages, these stringent alignment requirements must be verified. We anticipate a combination of two measurements to have a consistent cross-check of the trolley's transverse movement. The first verification is based on precision survey of the trolley on the rails by means of laser tracking. After mapping the shape of all individual rail sections with this method, the rail location inside the chambers are referenced to external markers mounted on the chamber walls. Once all chambers are mounted in the storage ring, these external markers will allow to determine the final position of each rail since FEA modeling showed that the deflection of the chamber walls is small when evacuated. We are currently developing the specific implementation of all required steps together with the metrology group at Fermilab with a test setup. A second technique to measure the trolley's transverse position involves imposing radial and vertical gradients using the surface coils to observe the changes in the trolley NMR probe readings around the ring.

In E821 the longitudinal position measurement of the trolley was achieved with a combination of optical rotary encoders and potentiometers monitoring the cable unwinding as well as the response spikes in the NMR frequency of the fixed probes due to the passing electronics of the trolley. The overall estimate of the longitudinal uncertainty was about one centimeter. We aim to reduce this uncertainty to 5 mm or better by refurbishing an onboard barcode reader that was mostly unused in E821 due to unreliable operation. As can be seen in Figure 15.15(a), the vacuum chambers are equipped with marks around the ring. The continuously spaced marks have a spacing of 2.5 mm while the larger spaced, unique patterns serve as absolute reference marks.

Figure 15.15(b) shows the basic principle of the barcode reader. A pair of an LED and a photo-sensor (CLOCK) is placed over the regular marks and is constantly sensing the photo-current. At the detection of a transition edge between marks, the onboard microcontroller in the trolley (see section 15.3.7) sees an interrupt and pulses two additional LEDs. Both of these are offset in the direction of motion from the CLOCK LED. One of the LEDs and its photo-sensor (DIR) are also above the regular pattern marks. In combination with the CLOCK sensor, this determines the relative trolley position and its direction of movement. The readout of a third LED / sensor pair (CODE) above the unique marks allows for determining the absolute trolley position at the occurence of those patterns.

For E989, we will build a new barcode reader board to achieve the required longitudinal position measurement. In a first step, we are designing a stand-alone new barcode reader centered around a Microsemi SmartFusion evaluation kit. This will be mounted on a small

(a) (b)
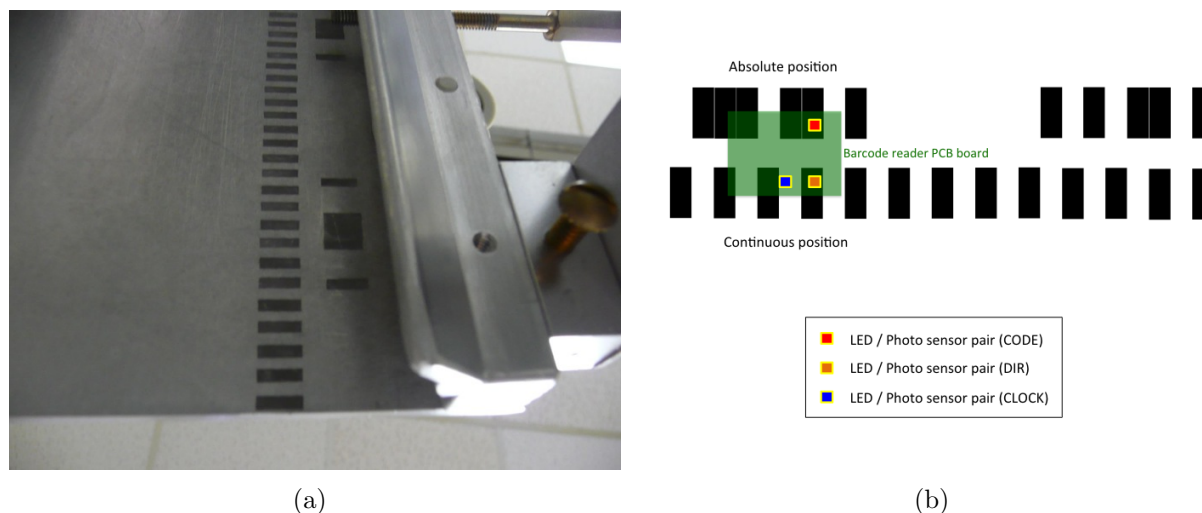
Figure 15.15: (a) Trolley bar code marks on vacuum chamber plate. (b)

carriage that can be pulled through individual vacuum chambers by hand or with the trolley drive. With available ADC channels on-board, full digitization of the entire barcode marks and their contrast level will be performed. Based on the results, we can empirically determine whether the contrast level is high enough to have a fixed threshold for detecting a pattern transition. This is important as the current trolley electronics is based on such a fixed threshold. We will also optimize the optical arrangement of the LED and sensors using the proto-type barcode reader with full digitization. Once a reliable operation with the existing barcode marks has been proven, the optimized prototype will be adapted to match the trolley electronics interface and meet the non-magnetic requirements. As we have the electronics schematics from E821, this is a straight-forward task. Then, the system will be tested for reliability and that it works under vacuum without overheating.

### 15.3.6 Probes

The 17 trolley NMR probes (see Figure 15.2(b)) are identical to the fixed probes. No major work should be necessary for future use in E989 except for the standard fabrication procedure performed by collaborators from the University of Washington. These activities (see section 15.2.1) will include filling with petroleum jelly, tuning for operation at 61.79 MHz, and impedance matching to the $50\,\Omega$ cable as well as testing of a normal NMR response at $1.45$ T. To reduce the uncertainties in the absolute calibration of these probes, minor changes to the coil windings and sample may be made so that the active volume of the probes is better defined. This can be achieved by restricting the sample to the most homogeneous part of the field produced by the coil $L_s$, and by ensuring the number of windings and their positions in the 17 probes are identical.

Alternate distributions of the NMR probes within the trolley (see Figure 15.8(b)) were studied and the configuration used by E821 already heavily overconstrains the determination of the important multipole amplitudes present inside the homogeneous field. Therefore, no

change to the probe configuration inside the trolley is necessary.

## 15.3.7   Frequency Measurement

The NMR frequency measurement for the 17 NMR trolley probes is all integrated into the onboard electronics which were developed for the Brookhaven E821 experiment. At its heart sits the Motorola $68332\mu$C microcontroller with a multitude of functionality. Power, RS232 communication, and the NMR reference frequency are multiplexed over a single double-shielded co-axial cable. The remaining NMR components (RF pulse amplifier, multi- and duplexer, signal preamplifier and frequency counter) are all integrated into the trolley housing together with temperature and pressure sensors and the barcode reader. The development of this minimally magnetic, low-power and low-noise system was a major effort in E821. Preliminary tests in June 2014 of individual components of the electronics have not revealed any obvious damaged components.

As the central microcontroller in the existing E821 electronics is outdated, it will be replaced with a modern SmartFusion2 chip from Microsemi which comprises both an ARM processor and an FPGA. In addition, full digitization of the NMR signal will replace the zero-crossing counting implemented in hardware in the old electronics. This will make the trolley readout compatible with the rest of the NMR probes used in E989. Depending on the maximum bandwidth of the current communication interface over the coaxial line, an upgrade of the communication protocol and interface might become necessary to facilitate offloading the increased data rate to the DAQ computer.
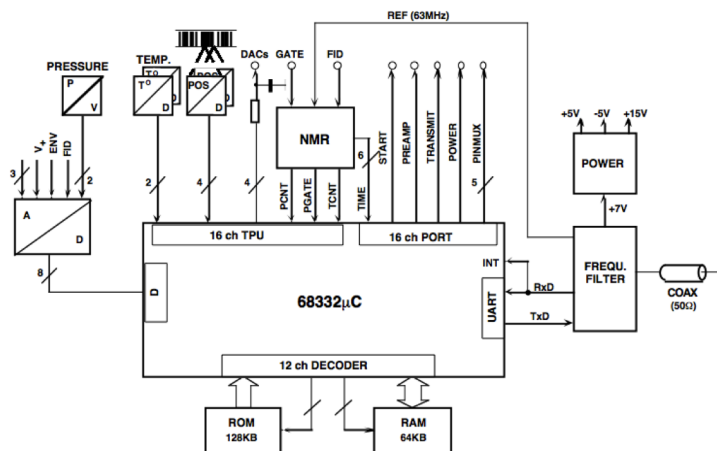


Figure 15.16: Schematics of central electronics on board of the trolley.

Even the low electric power of less than $1\,\mathrm{W}$ leads to changes in the temperature of the trolley electronics and the probes of a few °C over the course of a trolley run. As the measured NMR frequency is temperature dependent, minimization of the temperature changes will help to reduce the associated systematic error. The influence of the temperature on the NMR measurement will be carefully studied in a test solenoid (see section 15.3.9). We also started investigating whether more heat can be dissipated via radiation to the vacuum

chamber walls by increasing the surface emissivity of the trolley and by adding additional heat sinks to optimize the heat flow. Finally, reverse-direction trolley runs will provide a powerful *in situ* test temperature-dependent effects.

## 15.3.8 Trolley DAQ

The DAQ computer communicates with the onboard microcontroller using the RS232 protocol over the single co-axial cable connected to the trolley. A new DAQ computer will perform this function in E989 and will provide all necessary user interfaces to execute commands on the trolley microcontroller. The same DAQ infrastructure will be used to communicate with the trolley drive, garage and the plunging probe mechanism via the new motion controller as described in Sec. 15.3.4.

## 15.3.9 The 4T test solenoid

The homogeneity of the magnetic field must be known to the 70 ppb level for the new E989 experiment. Achieving this precision goal requires economical testing of the NMR equipment over prolonged periods at a precision of greater than 20 ppb. This requires a magnetic field of 1.45T with high stability and homogeneity. The main purpose is the testing of the in-vacuum NMR trolley system and a precise reevaluation of the absolute calibration probe (see Section 15.4.1).

The most stringent requirement for the magnet comes from the plan to repeat a careful evaluation of the absolute calibration probe at the nominal B field of 1.45T for $g - 2$. As the overall aim is a reduction of 50 ppb to 34 ppb as was achieved in a 1.7T field with the same probe [6], the gradients and drift should be significantly smaller than this goal. The envisoned tests will include both systematic studies of the NMR measurements with the same probe under changing external factors (e.g. temperature, power supply voltages, ...) and the comparison of different probes at the same location within the magnet. The latter requires a stability of the field when probes are swapped at the level of 10 ppb in order to be negligible with respect to the precision goal of these studies. Assuming that probes can be placed into the center of the test magnet at time intervals of 3 minutes, the 10 ppb requirement translates into a maximal allowable drift of 200 ppb per hour.

The field gradients coupled with uncertainties in the positioning of a probe also limit the reproducibility between exchanges of probes. Individual probes can be positioned with an accuracy of ± 0.5 mm on a well designed platform. Together with the 10 ppb specification above, we therefore can tolerate gradients of no greater than 200 ppb per centimeter in a typically few-centimeters large calibration region at the center of the test magnet.

In order to test the trolley system, the bore of the magnet must be large enough to conveniently fit the device. The most stable and homogeneous magnets available are persistent MRI magnets which have a solenoid field. Due to the orientation of the NMR probes inside the trolley, the current 50 cm long trolley would need insertion perpendicular to the axis of the magnet. At minimum a bore size of 60 cm is required to accomplish that. The active volumes of the NMR probes are located 8 cm away from one end-cap. Hence, a bore of about 90 cm would be ideal to operate the probes in the most homogeneous center of the magnet.

Table 15.3 summarizes these requirements for the planned E989 systematic studies being performed in this magnet. The last column shows the specifications of an available Oxford OR66 magnet which is shown in Figure 15.17.

|  | Requirement for E989 | Oxford OR66 magnet |
|---|---|---|
| Magnetic field | 1.45 T | $\leq 4\,T$ |
| Stability | $< 200\,\mathrm{ppb/hr}$ | $90\,\mathrm{ppb/hr}$ |
| Homogeneity at center | $< 200\,\mathrm{ppb/cm}$ | $\sim 10\,\mathrm{ppb/cm}$ |
| Bore diameter | $> 60\,\mathrm{cm}$ | 68 cm (with gradient coils) |
|  |  | 90 cm (w/o gradient coils) |

Table 15.3: Requirements for the E989 and specifications for the Oxford OR66 magnet at full field of 4 T. The quoted homogeneity is achieved with passive and active shimming which requires the gradient coils being installed as they contain the active shim coils.

This magnet has been shipped cold from its former medical research application in a VA hospital in San Francisco to Argonne. An outside company will ramp the magnet up to 1.45 T and will shim the shape to reach its optimal homogeneity. We are currently designing a suitable platform to insert the trolley and other stability monitoring NMR probes to support the calibration procedure. This configuration will also allow studyies of various systematic uncertainties and characterizations of ferrous properties of materials being considered for use in the experiment. A temperature controlled enclosure will help to understand the temperature dependence of the NMR frequency extraction.



Figure 15.17: The 4T, test solenoid OR66 from Oxford Instruments inside building 366 at Argonne National Laboratory waiting for installation.

The test magnet will be available for NMR related studies during the entirety of the $g-2$ experiment's lifetime. Especially in the early phase during the installation and shimming

of the $g-2$ storage ring, it will be solely dedicated to the extended NMR tests described above. Once the $g-2$ usage reduces, we have the freedom to make this test facility available to other users. Since the magnet power supply came with the magnet, we can infrequently ramp the field to other desired values. That offers the flexibility for the $g-2$ collaboration to come back with dedicated studies at 1.45 T even during data taking periods. For example, a careful repetition of the calibration probe's evaluation at the end of data taking will be an important and desired cross-check to complete the analysis.

# 15.4 Absolute calibration of the magnetic field

## 15.4.1 Necessity for calibration

The magnetic field map of the storage volume is made by the trolley, using pulsed NMR on protons (see section 15.3). However, these protons are not free - they are in hydrocarbon molecules in a macroscopic sample of petrolatum, which in turn is surrounded by probe materials - teflon, copper wire, and aluminum, all of which perturb the magnetic field at the proton. For each trolley probe $i$ at location $\boldsymbol{r}_i$, these perturbations must be measured and a correction $\delta_i$ applied to the raw Larmor precession frequency $\omega_{\mathrm{raw}}^i(\boldsymbol{r}_i)$. Then the free proton precession frequency, $\omega_p(\boldsymbol{r}_i)$, can be extracted from the raw measurements, $\omega_{\mathrm{raw}}^i(\boldsymbol{r}_i) = (1 - \delta_i)\omega_p(\boldsymbol{r}_i)$.

The procedure that determines the individual corrections $\delta_i$ for each trolley probe is called absolute calibration. This is the third major field measurement task outlined in Sec. 15.1.5.

This absolute calibration of the trolley probes is performed with two special NMR probes; the plunging probe and absolute calibration probe (see Figs. 15.2(a) and 15.1(a)). The probes used for BNL E821 absolute calibration (see [6]) can be used for E989, though improved versions are being developed for comparison and to reduce some systematic uncertainties. The details are described below.

**Absolute calibration probe**

The Larmor angular precession frequency of a proton in a pure water sample in the absolute calibration probe $\omega_{\mathrm{probe}}$ is related to the Larmor precession frequency of a free proton at the same location, $\omega_p$, by a total correction factor $\delta_t$,

$$\omega_{\mathrm{probe}} = (1 - \delta_t)\omega_p, \text{ where} \tag{15.9}$$
$$\delta_t = \sigma(\mathrm{H_2O}, \mathrm{T}) + \delta_b + \delta_p + \delta_s. \tag{15.10}$$

Contributions to $\delta_t$ come from the diamagnetic shielding of protons in a water molecule $\sigma(\mathrm{H_2O},\mathrm{T})$, the shape- and temperature-dependent bulk susceptibility of the water sample $\delta_b(T)$, paramagnetic impurities in the water sample $\delta_p$, and the magnetic field from the magnetization of paramagnetic and diamagnetic materials in the probe structure, $\delta_s$ [6]. These correction are discussed below.

The absolute calibration probe has a near-spherical water sample ($\delta r/r < 1\%$, see Figs. 15.1(b)) and is described in detail in [6]. The Larmor angular frequency observed

of a proton in a spherical water sample is related to that of the free proton through [11, 1]

$$\omega_L(\text{sph} - H_2O, T) = [1 - \sigma(H_2O, T)] \, \omega_L(\text{free}). \tag{15.11}$$

Measurements of $\sigma(H_2O, T)$, the temperature-dependent diamagnetic shielding of the proton in a water molecule, are described in [15, 23, 14] with the result:

$$\sigma(H_2O, T) \;=\; [25.680(2.5) + 0.01036(30) \times (T - 25.0°C)] \times 10^{-6}. \tag{15.12}$$

The bulk correction in Eqn. 15.10 is given by $\delta_b(T) = (\epsilon - 4\pi/3)\,\chi(T)$ in cgs units, where $\epsilon$ is a sample shape dependent factor and $\chi$ is the susceptibility of water $\chi(H_2 0)= -0.720(2) \times 10^{-6}$ [24]. The temperature dependence of $\chi(H_2O)$ has been measured [25]:

$$\chi(H_2O, T) = \chi(H_2O, 20°C) \times \left(1 + a_1(T - 20) + a_2(T - 20)^2 + a_3(T - 20)^3\right), \tag{15.13}$$

where $a_1 = 1.38810 \times 10^{-4}$, $a_2 = -1.2685 \times 10^{-7}$, and $a_3 = 8.09 \times 10^{-10}$ for $T$ in Celsius. A spherical sample shape is used in the absolute calibration probe because the shape-factor for a sphere $\epsilon = 4\pi/3$, which eliminates the bulk magnetic susceptibility correction, $\delta_b = 0$. (For an infinitely long cylinder $\epsilon = 2\pi$ when the axis is perpendicular to $\vec{B}$. The precession frequency observed using a cylindrical water sample should be 1.508(4) ppm higher than that of a spherical sample in the same field.) The sphericity of the glass bulb containing the water sample was measured for BNL E821 with an optical comparator, and corrections were made to $\delta_b$ [6]. Corrections were also made for bubbles or excess water in the neck of the sample, and other imperfections. Using pure, deionized, degassed, multiply-distilled water in the absolute calibration probe reduces $\delta_p$.

Several techniques can be applied to reduce the magnitude and uncertainty on the remaining corrections. The presence of impurities can be monitored by measuring the magnetization time-constants $T_1$ and $T_2$ using appropriate pulse sequences. The perturbation due to probe materials $\delta_s$ can be minimized by using material with low susceptibility and testing them for magnetic impurities. The residual influences must be measured so that $\delta_s$ is known at the 10 ppb level or better. Tight mechanical tolerances ensure symmetry about the cylindrical axis of the probe and reduce the sensitivity to the orientation of the probe [26]. Symmetry about the midplane helps make the lineshape symmetric (reducing time-dependence in the FID zero-crossing rate).

These techniques were applied and the properties of the absolute calibration probe developed for LANL E1054 and BNL E821 were measured carefully at LANL in a very stable MRI solenoid at 1.7 T so the absolute field in terms of the free proton precession frequency was determined by the probe to an accuracy of 34 ppb [6]. Measurements made by the absolute calibration probe were expressed in terms of the equivalent free proton frequency at 1.45 T to a reduced precision of 50 ppb in BNL E821. The main reason for the reduced precision was uncertainty in the probe temperature during the absolute calibration procedure. The precision will be improved for FNAL E989 to the 35 ppb level proven for LANL E1054 as discussed below.

First, the properties of the absolute calibration probe which were determined in the E1054 solenoid at 1.7 T to an accuracy of 34 ppb [6] will be repeated through extensive testing in the MRI solenoid at Argonne at 1.45 T. By constructing a thermal enclosure for use in the

solenoid with 0.1 °C stability, and with a higher performance ADC for the FID, the properties of the absolute probe should be determined at least as well as E1054, but now at the correct field for E989 and with greater control over the temperature. Another improvement is that construction of a new calibration platform will allow a few additional probes to be used to track the changes of the solenoid field during these calibration studies. The new platform will exchange probes with sub-mm position uncertainty, with the perturbation to the local field minimized and measured. These procedures should reduce the uncertainties on the absolute calibration probe from 50 ppb in E821 to 35 ppb in E989.

The absolute calibration procedure is performed with the ring up to air. It involves measuring the field at a fixed location in the ring with the center trolley probe, moving the trolley away, then measuring the field at the same location with the absolute calibration probe (which is mounted on a G10 support attached to a vacuum chamber flange). This is performed at times of the the day when the experimental hall temperature and magnet are most stable. The probe temperature will be monitored and determined with less than 0.5 °C uncertainty in the absolute temperature so the associated uncertainty in the diamagnetic shielding is less than 5 ppb. Calibrations performed at different temperatures should be consistent once the known temperature-dependent changes in shielding are accounted for.

An additional shift of the calibration in E989 versus those in the solenoid at LANL arises due to the presence of magnetic images of the magnetized probe materials and water sample of the absolute calibration probe which appear in the high-$\mu$ iron of the pole pieces. These effects are at the level of 40 ppb and were insignificant for BNL E821, but they will be determined as part of the calibration procedure in E989. This will be done by inserting a small diameter NMR probe (like one of the trolley/fixed probes) between the g-2 storage ring pole pieces. The shell of the absolute calibration probe (after removing the water sample) will be placed around the small probe, the field will be measured, then the shell removed and the field measured again by the small probe. The shift in field measured by the small probe yields $\delta_s$ in Eqn. 15.10. Measuring $\delta_s$ a function of the height above the pole pieces accounts for most of the magnetic image effects. These shielding effects will be compared between measurements made in the Argonne solenoid and the storage ring and cross-checked with predictions.

It is important to note the same absolute calibration probe intended for use in E989 was used in LANL E1054 to determine $\mu_\mu/\mu_p$ [3]. By using the same absolute calibration probe as E1054, there is a direct robust link of our E989 magnetic field to the muon magneton; proton NMR has only the role of a intermediate fly wheel. This link is independent of possible future changes in fundamental constants in the regular adjustment procedures [1], unless the muon magneton will be remeasured better experimentally or the theory-dependent value of $\mu_\mu/\mu_p$ is used to extract $a_\mu$. In these case $\mu_\mu/\mu_p$ is largely independent of the properties of the probe. This link is important if the value of $\mu_\mu/\mu_p$ directly extracted from the muonium experiment is used to extract $a_\mu$. The same probe will also be used as part of the calibration of the new J-PARC muonium experiment, which should reduce the experimental uncertainty on $\mu_\mu/\mu_p$.

Finally, as an important cross-check, we are developing a second absolute calibration probe using a spherical water sample but with several improvements. First, the water sample will be contained in a spherical shell made from machined Macor hemispheres. Prototype shells were constructed, the interiors were filled with a casting material and the casts ex-

amined on a Suburban Tool MV-14 $10\times$ optical comparator, with a Mitutoyo micrometer, and from analysis of images taken with a CMOS camera. The interiors were spherical to $\delta r/r \leq 0.5\%$, where an asphericity of $0.5\%$ leads to a fractional uncertainty $\delta B/B \approx 15$ ppb [17]. The machined shell incorporates a sealable plug, eliminating the long glass stem that lead to line broadening in E1054/E821. Other improvements: to reduce $\delta_s$, the probe shell will be made of a zero-susceptibility combination of thin aluminum (paramagnetic) and copper (diamagnetic) cylinders, or will be omitted completely, reducing the pole-piece image effects. Smaller, non-magnetic tuning capacitors than those of the E1054/E821 probe will be used, and moved farther from the sample, reducing $\delta_s$. Near zero-susceptibility wire (from Doty Scientific) will be used for the coil. The coil itself will be wound with a slight non-uniformity to achieve higher RF uniformity over the water sample, and by the reciprocity principle, give a more uniform $B$ field measurement. The sample will be held and the coil wound on thin-walled cylinders of low-susceptibility material (Macor, Pyrex or quartz). This probe will be compared with the E1054/E821 probe and will provide some redundancy and reduce risks in case of loss or damage. The reduced susceptibility and greater sphericity should lead to smaller systematic uncertainties. Having two probes to compare many times will provide an important check on the stability of the absolute calibration. The use of a precision cylindrical absolute calibration probe is also being considered.

## Cross-calibration of the trolley with the plunging probe

The calibration of the trolley involves shimming a section of the storage magnetic field to be as uniform as possible. This is important because absolute calibration involves measuring the field at the same location with a trolley probe, then a calibration probe. If the field is not uniform, then a difference in the trolley and calibration probe positions leads to the probes measuring different fields. This effect can not be separated from the calibration offset $\delta_i$ which is sought. Improving the field homogeneity reduces the requirements on probe positioning accuracy.

Good local field homogeneity is achieved by tailoring the surface correction coil currents temporarily to reduce the multipoles locally. Additional sets of coils (on the other side of the surface coil PCBs and/or on coils between the pole pieces and yoke) will be used to remove gradients in the azimuthal direction. This shimming needs to be done only over a restricted volume that encompasses the active volumes of the trolley probes.

Ideally, the field in the homogeneous field region is measured by the trolley probes; then the trolley is moved away and the absolute probe determines the field at the locations just measured by the active volumes of the 17 trolley probes. The magnet is stabilized during this procedure, which is repeated many times. Since the absolute probe is too large to reach all of the locations measured by the trolley probes, an intermediate probe called the plunging probe is also used (see Fig. 15.2). The plunging probe must be calibrated by the absolute calibration probe.

To cross calibrate the trolley probes with the plunging probe during E821, the field was measured by the 17 trolley probes at the calibration location. The trolley was moved away, and the plunging probe, which sits on the end of a 1 meter long, hollow G10 arm, was moved in the radial and vertical directions to measure the field at the locations formerly occupied by the trolley probes. The difference between the measurements calibrates each trolley probe

with respect to the plunging probe (after correcting for drifts in the field at the level of 100 ppb, which were measured by fixed probes $\approx 10°$ away from the calibration location).

Errors in the E821 calibration arose from uncertainties in the azimuthal positions of the probes, uncertainties in the transverse positions of the probes, and uncertainties in the comparison of the trolley probes with the central trolley probe which is calibrated directly by the absolute calibration probe.

In the azimuthal direction, errors in the E821 calibration procedure arose both from uncertainties on the positions of the centers of the active volumes inside the trolley along its axis (unknown at the level of a few mm) and of the trolley itself. The position uncertainty on the location of the active volumes of the calibration probes was also at the 1 mm level. Coupled with field gradients in the azimuthal direction gave a 30 ppb contribution to the uncertainty in the relative calibration.

In the transverse plane, the trolley probes are fixed with respect to the frame inside the trolley that holds them, and variation in the trolley transverse position is restricted below a mm by the rail system on which it rides. The vertical and radial positions of the trolley probes with respect to the plunging probe are determined by applying a sextupole field with the surface coils and comparing the change of field measured by the two probes. Magnetic field inhomogeneities of order 20 ppb/mm in the calibration region used in E821 (see Fig. 15.10(b) and Table 15.2) coupled with radial and vertical position uncertainties of order 1 mm to give a 20 ppb uncertainty. Field drifts and uncertainty in water sample temperature also contribute to the uncertainty.

Each trolley probes was calibrated against the plunging probe approximately 6 times in the 2001 run of E821. The RMS scatter of these 6 measurements of the relative calibrations of each probe versus the center trolley probe, averaged about 140 ppb. The resulting uncertainty on the relative calibration was estimated as 70 ppb, and is consistent with the uncertainty expected from the positional uncertainties described above.

The calibration of the center trolley probe with respect to the absolute calibration probe had an uncertainty of 50 ppb, so the total trolley probe calibration uncertainty was 90 ppb (the sum of 70 and 50 ppb in quadrature).

Changes to this procedure can reduce the relative calibration uncertainties to 30 ppb for E989. For E821, the plunging probe and G10 rod were inside a close-fitting metal tube with an enclosed end, and were operated in an air atmosphere. The tube was attached to a titanium bellows that allowed the probe to be translated in the radial and vertical directions in the calibration region, while the storage ring remained under vacuum. However, the probe could not be translated in azimuth. Since the trolley could not be positioned with high precision in the azimuthal direction, there were uncertainties at the few mm level between the plunging probe azimuthal position and the those of the active volumes of the trolley probes (which were not visible from the exterior).

Another limitation of the E821 trolley calibration with the plunging probe was due to the metal bellows and other parts of the plunging probe translation mechanism. These would move when the plunging probe position changed, perturbing the field at the location of the plunging probe at the 10 ppb level. To reduce this perturbation for E989, the bellows and metal sheath will be removed and the plunging probe operated in vacuum. This reduces the total mass of moving material significantly, reducing the local perturbation to the field, including those from magnetic images, during calibration. The residual perturbation will be

measured.

Another improvement will be to provide 3-dimensional positioning of the plunging probe with sub-mm accuracy. This will be done with three high-vacuum compatible, non-magnetic linear translation stages. The stages will provide simultaneous radial motion of 25 cm, vertical motion of 10 cm, and azimuthal motion of 2.5 cm, and will be driven by the same non-magnetic Shinsei USR60-E3N ultrasonic motors with encoders, Shinsei D6060S drivers and Galil controller as the trolley drive and garage.

In addition, the trolley position during calibration will be controlled and measured more precisely than E821 by using physical stops and/or optical survey or other high accuracy position readout of the trolley and plunging probe positions. A system under study consists of several CMOS cameras which observe the plunging probe from roughly 50 cm away with $\geq 15°$ field of view. Translation of the probe with respect to fiducial markers in the calibration region can be detected with the imaging system, allowing the probe position in 3 dimensions to be determined by triangulation. With a $2592\times 1944$ pixel array on a non-magnetic board camera (such as the Leopard Imaging LI-OV5640-USB-72) and low-distortion optics, sub-mm position resolution is possible. The trolley position can also be determined with the same camera system, enabling sub-mm relative position accuracy.

Another improvement is that the locations of the active volumes of all the trolley probes will be made more uniform by adjustments to the coil windings and sample position. The active volumes will be determined beforehand in the Argonne MRI solenoid to sub-mm accuracy [5], and precision fiducial marks on the exterior of the trolley will be added. This will allow positioning of the trolley and plunging probe active volumes with mm accuracy or better. Also, by aligning the active volumes of the trolley probes in azimuth to within a mm, the volume which needs to be shimmed for calibration is reduced.

Finally, we anticipate automating these procedures with the closed-loop positioning system outlined above so each trolley probe can be calibrated dozens or even hundreds of times. By reducing the position uncertainties on the trolley probe active volumes to a millimeter or less in azimuth, vertical and radial, and by positioning the trolley and plunging probe with millimeter or better accuracy during calibration, the position uncertainties will be reduced by a factor two or more compared to E821. The RMS scatter of relative calibration measurements should be reduced from 140 ppb achieved in E821 to less than 100 ppb assuming no improvement in the field shimming. Using petroleum jelly in the trolley probes, which has greater immunity to evaporation than water and a susceptibility with a smaller temperature dependence, might reduce this RMS scatter even further, and improved hall temperature stability will help. In addition to these steps, significant attention will be paid to monitoring the probe temperatures, and additional coils might be used to further reduce local field gradients and changes during calibration. By automating the trolley probe calibration and taking dozens of measurements, field drifts can be averaged out and the error on the mean can be brought down to 30 ppb.

In a similar way, the RMS scatter of 50 ppb in E821 on the absolute calibration of the center trolley probe should be reduced. By automating and repeating the calibration

---

[5]By superimposing a field gradient in azimuth, the location where the line center does not shift determines the effective center. The linewidth will be broadened and give some information regarding the size of the active volume.

many times, the goal of calibrating the central trolley probes with respect to the absolute calibration probe to an accuracy better than 20 ppb should be achievable. This provides a redundant check on the calibration of several of the trolley probes.

We note that the calibration with the plunging probe can be done with the ring under vacuum as many times as is necessary during E989. If necessary, calibration with the absolute calibration probe can be done with the ring backfilled with nitrogen to reduce effects due to the paramagnetism of $O_2$ which appear at the level of 30 ppb (which can be measured as in E821). Calibration with the absolute probe will be done before and after muon data-taking, and any time the ring is let up to air. More frequent absolute calibration will be performed if necessary to achieve a total trolley calibration uncertainty of 30 ppb.

## 15.4.2 $^3$He Magnetometry

We plan to develop a second absolute calibration probe using the NMR signal from polarized $^3$He to cross-check and possibly replace the water-based absolute calibration probe.

There are several potential advantages to using hyperpolarized $^3$He in place of distilled water in an absolute calibration probe, which will lead to reduced systematic uncertainties. The diamagnetic shielding factor (see equation 15.10) for $^3$He has been calculated to be $\sigma_{^3\mathrm{He}} = 59.967\ 43(10) \times 10^{-6}$ [1]. While the shielding correction is larger than for $H_2$ and $H_2O$, the uncertainty is much smaller, and the temperature coefficient is about 100 times smaller [24, 40]. The dependence on the shape of the $^3$He volume is much smaller, unlike the water sample which has to be spherical (the precise impact of cell-shape effects will be investigated). With a gaseous sample, motional narrowing eliminates line-shape distortion and the FID produces a Lorentzian line shape whose center is well defined. For $H_2O$ the line shape must be analyzed in the same way as reference [14] in order to accurately transfer the calibration.

Our experience with hyperpolarized xenon suggests that that signal-to-noise is comparable to the E821 $H_2O$ calibration sample. NMR with hyperpolarized $^3$He produced by laser optical pumping is also practical because the NMR signal per atom is of order $10^5$ times larger than that from protons at 1.5 T, compensating for the much lower concentration in the gas phase. Another advantage is that samples can be made smaller, e.g. 5 mm diameter and thus average the field over a smaller volume. Finally, the magnetic images of a $^3$He probe in the E989 pole pieces would be smaller than for a water probe because of the lower electron density, leading to smaller systematic shifts.

Given the advantages above, we expect the field can determined in terms of the $^3$He precession frequency with smaller systematic uncertainties than water. To get an absolute calibration in terms of $\omega_p$ would require knowledge of $\mu_{^3\mathrm{He}}/\mu_p$, the ratio of magnetic moments of a free $^3$He to a free proton. However, the most precisely measured related quantity is $\mu'_{^3\mathrm{He}}/\mu'_p = -0.761\ 786\ 1313(33)$ (4.3 ppb), the magnetic moment ratio of a bound $^3$He to that of proton in a spherical water sample [18, 1]. Still, since this ratio is known to 4.3 ppb, measurements with the water-based absolute calibration probe should agree with a $^3$He based probe to 4.3 ppb. Performing this cross-check would be quite valuable. Therefore we plan to develop an independent absolute calibration probe based on a $^3$He sample. This will be carried out at Oxford, working with Michigan and other collaborators. The aim is to use this to verify the calibration of the water-based absolute calibration probe using the test

magnet described in section 15.3.9. This will lay the ground for the possible use of $^3$He as a magnetometry standard in the future. Further work to measure $\mu_{^3\text{He}}/\mu_p$ or $\mu_{^3\text{He}}/\mu_B$, would also be very valuable.

Hyperpolarized $^3$He can be provided from a spin-exchange (SEOP)[42, 41] or metastability-exchange (MEOP)[43, 44] set up. The Michigan group have extensive experience with SEOP and have worked closely with MEOP systems and will cooperate with expert groups at Ecole Normal Superieur and Simon Fraser, and Oxford, to develop an effective system. A decision of which pumping technique to use will be taken in 2014.

The MEOP approach has advantages for the calibration because it can be applied at room temperature and therefore in-situ in the probe. In the MEOP scenario, a turnkey 1083 nm laser light from a fiber laser (*e.g.* Keopsys CYFL-GIGA series) is distributed to each of the probe cells by a fiber. A discharge is struck in the cell to produce the excited state. Polarization of 10% or more is expected in a few minutes. A second option is hyperpolarized $^3$He produced in a separate cell and transferred to the calibration cells through PFE tubing similar to the polarizers we have used for medical imaging work [45]. In either scenario, the dominant corrections, which are small, will arise due to cell-shape effects ($\delta_b$ in equation 15.10), i.e non-sphericity of the cell, but more importantly the polarized gas residing in any tubing or pull off left over from the cell filling procedure.

High-field hyperpolarization magnetometry using the MEOP technique will be developed at Michigan working with long-term collaborators on a search for the electric dipole moment of Xe atoms [46] and medical-imaging work [47]. One of the challenges is producing high magnetization at high field (signal-to-noise is proportional to magnetization, i.e. the product of polarization and gas density). High-field MEOP polarization of $^3$He has been recently studied by the ENS group [48, 49], who show that, due to higher polarization rates, nuclear polarization, of 80% at 1.33 mbar and 25% at 67 mbar, have been achieved. The magnetization at 67 mbar is essentially identical to protons in $H_2O$ at 1.5 T, though the signals may be slightly smaller due to the difference of gyromagnetic ratios (32.4 MHz/T for $^3$He and 42.6 MHz/T for protons).

The development work at Michigan will make use of our 1.45 T magnet and will enable probe development, polarization, and studies of temperature dependence similar to those planned for petroleum jelly. SEOP polarized samples are also under consideration, and we have significant experience in these techniques and equipment.

## 15.5 Feedback to the magnet power supply

A feedback system similar to E821 will be used to stabilize the storage ring magnetic field at the 1 ppm level or below. This is the fourth major field measurement task outlined in Sec. 15.1.5.

Without feedback, the field in the storage volume will change due to changes in the magnet current, mechanical distortions of the magnet (floor shifting, mechanical creep of magnet yoke, poles, or cryostat), and from changes in the magnet gap from thermal expansion/contraction of the yoke and poles. Both mechanical and thermal distortions should be reduced compared to BNL E821 due to the greater mechanical stability of the thick, monolithic concrete floor, and much improved experimental hall temperature stability $\pm2°$F, and

improved magnet insulation.

The storage ring magnet power supply can be set with 17 bit resolution (7.6 ppm). The current is regulated by a Bruker DCCT in the power supply, providing long term current stability of 0.5 ppm (8 hours) and ± 0.3 ppm or less over several minutes to several hours. Fine regulation of the current (much finer than the 7.6 ppm resolution of power supply DAC) is achieved by sending a current through the additional "Trim" input winding around the DCCT core, which effectively changes the current set point.

The magnitude of the required trim current is determined using the fixed probe NMR system. Field measurements from a subset of fixed probes are averaged, then compared with a desired field set point. This is done in real time in software on the NMR DAQ PC. Since the mechanical and thermal time constants of the magnet are very long (hours), and since the Bruker power supply has excellent short term stability, this error signal does not need to be determined faster than 1 Hz. In BNL E821, the error signal determined the setting of a 12-bit Jorway Model 31 (voltage output) DAC residing in a CAMAC crate, that was sent to the DCCT trim input. This scheme achieved $\mathcal{O}(1)$ ppm level of stability. In E989, the CAMAC crate and Jorway DAC will be replaced with a stable 16-bit current output DAC board in the NMR VME crate or a separate PCIe or USB board on the NMR PC, or a Keithley 6220 current source. The latter has the advantage that it can be positioned near the power supply DCCT, and controlled remotely by GPIB or RS-232. This avoids long cable runs of the analog feedback signal which would be susceptible to noise pickup.

The gain of the DCCT trim input winding will be determined in bench tests before the end of 2014. The optimal feedback loop scheme and loop coefficients will be determined once the magnet is cold and powered, before data-taking, through Zeigler-Nichols or other established tuning schemes. Field perturbations for tuning schemes can be introduced through a single coil winding on the inner radius of the vacuum chamber of the outer cryostat. A coil in this location produces a field similar to that from the outer coils, and ppm scale perturbations can be introduced with currents of a few hundred mA in a single winding.

Feedback will be used during muon data-taking, trolley runs, and probe calibration. With a more stable thermal and mechanical environment for the magnet, and an optimized feedback loop, we anticipate better magnetic field stability in E989 compared to BNL E821, and sub-ppm stability should be achievable.

## 15.6 Time-dependent perturbations to the $B$ field

In BNL E821, ramping of the AGS magnets changed the field in the experimental hall by $\approx$ 0.5 mG (34 ppb) over each cycle. The proton beam was extracted and muons were stored during the flat-top of the cycle, with no effect on the g-2 measurement. However, during the ramp up or down, the field in the storage volume changed by roughly 10-15 ppb as measured by the fixed probe NMR system [10]. The main effect is thought to be due to fields produced by currents induced in the outer mandrel [32]. Calculations which treat the magnet as coupled transformers formed by the mandrels and coils, but ignore any other effects (such as skin effects), predict field perturbations of order 25 ppb.

For E989, time-dependent magnetic fields from sources such as the Booster accelerator, and power lines could perturb the field in the storage ring at the ppb level. The error

budget for these fields is 5 ppb, and we have carried out extensive studies of the 15 Hz Booster field, transient magnetic fields in MC1, and induced fields from cars and trucks [33]. These measurements began before building construction, and have continued through the re-assembly of the storage-ring magnet. A complete discussion of the Results and Opera 3d simulations are reported in g-2 note #66 [36], and are summarized below.

The principal difference between the BNL magnetic environment and that at Fermilab is the fact that at Fermilab the 15 Hz of the Booster accelerator is derived from the 60 Hz powerlines. In BNL E821, muons were injected into the $(g-2)$ ring storage region asynchronous to the 60 Hz AC power, since the AGS operation is powered by a motor-generator, rather than directly off of the LILCO power lines. This feature averaged out any transient magnetic fields induced in the muon storage region by the 60 Hz power lines.

### 15.6.1    Measurements of Transient Fields



(a)                                                         (b)
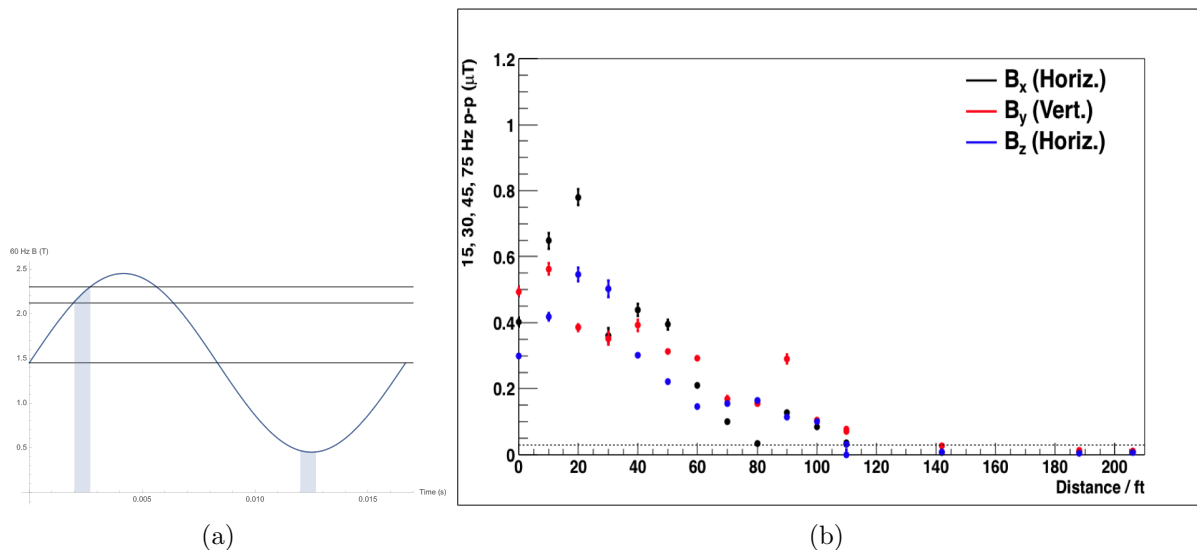
Figure 15.18: (a) An exaggerated 60 Hz magnetic field on top of the 1.45 T storage region field. The middle line shows what the NMR probe measurements average out to, while the shaded regions show the time covered by the first two muon fills from a single Booster batch. The width of the line corresponds to the 700 $\mu$s ($\simeq 10\gamma\tau_\mu$) measurement time. There is a 10 ms time gap between fills of the storage ring. (b) The booster harmonics (excluding the 60 Hz), as a function of distance from the circumference of the Booster. The dashed line shows the 10 ppb level of the 1.45 T magnetic field. On this graph, some points are inside of the booster circumference, and the closest MC-1 wall is approximately at 200 ft.

At Fermilab, the bunch of muons to be stored will then be injected at the <u>same</u> phase of any 15/60 Hz magnetic field. Due to the asynchronous NMR measurement, the NMR probes will average out this time-varying field as the muons travel around the storage ring. Fig. 15.18(a) gives a pictorial representation of the problem. The fills of the ring will be separated by 10 ms, and the measurement time is $\simeq 0.7$ ms (just over ten muon lifetimes),

where ($\gamma\tau_\mu = 64.4$ $\mu$s, and $\tau_{60\text{ Hz}} = 16.7$ ms). The phase of each 0.7 ms measurement period relative to the 60 Hz will be unmeasured, and if unaccounted for, could lead to an error on the magnetic field used in the determination of $a_\mu$.

Because of the close proximity of the Booster Accelerator to the MC-1 building, we measured the 15 Hz Booster field as a function of distance from the Booster toward the MC-1 building. The Booster field vs. distance is shown in Fig. 15.18. It became immediately obvious that the time-varying magnetic field near or inside of MC-1 was dominated by the 60 Hz from the powerlines, and the 15 Hz is negligible at the MC-1 building. We have studied whether this 60 Hz background is large enough to change the central storage-ring field by more than the systematic error budget of 5 ppb, which is 7.25 nT of the main 1.45 T magnetic field[6].

Fourier transforms of thee time varying fields near the booster and in the empty MC-1 Building show that the 15 Hz is almost absent inside of the building, but there is significant 60 Hz, as shown in Fig. 15.19. Analysis of data shows that the booster harmonics are well below the 5 ppb level inside of the empty building, but significant 60 Hz exists there, with the vertical component being roughly 20 ppb [36].



(a)                                                        (b)
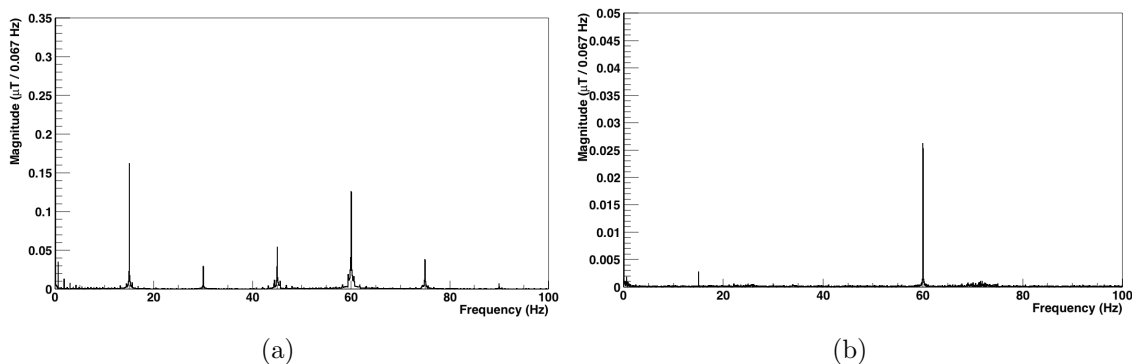
Figure 15.19: (a)An FFT of the magnetic field at a point close to the booster, approximately 160 ft from the edge of the MC-1 building wall. (b) An FFT of the magnetic field at a point inside the empty MC-1 building.

After the storage ring magnet yokes and cryostats were assembled, but before the pole pieces were installed, additional measurements were carried out. The AC fields were measured at the azimuthal center of each yoke sector at the storage region radius $r_0 = 7.112$ m after the iron yokes and cryostats were installed (see Fig. 15.20(a)). The inner yoke radius is $r_{Yi} = 6.832$ m. Measurements were also taken at the same azimuthal locations at the radii represented by the three red circles: $r_1 = 5.61$ m; $r_2 = 4.36$ m; $r_3 = 0.6$ m. Only four points were measured at $r_3$. The results are shown in Fig. 15.20(b) for the center of the Yoke pieces are $r_0$. The final running period at Brookhaven was for $\mu^-$, and the remnant field between the yoke pieces at the muon storage radius of 7.112 m has a residual vertical field that saturated the fluxgate magnetometer (see Fig. 15.20(b)). At radius $r_1$, all components

---

[6]At the time of this writing, there has been preliminary work investigating whether the modification of some NMR probe readout times can help measure this phase difference.

of the transient field were less than the 5 ppb level, except points 8 and 10, which were near operating vacuum pumps.



(a)                                                            (b)
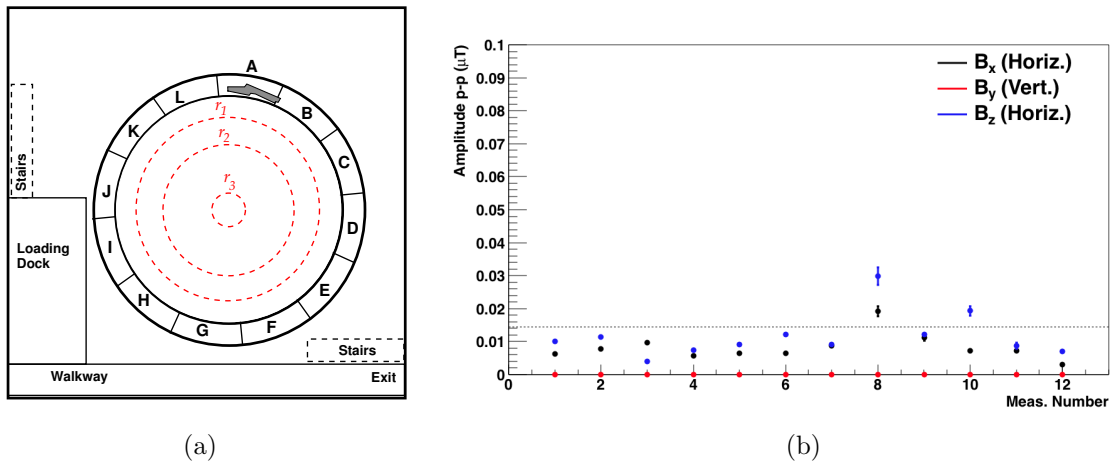
Figure 15.20: (a)Measurement locations for field measurements. The location where the inflector magnet will be installed in yoke sector A is also shown in the sketch. (b)Peak to peak field magnitudes in 3 dimensions for 15 Hz harmonics (including 60 Hz) at the storage radius $r_0 = 7.112$ m.
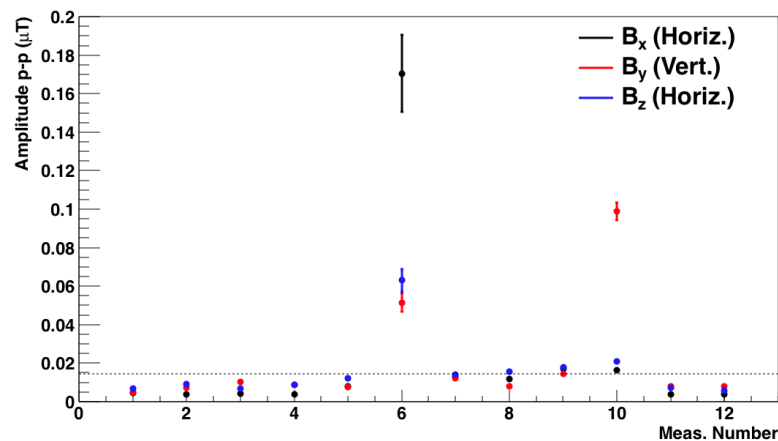


Figure 15.21: Peak to peak field magnitudes in 3 dimensions for 15 Hz harmonics (including 60 Hz) at $r_1$ (4 ft in from $r_{Yi}$). The azimuthal positions corresponded to the center of the yoke pieces (1=A, 2=B, etc.). Points 6 and 10 were located near running vacuum pumps, leading to abnormally large fields. The dashed line represents the 5 ppb acceptable error level. The points far enough from the vacuum pumps lie at, or below, this threshold.

## 15.6.2    Opera Simulations of Transient Fields

An Opera-3d model of the storage ring that included the coils, cryostats, all the iron and the muon vacuum chamber was built. The reader is referred to Ref. [36] for full details. Simulations of vertical transient fields were carried out, with and without the beam vacuum chamber present. A 3° sector of the ring was simulated with axial symmetry. The Opera model is shown in Fig. 15.6.2(a) and the magnetic field is shown in Fig. 15.6.2(b). Once this model was built in Opera, it was used to calculate the effect of a sinusoidal driving field, to determine the shielding factors of the storage ring, with and without the muon beam vacuum chambers installed. The calculated magnetic field at the beam-center height, is shown as a function of radius in Fig. 15.6.2.



(a)                                                                                    (b)
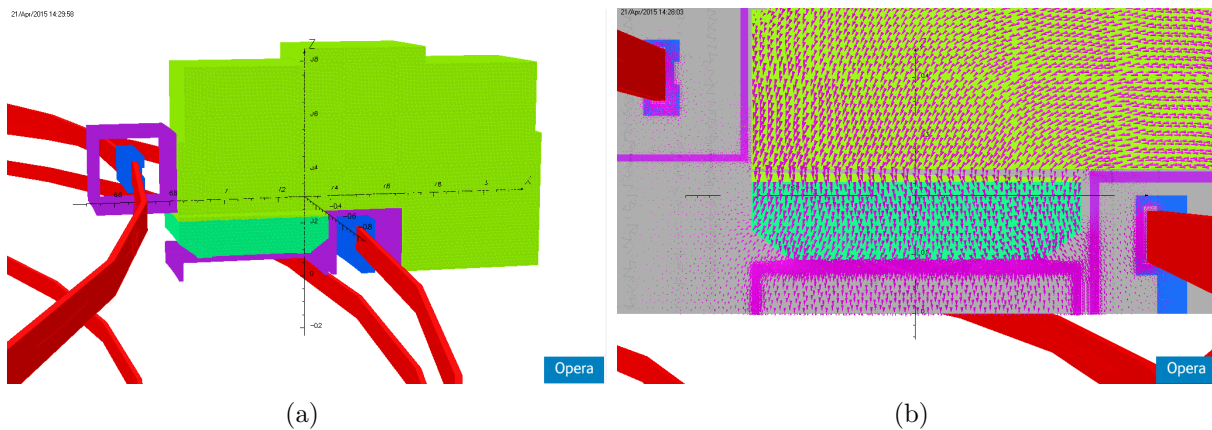
Figure 15.22: (a) A 3 degree section of the ring. In light and dark green are the yoke and pole pieces respectively, with proper B-H curves applied. In red are the superconducting coils, modeled as perfect Biot-Savart conductors driven at 5200 amps. In blue are the cold aluminum mandrels, modeled with the appropriate conductivity [35]. In purple are the aluminum cryostat boxes housing the superconducting coils, as well as a wide section of the beam vacuum chamber. The apparent blockiness of the cylindrical superconducting coils is a function of the OPERA program visualization, and not a representation of how the program performed the calculations. (b)Close up view of of the storage region, with field lines superimposed upon the geometry. One can easily see that the field lines follow the proper path, and there is a nice uniformity across the storage region. The field magnitude at the center of the storage region was calculated to be within less than 1% of the target 1.45 T.

There is a single dielectric stop for the beam vacuum chamber, around which fields will penetrate to a greater degree as induced current flow is restricted. An OPERA model with a 3 mm slice cut out of the the 3 degree section of the vacuum chamber was constructed, and analyzed to study the effect of this discontinuity. The results are shown in Fig. 15.25, which indicates some magnetic field penetration around the slit. We will study this issue further to make sure it will not cause a problem.

(a)                                                    (b)
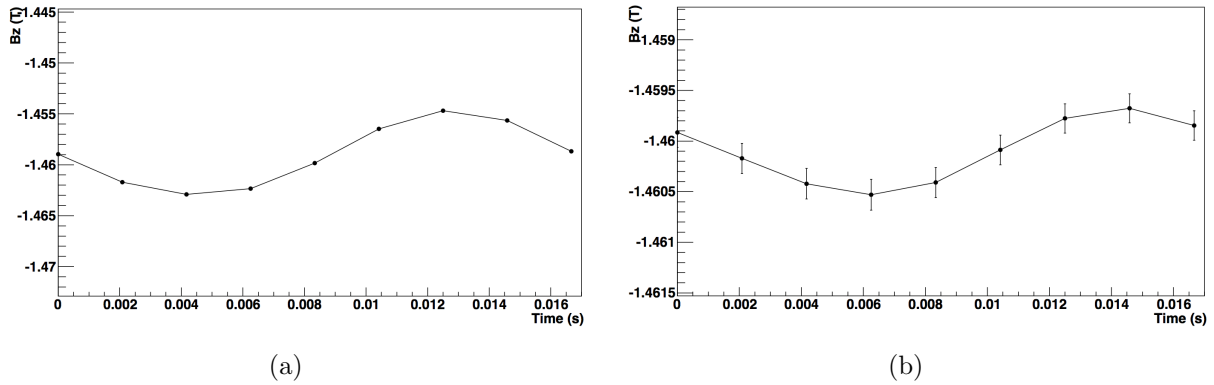
Figure 15.23: (a)The field magnitude in the vertical direction at a single point at the center of the storage volume for a .1 T external driving sine wave field. This result was produced within the OPERA model where the vacuum chamber was absent. Note the reduced magnitude and opposite direction to the free field. (b)The field magnitude in the vertical direction at a single point at the center of the storage volume for a .1 T external driving sine wave field. This result was produced within the OPERA model where the vacuum chamber was present. Compared to the non-vacuum chamber model, the external field is even further reduced, to the point where the solution accuracy is approaching its lower limits. There is also an unimportant phase shift here due to the larger resistance of the vacuum chamber.
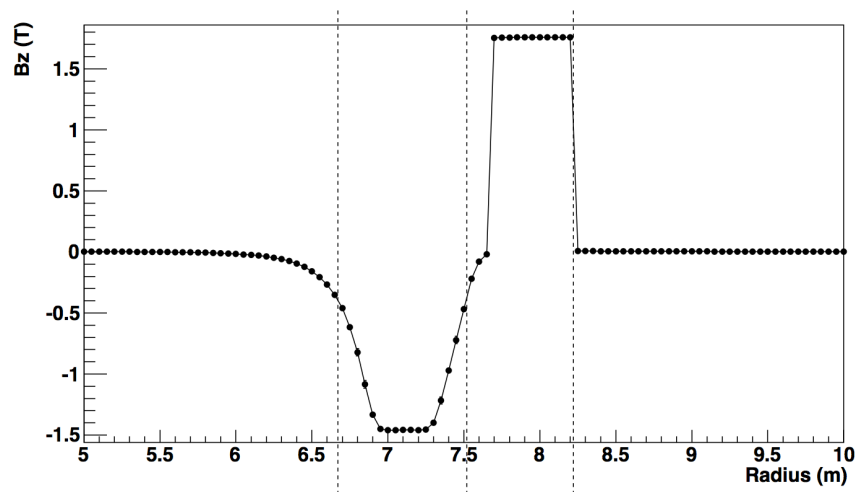


Figure 15.24: Field values for points radially outward from the center of the ring. The first two dashed lines from the left represent the placement of the superconducting coils while the last dashed line shows the location of the outer edge of the iron yoke. The muon storage region is centered at $r_0 = 7.112$ m. Error bars are included in the plot.

## 15.6.3   Summary of Measured and Calculated Fields

The ambient fields in the empty hall have been measured and shown to be of order 20 ppb or less, and calculations show that they are 5 ppb or less with the presence of the ring and
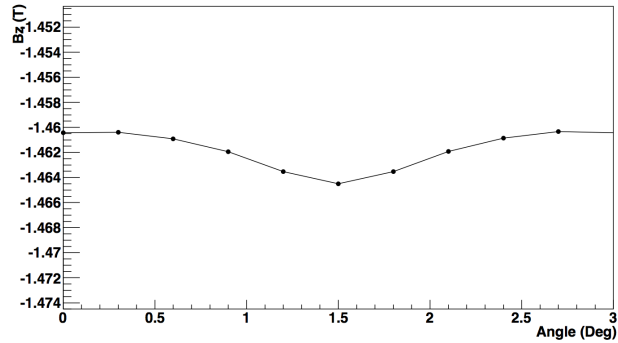
Figure 15.25: Field values for points axially around the 3 degree section of the ring for an OPERA model with a vacuum chamber that has had a slice cut out of it. The vertical field penetrates to a larger degree than the model of a vacuum chamber with no cut. This is for a single time point when the external field is at its maximum. Error bars are included within the plot.

vacuum chambers. With the calculated shielding factors, we are confident in the ability of the ring to passively self shield ambient fields from the booster and powerlines to below the 5 ppb acceptable error level. Even if the ambient fields were a factor of four higher, they will still be shielded out. Still of concern are fields from nearby electronics, which have yet to be measured. If their fields are less than 1 mG at the edge of the vacuum chambers, then the field that penetrates the storage region will be below the 5 ppb level. Those which produce fields greater than this will have to be further shielded in some fashion. The next step is to measure these fields as different electronics are produced in the coming months.
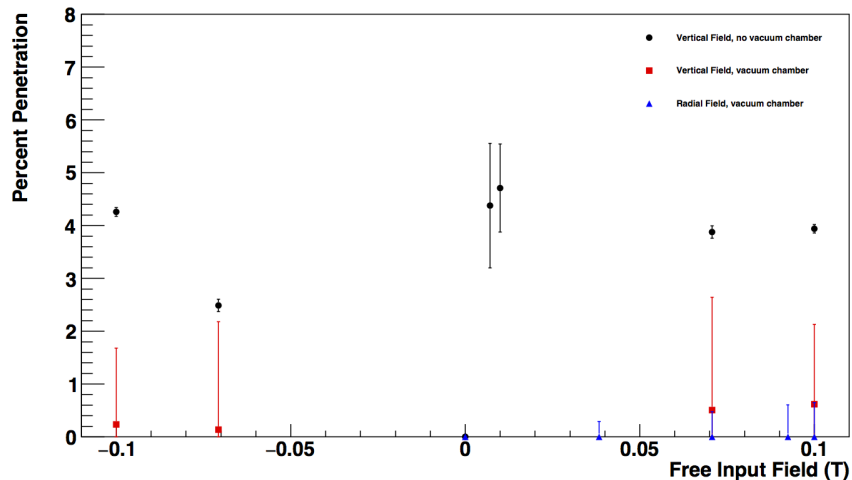


Figure 15.26: Percentages of varying free field values at the center of the storage region for different OPERA 3D models. The shielding of the ring system is shown to passively be quite effective.

The effect of these external fields in E989 can be monitored in several ways. While readings of the fixed probes are asynchronous with accelerator operations and the 60 Hz power grid, they will be time-stamped with an absolute accuracy better than 1 ms. The FIDs have time constants of just a few ms, so fixed probe readings are in principle sensitive to field perturbations at frequencies up to a few hundred Hz. However, the probes are only read out at about 5 Hz, so perturbations at 15, 30, 60 Hz etc will get aliased to additional image frequencies when probe readings are Fourier analyzed.

A scheme of monitoring the transients in the hall with the use of several fluxgate magnetometers has been proposed. We will study that, and other suggestions with additional Opera-3d simulations to determine the most effective method of measuring these transients. We will also have ample time during the shimming process to study these effects, including carrying out shielding studies with fluxgates inside and outside of the vacuum chamber.

We are also concerned about possible effects from the calorimeter and tracker electronics, and we are beginning an active program to study the magnetic fields produced by the electronics as a function of rate.

## 15.7  Other systematic effects on the field determination

Other contributions to the E821 systematic uncertainty on $\omega_p$ are listed in Table 15.4, along with a brief comment on the changes required to meet the E989 goal. The total of these effects was estimated to be 100 ppb in E821 (see [7, 54] and Table 15.1). Details on the sources of uncertainty and how they will be reduced to 30 ppb for E989 are discussed below.

**Kicker Transients:**

One source of field uncertainty in BNL E821 was from transient magnetic fields from eddy currents in the vacuum chambers induced by the pulsed kicker magnet. These field transients were measured in the E821 g-2 storage ring volume, before data-taking, using a magnetometer based on Faraday rotation in a crystal of TGG [53]. The transients affect the kicker region (roughly 5 m out of the 45 m circumference), and were of order 13 mG 20 $\mu$s after the kick, corresponding to a local change of 1.1 ppm [53]. However, the transients decay rapidly so by 30 $\mu$s when data-taking started, and when averaged over the ring circumference, the effect was 20 ppb [54].

For E989, an effort is being made to reduce these transients as a consideration in the new kicker design. Second, rather than being left as an uncertainty, measurements of the transients will be incorporated into the final field result. This can be done with the E821 Faraday magnetometer, which reached noise levels equivalent to a 20 ppb perturbation after some averaging. With more averaging and no other changes, a measurement of the kicker transients can be made with an uncertainty of 10 ppb. This will be done before data-taking with the TGG crystal located in the storage volume.

In E989 additional steps are possible. The Faraday magnetometer performance can be improved by replacing the E821 10 mW Ar$^+$ laser at $\lambda = 514.5$ nm, with an off-the-shelf

| Source of Uncertainty | E821 Magnitude [ppb] | Improvements for E989 | E989 Goal [ppb] |
|---|---|---|---|
| Kicker Eddy Currents | 20 | Average more measurements, reduced transients, improved magnetometer | 10 |
| Higher Multipoles | 30 | Move trolley probes to larger radius, measure higher multipoles | 15 |
| Trolley temperature changes | 45 | Calibration of temperature effects, reduced temperature range | 15 |
| Trolley power supply voltage fluctuations | 20 | Use better power supply, calibration of effects due to voltage fluctuations | 5 |
| Oxygen effect | 40 | Improved measurement of oxygen effects | 10 |
| Image effects | 40 | Reduced susceptibility probes, measurement of image effects | 15 |
| Frequency Reference | 3 | Calibration of effects due to change in reference frequency | 3 |
| Total | $\leq$100 | | 30 |

Table 15.4: Other sources of systematic uncertainty from BNL E821, with changes in preparation to meet the requirements for E989.

405 nm diode laser with 80 mW power (Edmund Optics #64-823 for instance). The Verdet constant at 405 nm (and hence signal) of TGG is more than 50% larger than at 514.5 nm. The higher laser power also improves the ratio of signal to photon shot noise. This allows the transient signal to be measured with a lower noise floor in less time. Measuring the second beam from the polarizing beam cube splitter (analyzer) of E821 doubles the signal to noise and cancels noise from laser intensity changes.

Other improvements being considered are to record the kicker pulse waveforms shot-by-shot so the field transients can be estimated more precisely if the waveforms change. As a redundant check, the Faraday measurements taken inside the storage volume before data-taking could calibrate a second magnetometer positioned slightly outside the storage volume and left in place during data-taking. This would continuously monitor and provide a correction to the field average from kicker-induced transients. The second magnetometer would be build specifically for the transient field measurement, to be sensitive to few mG fields with a bandwidth approaching 1 MHz. This magnetometer could not use the high susceptibility, field-perturbing TGG, but a longer crystal (3-4 cm) of diamagnetic SF59 for comparable performance Using a 405 nm diode laser of a few hundred mW, balanced photodetectors with photocurrents subtracted, AC-coupled, then amplified, can approach mG sensitivity on

time scales of a minute, and reduce the uncertainty on the field average from kicker transients well below 10 ppb. This would be developed and implemented if errors from kicker transients must be reduced below 10 ppb to compensate larger uncertainties in other parts of the field measurement.

**Higher Multipoles:**

In E821 the trolley measured the magnetic field in the muon storage region to a radius of 35 mm. The field beyond 35 mm was extrapolated using the measured multipoles up to and including the normal and skew decupoles. Early in E821 before the vacuum chambers were installed (and well before the final field homogeneity was achieved), the field was measured to 45 mm radius using a special shimming trolley. The multipoles higher than decupoles were measured to be less than 8 ppm at 45 mm, and when convoluted with the falling muon distribution at large radius, gave a maximum uncertainty of 30 ppb from higher multipoles.

In E989, this uncertainty will be reduced to 10 ppb. First, with higher field uniformity and stability, the higher order multipoles should be significantly smaller than the worst case estimate given above. The higher order multipoles will be measured with the shimming trolley to 45 mm so we have a map of the field over the full muon aperture before the vacuum chambers are installed. The influence of the vacuum chambers will measured using a modified shimming trolley that is inserted in regions of the vacuum chambers where the probes can be extended to the full storage aperture (with the chambers at atmosphere). Second, if possible, the beam-tube trolley probes will be moved to slightly larger radius to map a larger fraction of the storage volume, which will also reduce these uncertainties. If necessary, when the ring is up to air, we will make consecutive measurements with the trolley probes rotated around the trolley axis. Combining these field maps allows a direct measurement of the higher order multipoles in the presence of the vacuum chambers. These steps will reduce the uncertainty from 30 to 10 ppb.

On a related note, better tracking and monitoring of the muon distribution will reduce the uncertainties on the convolution of the muon distribution with the field. Also, unlike E821, in E989 the multipoles beyond the quadrupole in the field convolution with the muon distribution, such as the normal sextupole contribution, will be corrected for by including the measured values in the convolution with the muon distribution, rather than leaving these contributions as an uncertainty. Given the expected significant improvements in hall temperature stability, these multipoles should be more stable than in E821.

**Trolley Temperature:**

Changes in the trolley temperature in BNL E821 lead to observed fluctuations in the Larmor frequency extracted from the trolley probes of order 30 ppb/°C. This sensitivity can come from the electronics and from actual temperature dependent changes in the magnetic environment in the trolley and probes. Trolley measurements during E821 were made over a temperature range of 23°C to 30°C, with an RMS spread of 1.5 degrees, for an estimated 45 ppb uncertainty. Within a trolley run, the electronics rose in temperaure by about 4 degrees, the probes by about 1.5 degrees [9].

These temperature effects will be studied extensively in a thermal enclosure in the MRI solenoid at Argonne, so temperature effects can be corrected rather than left as an uncertainty. The temperature dependence of the trolley electronics will be measured. The perturbations to the trolley probe readings from the temperature dependence of the susceptibility of the trolley aluminum shell will be measured (a fractional change in the perturbation of $10^{-3}$ for every 2°C change in temperature is expected). The temperature dependence of the probe response due to temperature dependent changes in the bulk susceptibility and chemical shift of the NMR sample will also be measured. The temperature sensors in the trolley will be calibrated to 0.1°C. Also, the possibility of using petrolatum in the trolley probes will be investigated since its temperature dependence (at least of the bulk susceptibility) might be lower than in water. Changing the trolley probe sample shape to spheres might also reduce the temperature sensitivity (since it eliminates the temperature dependence of the bulk susceptibility of the sample). This will tested in the MRI magnet.

Finally, applying a high vacuum compatible, non-magnetic, high-emissivity coating to the trolley (Cerablak HTP with $\epsilon > 0.9$, made of carbon encapsulated in an aluminum phosphate glass) should lead to a reduction in the temperature rise of the trolley during trolley runs, roughly by the ratio of emissivities, $\epsilon_{\text{E989}}/\epsilon_{\text{E821}} \geq 0.8/0.2 \approx 4$, a minimum of several degrees. This will reduce the magnitude of all temperature dependent changes in the trolley.

Perhaps most important, the much more stable experimental hall temperature in E989 compared to BNL, will reduce the range of temperatures of trolley operation from 7°C in E821 to 2°C in E989. This alone should reduce temperature-related uncertainties by a factor of 3. Between careful calibration of temperature effects, and efforts to reduce the temperature range of the trolley, a systematic uncertainty of 15 ppb should be achievable.

**Trolley Power Supply:**

The E821 trolley power supply operated around 9.9 V and drifted around 50 mV. These fluctuations in the trolley supply seemed to lead to FID baseline shifts and uncertainties in counting of zero-crossings, leading to a voltage sensitivity of roughly 400 ppb/V observed in the probe readings, for an uncertainty of 20 ppb. This will be replaced in E989 with a modern stable linear supply. With and stability and monitoring at the level of 10 mV, this uncertainty should be below 5 ppb in E989.

**Oxygen Effect:**

The oxygen effect is described in [7], and is due to the paramagnetism of $O_2$ which is inside the trolley and perturbs the field seen by the probes. It also affects the plunging probe. The problem arises when the absolute calibration is performed since the ring is then filled with air, creating a different field environment. The resulting correction (which was measured during E821 in the storage ring magnet) is about 40 ppb (with roughly a 20 ppb uncertainty). The correction will be measured again carefully in E989 in the ring and the MRI solenoid for the trolley, plunging probe, and absolute calibration probe. Given the much greater stability of the solenoid, it should be possible to reduce the uncertainty to 10 ppb.

**Image Effect:**

When the plunging probe and absolute calibration probe are inserted in the gap between magnet pole pieces, the field at the NMR sample is perturbed by the magnetic images of the probe materials in the pole pieces. When the probe moves vertically in the storage volume to calibrate the trolley probes, the magnitude of the images change, hence the effective shielding properties of the probe are position dependent. The magnitude of these effects is estimated as 40 ppb from knowledge of the probe materials and their susceptibilities. In E989, the position dependence of the shielding will be reduced by using combinations of materials with near zero susceptibility (see section 15.4.1), and the residual effects will be measured in the ring to reduce the uncertainty to 15 ppb.

**Frequency Reference:**

The frequency extracted from an FID had a small 3 ppb dependence on the synthesizer reference frequency. This will be studied again in E989 to confirm that the effect is small, but not serious enough to warrant any changes. The effect should actually disappear when the FIDs are digitized in E989 and zero-crossings can be interpolated to give fractional clock counts.

In combination, all of the efforts detailed above should reduce the systematics observed in E821 from 100 ppb to 30 ppb in E989.

# 15.8   Magnet Shimming

## 15.8.1   Overview

The main technical objective of the $g - 2$ storage ring shimming is to produce the most uniform field possible. Both the muon distribution and the average field can be described by multipole expansions (see Sec 15.3). The field uniformity requirement is that the field varies less than 1 ppm over the 4.5 cm storage radius. Specifically, each multipole contribution should vary by less than 1 ppm when averaged over azimuth. In order to enhance additional systems within the field measurement, we will aim to reduce the variation of these individual multipole contributions to 100 ppb. Improved field uniformity at any local azimuthal position is also desirable since the performance of the trolley NMR probes relies on keeping the field gradients as small as possible in order to optimize the measurement of the free induction decay (FID) signal (see Sec 15.2.1). Furthermore, small field gradients reduce the uncertainty contribution from the position uncertainty of the probes. Since the probes sample the field over a non-negligible volume, the requirements on knowledge of the position are relaxed if the field gradients are minimized.

The $g - 2$ magnet was designed to produce a field uniformity in the muon storage region of better than a few parts in $10^4$ prior to shimming. This design spec was achieved by using high-quality steel for the magnet yoke, and ultra-low carbon steel (ULCS) for the pole pieces. Upon assembly, the field uniformity was improved by more than two orders of magnitude through a shimming sequence. The general shimming strategy implemented in E821 was two-fold: passive shimming via precision alignment of ferromagnetic materials and active

shimming utilizing current distributions. We will base our general shimming procedure on that of E821 and the experience gained therein, supplemented by modeling results.

The $g - 2$ superconducting coils, yoke, pole pieces, and shims have been simulated with OPERA-2D as well as OPERA-3D [38]. The results of these simulations are compared both with POISSON simulations and results obtained during the development of E821 [27, 28, 29, 30, 31, 37, 39]. One critical aspect of the simulation is the use of realistic B-H magnetization curves. Although the steel is not fully saturated at 1.45 T, the response is not perfectly linear. This non-linearity is partially responsible for generating higher-order multipole moments in the simulations, and must be recognized during the actual shimming procedure. Our OPERA simulations will allow for a sophisticated shimming plan that improves the overall uniformity of the field in E989 compared to E821.

The shimming consists of the following elements: (1) Passive or mechanical shimming using precise positioning of materials, and (2) Active or current-based shimming using surface correction coils. These are discussed in the following sections.

## 15.8.2 Passive Shims

### Shimming Procedure

Passive shimming refers to the set of mechanical adjustments that are performed during the assembly of the ring and remain fixed during the running period. The strategy begins with adjustments far from the muon storage region and work inwards with finer and finer adjustments. The principal passive shimming elements consist of the following:

1. Iron pieces on the yoke

2. Alignment of the pole faces

3. Wedge shims in the air gap between the pole piece and yoke

4. Edge shims in the gap between upper and lower pole faces

5. Iron pieces on the pole surface near the azimuthal gaps between adjacent pole faces

Throughout the physics measurement, the NMR trolley described in Section 15.3 will travel around the ring to map out the magnetic field. Due to the limited space inside the vacuum chambers, the NMR probes inside the trolley only extend to $r$=3.5 cm, which is smaller than the extent of the muon beam ($r$=4.5 cm). However, prior to the installation of the vacuum chambers, more space is available between the pole pieces and a larger trolley will be used. This shimming trolley (see Figure 15.27) consists of 25 NMR probes; one is at the center of the muon storage region, eight are at a radius of 2.25 cm, and 16 are at a radius of 4.5 cm. This allows a mapping that extends to the outer radius of the muon storage region. The shimming trolley probes use the same electronics as the fixed probes.

In E821 the shimming trolley was positioned on the end of a $\approx 7$ meter turntable arm positioned about the center of the storage ring. Rotating the turntable allowed the shimming trolley to map the field at various azimuthal positions. In E989, the trolley will be moved manually or with a small arm and motor.
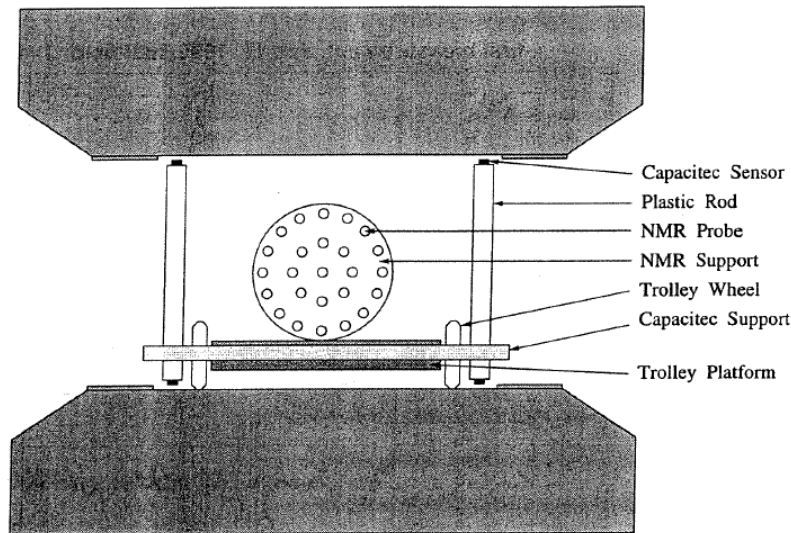
Figure 15.27: Schematic depiction of the NMR shimming trolley situated on a platform. Capacitive sensors on plastic rods help measure the pole piece alignment.

The platform on which the shimming trolley rests also allows for a precision measurement of the vertical gap between the upper and lower pole faces. This information can then be used to re-align the pole pieces ultimately producing a more uniform field. In E821, plastic rods with capacitive sensors on each end allowed for a determination of the relative parallelism between the poles [39]. For E989 the plastic rods might be replaced by quartz rods or other materials with very low coefficients of thermal expansion and low susceptibility. Furthemore, we are upgrading the capacitive sensors to a series whose readings are less sensitive to temperature and contain fewer field-perturbing elements. Careful attention will be paid to systematic effects due to changes in the rod angles and differences in length.

The data from the shimming trolley is analyzed and used to inform the next iteration of mechanical adjustments necessary to proceed to the next stage of the shimming procedure. A two-dimensional slice of the $g-2$ magnet used for `OPERA-2D` simulations is shown in Figure 15.28 for reference.

**Yoke Iron**   The yoke is subdivided into twelve 30° sectors, as described in Section 9.2. Long wavelength azimuthal variations in the field uniformity are addressed by adjusting the positioning of pieces of iron on the outer surface of the yoke. In particular, an increase in the air gap between the top piece of steel and the upper yoke plate (see the label "Air gap" in Figure 15.28) leads to an increase in the overall reluctance of the magnetic circuit. In this manner, rough adjustments to the dipole field can be achieved on a sector-by-sector basis. In other regions of the ring, steel shims will be added to the outside of the yoke in order to compensate for the various holes and penetrations that are required for items like vacuum feedthroughs, the inflector, etc.
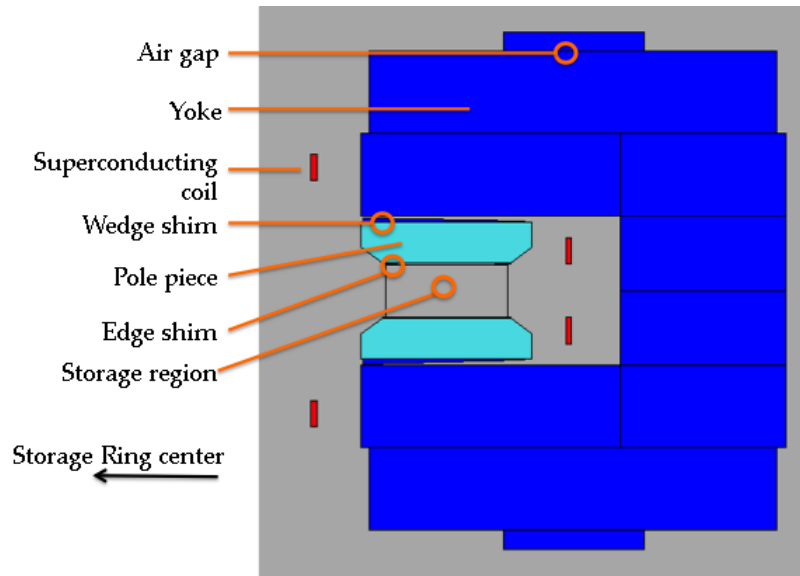
Figure 15.28: `OPERA-2D` model of the $g - 2$ magnet. The yoke and wedge shims are steel and shown in blue. The pole pieces (cyan) are made from ultra-low carbon steel (ULCS). The current in the superconductor coils is into the page for the inner coils and out of the page for outer coils.

**Pole Piece Alignment**     The Capacitec sensors mounted to the shimming trolley apparatus will measure the gap between the upper and lower pole pieces to a precision of $< 1$ $\mu$m. `OPERA-3D` simulations show that an increase in this gap size of 25 $\mu$m corresponds to a 250 ppm decrease of the dipole field [55]. A 50 $\mu$m change in the gap over the 56-cm radial extent of the pole corresponds to a change in the quadrupole moment of 120 ppm.

In E821 the gap height around the ring varied by $\pm 23$ $\mu$m rms, with a full range of 130 $\mu$m. Adjacent poles were matched to $\pm 10$ $\mu$m to reduce field distortions caused by discrete steps in the pole surfaces. Poles were leveled to $\pm$ 50 $\mu$rad using measurements from a precision electrolytic tilt sensor (see section on the radial field).

In E989 we will build a shimming trolley that is similar to the one used in E821 with a couple of upgrades. We plan to use several new copper-kapton thin-wand capacitive probes (Model GPS-7G-A-200-FX-5509-6108) instead of the button probes used in E821 which contained stainless steel. New quartz rods will be necessary to mount the probes and help provide the proper cable strain relief. A new set of 200Hz-BNC Dual Channel Linearized Capteura Amplifier Cards from Capacitec, Inc. will be used to read out these probes. The combination of these probes and amplifiers produce a linear output voltage in the range of 0 to 10V when the probe is a distance of 0 to 1.27 mm from the surface of interest. The quoted precision of this equipment allows a gap measurement precision of 0.07 microns. The overall temperature stability of these probes is 0.1 micron/degree Celsius, which is also improved with respect to the ones used in E821. The significantly improved temperature stability and uniformity of the experimental hall in E989 over E821 will help by reducing the size of thermal distortions, where changes of a few degrees Celsius change the gap by 10 $\mu$m or more due to thermal expansion of the steel. Finally, we intend to mount a vertical
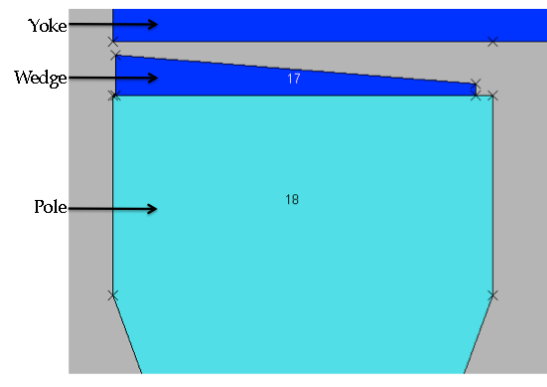
Figure 15.29: `OPERA-2D` model of the $g-2$ magnet, zoomed in on the air gap between the yoke and pole pieces. The wedge shims are radially adjustable.

plate to the shimming trolley at the inner radius in order to enable monitoring by a laser tracking system. This system will hold non-magnetic reflectors on the plate and use a series of optical interferometers that are standard instruments used by the metrology department. This system will provide the location of the shimming trolley in the coordinates of the storage ring, and will allow for a more automated feedback procedure when analyzing the shimming trolley NMR data. Recommendations can then be made for each sector as we iterate on the mechancial adjustments necessary to properly align the pole pieces. The combination of these various system upgrades will allow E989 to exceed the benchmarks achieved by E821.

**Wedge Shims**   Wedge shims are inserted into the 2-cm air gap between the pole piece and the yoke, as depicted in Figure 15.29. The gap is designed to isolate the high-quality precision pole pieces from the yoke steel, which contains some magnetic inhomogeneities. Each 30° sector contains 72 wedge shims, which are 9.86 cm wide (azimuthally) and 53 cm-long (radially)[50]. This is shorter than the 56 cm-long pole pieces (radially), to accommodate radial adjustments. At the inner radius, the wedge shims are 1.65 cm thick, while at the outer radius, they are 0.5 cm thick. Viewed from above, each wedge shim is rectangular. Thus the space between adjacent wedge shims increases as the radial coordinate increases.

    The angle of the wedge shims was calculated to be 20 milliradian in order compensate for the intrinsic quadrupole moment produced by the C-shaped magnet. Due to the asymmetry in the C-magnet, the field lines tend to concentrate in the gap near the return yoke. The dipole field is determined by the average thickness in the air gap above the storage region. The average wedge thickness is adjusted by translating the radial position of the wedge shims. Because of the shallow angle of 20 mrad, a radial movement by 50 $\mu$m changes the gap by 1 $\mu$m, allowing fine control for the dipole field. `OPERA-2D` simulations show that inserting the wedges into the air gap (towards the return yoke) radially by 50 $\mu$m produces a 5.4 ppm increase in the dipole field. The quadrupole and higher-order multipoles are each affected by less than 0.1 ppm for this adjustment. We will reuse the wedge-shims that were constructed for the E821 experiment. The angle correctly compensates for the intrinsic quadrupole of the C-shaped magnet, so we will just clean and refurbish these components.
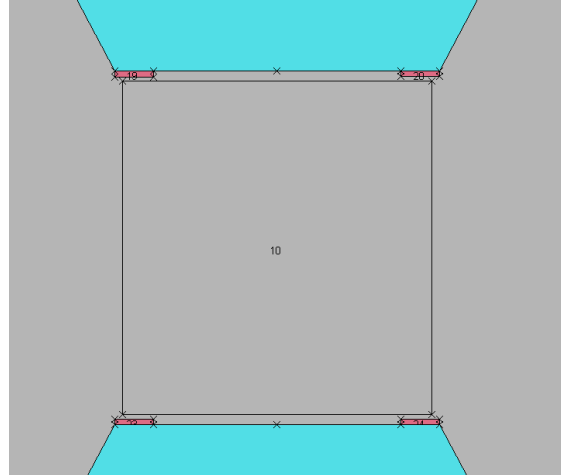
Figure 15.30: `OPERA-2D` model of the $g - 2$ magnet, zoomed in on the storage region. Edge shims are mounted on the pole pieces. "Inner" refers the shim at smaller radius (closest to the center of the ring), while "outer" refers to the shim at the larger radius (closest to the return yoke).

**Edge Shims**  Each of the 36 pole pieces has four removable edge shims mounted on the surface closest to the muon storage region, as shown in Figure 15.30. Each shim is 5 cm wide (radially), spans one pole piece (10° azimuthally), and is positioned at either the inner or outer edge of the pole faces. Variation of the thickness of the edge shims can produce predictable multipole corrections.

In E821, the shims were ordered oversized (3.2 mm for the outer shims and 4.4 mm for the inner shims) and then ground down to tune the quadrupole through octupole moments. A first pass was performed to uniformly grind the shims as a function of azimuth. In E821 a final pass was planned to optimize the thickness of the edge shims pole-piece-by-pole-piece, but this did not occur due to time constraints.

We have studied the effect of systematic shim thickness variations in `OPERA-2D`. Since the 2D model assumes vertical symmetry, the upper and lower edge shims are always adjusted simultaneously. Symmetrically increasing the thickness of both the inner and outer edge shims primarily affects the sextupole moment. `OPERA-2D` simulations helped us determine that a 100 $\mu$m increase in the edge shim thickness in all four corners increases the sextupole moment by 10.8 ppm. Asymmetric thickness adjustment leaves the sextupole moment unchanged and allows fine tuning of the quadrupole and octupole moments. Increasing the outer edge shim thickness by 100 $\mu$m while decreasing the inner edge shim thickness by the same amount increases the quadrupole and octupole moments by 13.2 ppm and 5.6 ppm, respectively. Although the simulation utilized vertical symmetry, this model can be extended to up-down and diagonal (skew) asymmetries.

We plan to use a similar shimming strategy in E989. An Ultra-Low-Carbon-Steel (ULCS) material called ARMCO Pure Iron is manufactured by AK Steel, and we have obtained a sample with dimensions 297 mm × 210 mm × 3 mm. It has excellent magnetic properties that are appropriate for the edge shim application: high permeability, uniformity, and
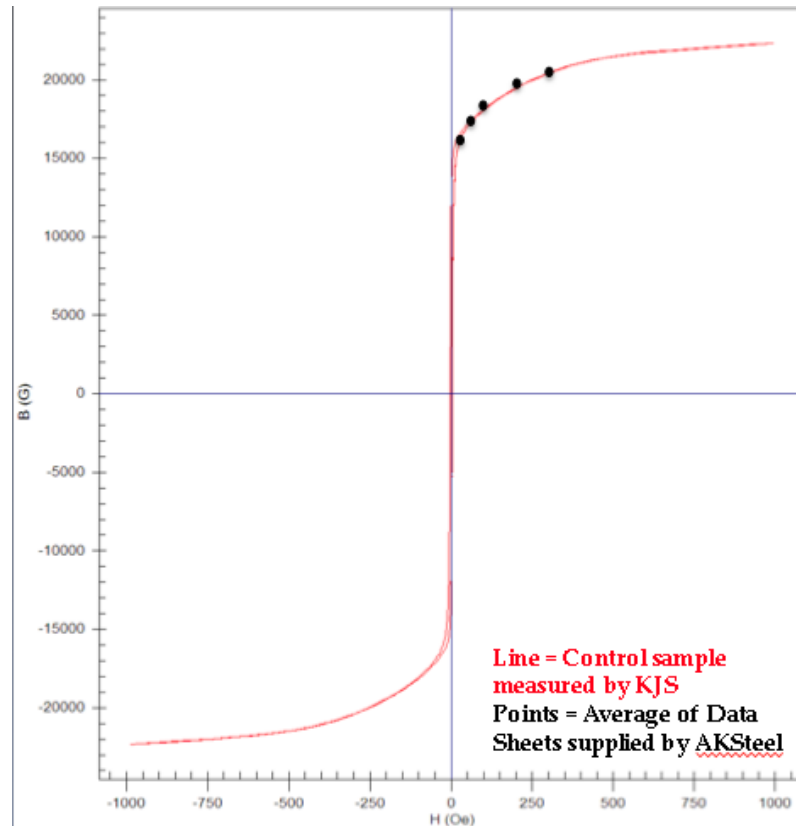
Figure 15.31: Test results of a control sample of ARMCO Pure Iron steel, manufactured by AK Steel and tested by KJS Associates. The measured B-H curve is shown in red and contains an uncertainty of 2%. The black data points correspond to the AK Steel data sheet for these samples, with an uncertainty of 1%. Additional tests of other samples showed expected reproducability.

machinability. We cut six small bars with volume 100 mm $\times$ 20 mm $\times$ 3 mm. Prior to sending them to KJS Associates for magnetic classification, we practiced introducing several types of machining stress: we ground off 200 micron from several samples, added countersunk holes, and additionally performed stress tests by hammering on the samples. Figure 15.31 show a sample B-H curve that has been characterized (red), as well as some black data points that come from the AK Steel data sheet. Ultimately, we found that the samples were relatively resilient against usual stresses. All samples were measured to have magnetization curves within the margin of error of the data sheet and measurement uncertainty [56]. Thus we will order oversized edge shims, map the field, calculate the appropriate thickness required, grind the shims, and iterate. Based on the experience of E821 and the extensive `OPERA` simulations, we believe this phase of the shimming will require only two iterations.

**Gap shims**   Significant variations in the magnetic field occur at the azimuthal boundaries between adjacent pole pieces, as shown in figure 15.32. The effect is even more pronounced at the pole piece surface than in the storage region, jeopardizing the effectiveness of the fixed
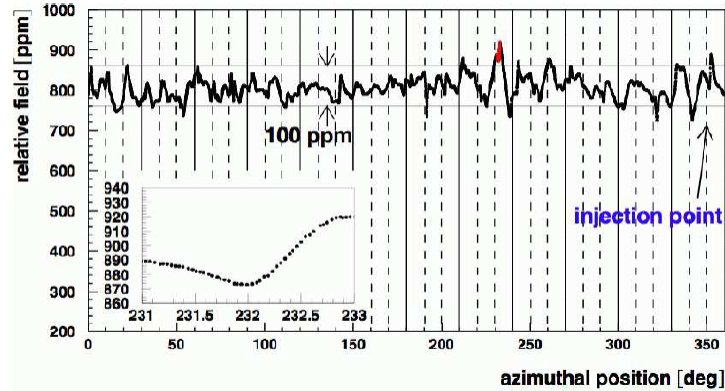
Figure 15.32: The magnetic field determined by the center NMR trolley probe versus azimuthal position in the storage ring during one trolley pass (reproduced from Ref [7]). The solid vertical lines denote boundaries between the 12 yoke sectors. The dashed vertical lines denote the pole piece boundaries.

probes located near the inter pole piece gaps. In E989, we plan to reduce the azimuthal variations in the field by shimming the gaps with thin iron plates. The basic concept is to span the surface of adjacent pole pieces with high quality steel plates varying from 10 to 100 $\mu$m. Simulations show that a local change of 10 $\mu$m in the air gap between the pole pieces results in a 40 ppm shift in the dipole field. This should be a fairly short range effect (azimuthally) that will reduce the local field gradients and improve the performance of the fixed NMR probes mounted in the vacuum chambers.

**Radial Field**

For E821, an auxiliary measurement of the radial component of the magnetic field was performed during the passive shimming phase prior to the installation of the vacuum chambers. In the storage region, the direction of magnetic field is principally vertical. The presence of a radial field component has a significant impact on the muon storage beam dynamics, affecting both the mean vertical position and the vertical betatron oscillations. Quantitatively, the radial field component needs to be measured to $\approx$ 10 ppm of the total vertical field. However, the NMR probes only measure the total magnitude of the magnetic field without providing information about the separate vertical and radial components. In E821 an auxiliary measurement using Hall probes was implemented to quantify the radial component of the field and we plan to repeat this procedure.

    Figure 15.33 shows a schematic representation of the E821 setup used to measure the radial field [39]. Two Hall probes (BH-206, F.W. Bell) were vertically aligned to measure the radial magnetic field, with the Hall currents running in the $z$ and $y$ directions. To ensure alignment of the setup with respect to the gravitational vertical direction, electrolytic tilt sensors (RG33A, Spectron Systems Technology, Inc.) were mounted to the support structure. Finally, to account for potential misalignment of the Hall probes with respect to the support structure, the measurements were repeated after rotating the entire structure by 180° about
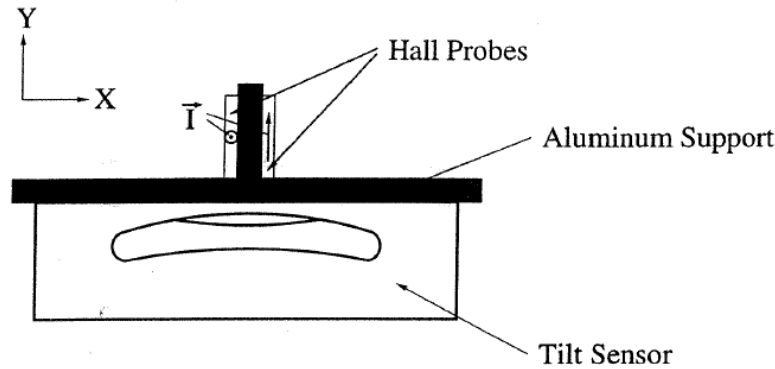
Figure 15.33: A schematic representation of the radial field measurement configuration in E821 [39]. Two Hall probes are mounted to measure the radial component of the field ($x$) with Hall currents oriented in the $z$ and $y$ directions. The rigid configuration is equipped with a tilt sensor. Rotating the entire setup 180° about the $y$-axis isolates the radial component.

the vertical axis and taking the difference of the Hall voltages.

Figure 15.34 shows the data from the Hall probes overlaid on the expected radial field determined from the multipole expansion of a field measurement. The overall precision of the radial field measurement was significantly better than the required 10 ppm. Figure 15.35 shows the radial field measurement (dots) from the Hall probe as a function of the azimuthal position around the ring. The line in this plot represents the measured pole tilt derived from the capacitive sensor data described above. The tracking of these two curves demonstrates the dependence of the radial field on the pole alignment.

### 15.8.3 Active Shims

Active shimming refers to the adjustment of current distributions to minimize any residual field non-uniformities that remain after the passive shimming is complete.

The principal active shimming controls consist of the following:

1. Control of the main superconductor current

2. Surface correction coils on printed circuit boards mounted between the pole face and the vacuum chamber

3. Dipole correction loops placed in the gap between the wedge shim and the yoke

4. Gap correction loops located in the azimuthal gaps between adjacent pole faces

**Main Current**

The central value of the dipole field is determined primarily by the current in the main superconducting coils. The nominal current is 5200 Amp per turn. `OPERA` simulations show

(a)                                                    (b)
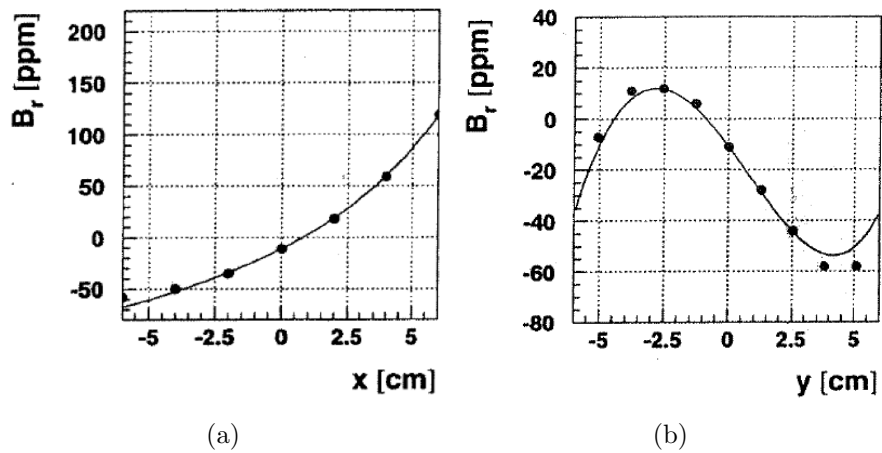
Figure 15.34: Radial component of the magnetic field in ppm as a function of (a) radial position $x$ and (b) vertical position $y$. The dots show the data from the Hall probe, while the solid lines represent the field variation expected from the multipole coefficients calculated from the absolute field measurement.
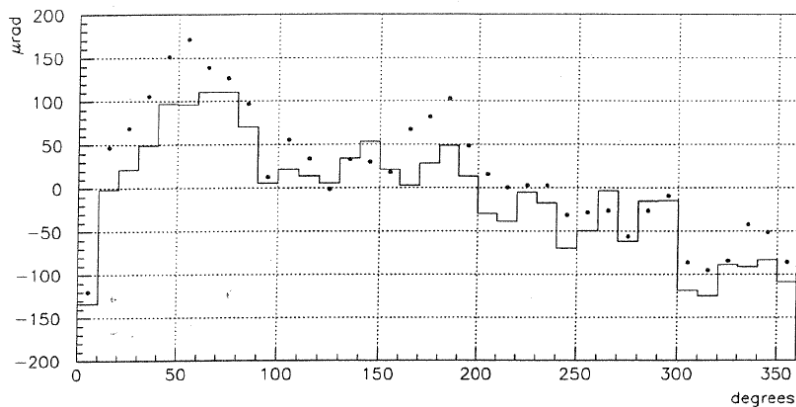


Figure 15.35: The radial field measurement (dots) from the Hall probe and the average pole tilt (line) from the tilt sensor are shown as a function of the azimuthal position around the ring.
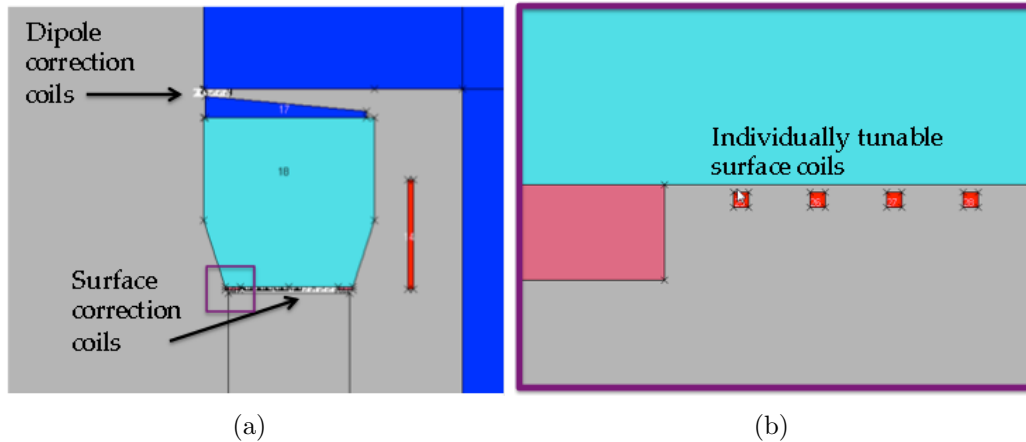
Figure 15.36: `OPERA-2D` depiction of the dipole correction coils and the surface correction coils. (a) Schematic overview showing the positions of the current traces on the printed circuit boards. The purple box is zoomed in and displayed in panel (b). Individual traces are adjusted to tune various multipole contributions.

that an increase of 1 A increases the field in the storage region by about 2 Gauss (140 ppm). During beam-on data collection periods, the field is monitored by the fixed NMR probes. The shape of the magnet gets distorted due to temperature variations which leads to a change in the magnetic field, so a feedback loop is utilized to stabilize the dipole field accordingly.

**Surface Correction coils**

Correction coils on the surface of the poles permit fine control of static, and slowly varying errors. The surface coils can be used to correct the lowest multipoles and adjust the field by up to tens of ppm, thus providing significant overlap between the iron shimming and the dynamic shimming. These coils have been constructed to generate moments over the entire 360° azimuth. The coils were designed with printed circuit boards, with 120 wires running azimuthally around the ring on the top and bottom pole surfaces facing the storage ring gap, and spaced radially 2.5 mm apart. The boards must be thin enough to fit between the pole faces and the vacuum chamber. With the pole-to-pole spacing of 180 mm and a vacuum chamber height of 165 mm, this allows up to 7.5 mm for each board and its corresponding insulation and any epoxy or glue that is necessary to affix the boards to the surface of the poles. We have studied the surface correction coils in `OPERA-2D` (see Figure 15.36) and verified that the expected residual multipole contributions can be compensated with the appropriately applied current distributions. One additional benefit of this system is that we can induce known multipole distributions in the NMR probe region and use the surface correction coils to help determine our position resolution of the trolley probes. A summary of the principal current distributions is shown in Table 15.8.3. E821 used these coils successfully to shim out the final few ppm for the higher order multipoles.

For E989, we plan to fabricate new printed circuit boards at Fermilab that extend over each of the 72 pole pieces. Each board should contain 100 azimuthally directed traces with

Table 15.5: Leading order current distributions as a function of the radial coordinate ($x$) that needed to correct for various multipole components, and the maximum range that can be corrected with less than 1 Amp. The currents are calculated at the fixed vertical position of the boards ($y = a = 9$ cm). Geometric and finite-size-effect corrections to the currents are necessary to compensate for residual higher order moments.

| Multipole | $K(x)(y = a)$ | Maximum range (ppm) |
|-----------|---------------|---------------------|
| Quadrupole | $a$ | 20 |
| Sextupole | $2ax$ | 10 |
| Octupole | $3ax^2 - a^3$ | 8 |
| Decupole | $4ax(x^2 - a^2)$ | 6 |

a radial spacing of 2.5 mm, and a length of one pole piece ($\approx 1.25$ m). The conducting elements should be positioned accurately to better than 50 $\mu$m in the radial direction. Since these boards will placed in the gap between the poles and the vacuum chamber, resistive heat dissipation is an important consideration. We wish to keep the total resistance per channel below 4 $\Omega$. At a maximum anticipated current of $\pm 2$ Amp/channel, this amounts to 16 W/channel, or 3.2 kW total power if operating all traces at the maximum current simultaneously. This would be an unusual, upper-limit implementation mode for the surface correction coils, as Table 15.8.3 indicates the radial dependence of the current necessary to tune individual moments.

Because these coils extend azimuthally around the entire ring, interconnects between adjacent boards must be designed. Low resistance (10 m$\Omega$), high quality blade connectors can be introduced at the union of adjacent boards. With 36 connectors, this only contributes 0.36 $\Omega$ to the total loop resistance per conductor. This additional resistance is taken into account when determining the design resistance for each trace. If necessary, multiple conducting layers at each radial position can be utilized in order to reduce the resistance to the appropriately low values. We will finish each board with a protective cladding covering the traces to provide electric isolation from the poles and vacuum chamber.

There are 36 upper poles and 36 lower poles. Overall, 70 of the surface coil boards have identical designs, and two boards (one upper and one lower) will be specialized in order to accommodate leads to the power supply boards. The external leads will be routed in a manner that minimizes the production of unwanted stray fields.

The baseline design for the power supplies for the surface correction coils derives from the design for the DECAM Heater Controller Crate used in the Dark Energy Survey [57]. The circuit specifications for that application are very similar, and allow us to build upon previous developments at Fermilab. The power supplies must be able to provide bi-directional, continuous DC currents of up to 2 Ampere for 200 total channels, with individual control of the current on each channel. The types of ICs utilized in the DECAM Heater board will be able to provide these currents without overheating, assuming the implementation of reasonably standard crate cooling. The SCC resistance will be $< 4\Omega$. Each trace on the surface correction coil amounts to a 7m-diameter circular loop, so our design calls for filters to help mitigate noise effects. In order to cancel higher-order magnetic field multipoles, fine tuning of the individual currents must be provided. To achieve 100 ppb resolution for those

moments, we need at least 5 mA resolution per channel. Over the dynamic range that the SCCs will need to shim, this requires a minimum of 10 bits for the DACs. We plan to use a 12-bit DAC to allow for finer resolution of the currents and better control of the magnetic field. A schematic of the DES Heater Controller Driver is included for reference in Figure 15.37. The specific components relevant to the $g - 2$ SCC are shown in the simplified block diagram in Figure 15.38.

We plan to use three standard 6U VME crates, each with 17 SCC driver cards, with 4 channels per board. Accounting for adequate cooling, each crate would require about 9U of rack space. Our baseline plan is to reuse available VME crates at Fermilab.

Table 15.6: A summary of design requirements for the Surface Correction Coils and associated Power Supplies

| Category | Specificiation | Comments |
|---|---|---|
| Number of Boards | 72 | 1 per pole piece; 2 specialty boards |
| Channel per Board | 100 | 200 total (100 upper, 100 lower) |
| Resistance per trace | $< 4 \ \Omega$ | Includes 36 blade connectors per channel |
| Channel spacing | 2.5 mm | Center channel at r=711.2cm |
| Current range | -2 A$<$I$<+$2 A | D C output, Each channel tuned separately |
| Current resolution | 5 mA | Controlled by DAC chosen |

As an alternative for the surface coils, we also investigated the possibility of routing channels in a G10 board and inserting 12-14 AWG wires for each of the traces. This alternative has the benefit of offering a very low resistance ($< 1 \ \Omega$ per conductor), but will limit the precision of the placement of the coils. The mechanical construction of the boards would also be more time consuming. Our baseline alternative is to route traces on a circuit board.

Finally, we will explore the option of using the reverse side of the boards for active current shims in the azimuthal gaps between adjacent pole pieces. The baseline design calls for using passive mechanical shims in these gaps instead, but the continued value engineering efforts will revisit this issue.

**Dipole correction loops**

The "continuous" ring was built with 10° pole sections, 36 of which form an almost continuous ring. Dipole correction coils were located in the air gaps of each 10° pole of the E821 storage ring, as depicted in Figure 15.36 (a). These coils consisted of 50 turns of copper wire wound in a rectangular shape. The dipole correction coils were capable of tuning each pole section independently, but were not used. Instead E821 used an active NMR feedback loop to stabilize the overall field by adjusting the main superconductor current. It is possible that the field in E989 could be stabilized in each pole piece separately by using the local NMR feedback to adjust the dipole correction currents. This would be particularly useful if temperature gradients over the 14 m diameter ring lead to different field distortions in different locations. However, given the much improved thermal stability and uniformity in MC-1 over E821, it is unlikely the dipole correction loops will be required.

Figure 15.37: A schematic of the circuit used for the DES Heater Driver Board.

Active Current Shim Driver Channel (2-4 Channels per PC Board)

12-bit DAC

VME Interface Control/Status Registers

V-control Input Filter

V-control Buffer/Amp

I-out Direction Amp

Bi-Directional Output Driver

Output Filter

Bi-Directional Output Driver

I-out (pos)

I-out (neg)

V-control = 25 mV per 5 mA Output Resolution
2.0 Amps Output Maximum
Over Current/Over Temperature Protection
Power Dissipation = 5 to 10 W per channel

Title: **Active Current Shim, Driver Channel Simplified Block Diagram**
Project: Muon g-2 | Drawn: Steve Chappa | Date: 05-13-2014 | Sheet: 1 of 1 | Rev: A

Figure 15.38: A simplified block diagram used to lay out the requirements of the Surface Correction Coils.

**Gap correction loops**

We want to minimize the azimuthal variation of the magnetic field, as explained in Section 15.8.2. Thus, E989 will use `OPERA-3D` to study the possibility of adding small loops to the bottom of the surface correction coil boards at the azimuthal positions between adjacent poles. We would primarily have control over the dipole moment, with limited ability to modify the higher order multipoles.

### 15.8.4 E821 results

E821 successfully implemented many of the passive and active shimming techniques described above. Table 15.8.4 shows the historical progression of the uniformity of the field as a function of time during the commissioning phase of the experiment. As they adjusted shims closer to the storage region, the higher order multipoles became more controlled. The final column shows the principal changes that were implemented at that step. We plan to use this experience to compress the shimming schedule for E989.

Table 15.7: Quadrupole (Q), Sextupole (S), Octupole (O), and Decupole (D) multipoles, broken down into normal(n) and skew(s) components, in ppm, evaluated at the storage radius ($r = 4.5$ cm).

| Date | $Q_n$ | $S_n$ | $O_n$ | $D_n$ | $Q_s$ | $S_s$ | $O_s$ | $D_s$ | Action |
|------|-------|-------|-------|-------|-------|-------|-------|-------|--------|
| Jun 1996 | -169.12 | 112.03 | -34.16 | 23.71 | 27.06 | 5.82 | 3.12 | 0.46 | Initial configuration |
| Nov 1996 | 5.52 | 3.19 | -1.11 | 1.95 | 9.13 | 5.32 | 0.85 | 0.45 | Edge shims ground uniformly |
| Jul 1997 | 5.26 | 2.94 | -1.03 | 1.45 | 12.26 | 2.78 | 0.36 | 0.25 | Edge shims ground in each pole piece+ pole alignment |
| Aug 1998 | 7.73 | -5.29 | -2.79 | 0.38 | -2.07 | -0.02 | -0.25 | 0.71 | Final passive shimming |
| Sep 1998 | -2.54 | -1.25 | -2.70 | 0.34 | -2.39 | -0.18 | -0.28 | 0.42 | Active shimming commissioned |
| PRD | 0.24 | -0.53 | -0.10 | 0.82 | 0.29 | -1.06 | -0.15 | 0.54 | Publication |

## 15.9   Value Management and Alternatives

We are realizing significant savings in the magnetic field measurement system by refurbishing as much of the E821 hardware as possible, rather than building a completely new system. At the same time, we are making improvements (such as the change to the NMR sample

material, improved shimming and magnet temperature control, improved calibration appa-
ratus, ...) that improve operational characteristics and reliability, and which are necessary to
reach our goal of an uncertainty on $\omega_p \leq 70$ ppb. Some examples of the various alternatives
that are considered and the value management principles used to make down-selections are
highlighted here.

## Probes

The determination $a_\mu$ in terms of $\omega_a/\omega_p$ and $\mu_\mu/\mu_P$ requires the storage ring magnetic field be
measured in terms of the muon distribution weighted free proton precession frequency, $\omega_P$. In
principle this could be done by injecting a 3.1 GeV/$c$ polarized proton beam into the storage
ring with a proton spin analyzer (polarimeter) in the ring based on the spin dependence of
$p$-carbon elastic scattering. The anomalous precession frequency would be close to 40 MHz,
and the phase space of the protons and muons would have to be matched or measured to mm
precision. Proton beam measurements of the field distribution would have to alternate with
muon injection. Developing a polarized proton source, 3.1 GeV/$c$ accelerator, polarimeter,
proton beam position monitoring hardware etc. would add significant cost and technical
challenge to the experiment, and it is not clear that the field determination could be made
to 70 ppb. Further, during periods of muon injection, an NMR-based system of fixed probes
outside the storage volume would still be required to monitor the field and provide feedback
to the power supply to stabilize the field. A similar NMR system would be required to shim
the magnet.

Other field measurement technologies such as Hall probes have been considered. One
advantage is that a 3-axis device could make separate measurements of $B_x$, $B_y$, $B_z$. However,
Hall probes have a significant temperature dependence ($\sim 10$ ppm/$^\circ$C), resolutions at the
1 ppm level (versus 20 ppb for NMR), and fluctuating offsets. Commercial technology is
currently inadequate for the level of accuracy sought in E989. Further, they would require
frequent calibration in terms of an equivalent free proton precession frequency, so an NMR-
based absolute calibration probe would still have to be developed and tested.

Finally we note that pulsed NMR is preferred over CW techniques since the latter typ-
ically requires a small field modulation coil that perturbs the local field, introduces image
fields in the iron poles and yokes, and is potentially difficult to calibrate at the precision
sought in E989. In addition, the lineshape analysis required in CW techniques to achieve
ppb levels of precision is substantially more difficult than the analysis methods required for
analyzing pulsed NMR FIDs. Newer approaches replace the field modulation with frequency
modulation, but still must deal with the time constants of the probes and of the samples,
and still need a sophisticated signal analysis to determine the resonance frequency precisely
from the time domain response.

## Trolley

We are investigating improvements with respect to systematic uncertainties by changing the
size and shape of the trolley probes. Smaller probes could allow positioning of the probes
to slightly larger radii and hence improve the determination of higher multipole moments of
the magnetic field. However, the expected gains need to be understood to verify such change

as the current probes are certainly already close to optimal.

A major alternative could be the design of a new trolley system with much reduced onboard functionality. Given the crucial role of this system in the g-2 experiment, a replacement of the existing trolley would eliminate such single point of failure. In this alternative version, the onboard electronics would ideally be reduced to only host the multi- and duplexer, a preamplifier, and a small control unit including some of the sensor functionality (temperature, pressure, position measurement). This scheme requires that the NMR analog signal can propagate with minimal distortion over the 45-m-long co-axial cable to the outside of the vacuum where electronics for frequency determination would be located. Similarly, the RF pulse would be sent to the trolley from the outside eliminating the need of the RF amplifier onboard. The processing of the NMR signal could then happen analogously to the fixed probes in the proposed new readout system with full digitization. However, such an alternative development would require major cost and labor resources and the actual implementation has to be based on a more detailed cost-benefit-analyses. Thus our baseline calls for refurbishing the existing E821 trolley and a new trolley system remains a risk/alternative.

## Absolute Calibration

The baseline plan for the absolute calibration involves using reusing the spherical water sample that has been used in the Brookhaven $g - 2$ experiment, as well as the E1054 experiment that determined the ratio $\mu_\mu/\mu_p$. An alternative going forward is to develop a polarized $^3$He sample instead of water. This alternative benefits from lower uncertainty in the diamagnetic shielding factor, reduced sensitivity to some geometric effects, and a much smaller temperature coefficient. The addition of the $^3$He calibration system would provide a valuable cross-check of the spherical water probe, and thus remains a viable alternative going forward, as described in section 15.4.2.

## Shimming

The magnet shimming team has decided to refurbish equipment wherever possible. This includes reusing most of the shim kits from the E821, including the iron pieces on the yoke, the poles, and the wedge shims. New edge shims are being ordered to provide the flexibility required to tune the residual sextupole and octupole moments that remain after the rough shimming procedure.

One alternative that remains involves the possibility of reusing the existing edge shims. A significant amount of rust has formed in a non-uniform manner across the exposed face of some edge shims, so these would likely need to be resurfaced. The inevitable reduction in the total magnetic thickness of these shims would require the addition of very thin steel shims on top of the existing edge shims. We have identified a variety of vendors that have 1-mil thick AISI 1008 shim stock that could be appropriate for this application, at a cost as low as $2.5 per sq-ft. We need to investigate the magnetic uniformity of the candidate material and ensure that we can securely fasten these foils to the existing edge shims. In the case that we need thinner edge shims to correct a higher order multipole, we have also simulated the possibility of adding non-magnetic (or low-magnetic) spacers between the pole pieces and edge shims. We have found that this has an effect that is proportional to the reduction of the

thickness of the edge shims. One concern with this method is that the steel screws that fasten the edge shims to the poles would create magnetic shorts that could produce non-uniform effects, so the ability of this method to meet the technical uniformity requirements has not been verified. Further value engineering will be applied to see if we can reduce the cost of the edge shim system without jeopardizing the technical requirements by employing these low-costs methods. Our current baseline calls for repeating the E821 method of ordering oversized edge shims and then grinding them to the appropriate thickness.

A final example of value management in the shimming system comes from the Surface Correction Coils. The driver boards for these coils are based upon the design for the Dark Energy Survey's DECAM Heater Controller Board. Our engineers identified many similarities between our requirements and these existing boards, and plan to use that as a base design for our system.

**Test Magnet**

The HEP division at Argonne has acquired a 4T solenoid magnet (see Section 15.3.9). This solenoid has a measured stability of better than 0.1 ppm/hour, a shim set for ppm-level homogeneity over a 10 cm diameter volume, and a 680 mm bore diameter, essential for extensive performance tests of the NMR trolley in advance of installation in the $g - 2$ storage ring. We will also perform systematic studies of the absolute calibration probe in this magnet. They will also be essential for determining the magnetic influence of the calorimeter and tracker hardware on the storage ring field. The acquired magnet has replaced the original option of bringing a 1.5 T solenoid from Los Alamos. The decision basis for this 4 T option were reduced costs for the transfer and installation, and expected lower operational costs. The system was also readily available leading to a shorter time until it is fully operational for the essential systematic tests of the NMR equipment.

# 15.10   ES&H

The trolley garage, which is part of the field monitoring system, is a vacuum vessel. Lasers are used during survey/alignment activities and calibration activities. The storage ring magnetic field is at 1.45 T and has a strong fringe field in the interior of the ring. The hazards encountered in the field monitoring operation are therefore Laser Hazards, Vacuum Vessel Hazards, and High Magnetic Field Hazards. Engineering review will determine the necessary requirements on the vacuum vessels. Job Hazard Analysis will be performed for any testing, installation, or operational task that involves personnel working in the high field environment or using lasers.

In addition there will be three or four 19" racks of field measurement electronics. These will typically draw a few kW of power each, and do not produce high voltages or large currents. All personnel working on this equipment will be trained to ensure safe operation.

# 15.11 Risks

**Fixed Probe System**

The fixed probe system is essential for field monitoring during data taking. The technology required to monitor the field at the required level already exists so the risks are primarily in two other categories; (1) the risk that the refurbishment of the fixed probe system can not be completed on time, (2) the magnet stability is worse than anticipated.

The refurbishment of the fixed probe electronics requires that new preamplifiers for the NMR signal and a new RF pulse amplifier must be found since the vendors for the E821 components are not in business. These risks are minor or non-existent as new candidate components (with higher performance in some cases) have been identified and will be tested. The risks to the schedule come primarily from the time and effort required to refurbish the roughly 400 fixed probes and the NIM crate and multiplexer electronics. The mechanical work on the fixed probes can be distributed to additional university or laboratory machine shops so it may be done in parallel. Filling the samples and tuning the probes can also be done in parallel by any group with a vector impedance meter or network analyzer. In E821 such work was done by undergraduates. If the electronics work falls behind schedule, it can also be done in parallel at the Electronic Design Facility at Boston University, at Argonne, or Fermilab once new boards have been designed.

The second risk regarding magnet stability is more serious but unlikely as the new building is designed specifically for magnet stability. If the anticipated gains in magnet stability do not materialize, additional insulation can be applied around the magnet and on the experimental hall floor. If necessary, an inexpensive, easily installed and removed thermal enclosure from aluminum framing and foam board insulation can be constructed.

**Absolute Calibration System**

The calibration of the trolley probes requires that the absolute calibration probe and plunging probe and their positioning systems have been extensively tested. The risks here are that the probes are damaged, and that the system does not perform to specifications.

If the calibration probes are damaged, they can be be remade. The most delicate part is the highly-spherical glass bulb used in the absolute calibration probe. This part has survived nearly 20 years already, and the vendor, Wilmad LabGlass has already been contacted regarding making replacements. Spare absolute calibration probes will be prepared for E989, and ready for use long before data-taking.

The risk that the new calibration system does not perform to specifications is small. The changes from E821 are relatively minor but should be effective (primarily adding motion in the azimuthal direction for the plunging probe, adding a closed loop positioning system, and better determination of the precise location of trolley probe active volumes). These systems involve little technical risk and their performance can be tested thoroughly before the experiment takes data. The worst schedule risk is losing roughly 2-3 weeks of muon data. If the calibration system is not ready when the experiment starts, muon data can still be taken while the calibration system is being prepared. When the system is ready, roughly 2-3 weeks of muon data would be lost for installation as it would involve letting the vacuum chambers up to air, installing the system, testing it, and pumping back down.

**Trolley**

The trolley and its associated mechanics are a central piece in the measurement of the magnetic field of the storage ring. A major risk would be the partial or complete failure of the onboard electronics. Depending on the severity of the failure mode, the consequences could range from a replacement of the broken component, a redesign of parts of the electronics up to the need of a complete redesign of the trolley electronics. While the probability is low for this to happen, a realization of this risk could have both significant cost and schedule impact. Mitigation of the risk is hence important. It involves careful refurbishment of the system with guidance from former experts as well as the refurbishment of both existing trolleys so that both are fully operational. For that purpose, we bring together a group of current E989 and former E821 collabortion members and the electronics engineer from Heidelberg in June at Argonne National Laboratory. During the 9 days of scheduled work together, we will carefully learn how to communicate with the central microcontroller and transfer the knowledge to the new collaborators that are in charge of this system.

Damage of the trolley garage or drive mechanism during the shipping was prevented by careful packing. Immediate mechanical inspection and testing of both devices at Argonne have shown no indication of any mechanical shortcomings so that we were able to retire these risks. Of course, final shipment to Fermilab for installation at the experimental hall will be handled in a similar careful way.

Another risk is associated with the position measurement upgrades to determine the longitudinal position of the trolley during its data taking. There is a small possibility that the anticipated upgrade of the barcode reader does not succeed because of remaining overheating or other unforeseen issues. In the case of this event, alternative solutions must be sought to meet the requirements. To mitigate this risk, we are currently building a stand-alone prototype barcode reader. With it, we can test early that the replacement barcode reader will work with the barcode marks and in vacuum.

**Shimming**

The shimming procedure used in E821 has been examined and provides the basis for shimming the field in E989. Careful review of past safety procedures will be necessary to ensure the successful, safe shimming of the field. An examination of associated risks reveals two main categories of risks associated with the shimming procedure: damage to equipment and delay of the experiment. To mitigate each category, we will begin as early as possible with a well-formulated plan.

Damage during shipping is a risk for the yoke, poles, wedge shims, edge shims and dipole correction coils. To address this risk, we have shipped most of the steel well in advance of the installation in the experimental hall at Fermilab. If there were any unexpected accidents in transit or during the installation of the steel in the hall, this would allow us the necessary time to order replacements for these parts. Additionally, there are ongoing risks to the materials during both the shimming procedure and the subsequent running due to the enormous energy stored by the $g-2$ magnet. The stray fields are significant enough to attract loose ferromagnetic materials in the experimental hall towards the steel. These pieces could potentially impact and damage the precisely manufactured surfaces of the shims

and poles, causing major distortions to the field but more seriously, posing a significant risk to human safety. To address these issues, we will follow safety procedures to ensure that no loose magnetic materials are left in the hall when the ring is powered. We will check that the shims are securely fastened to the pole and yoke pieces. We will continue to examine the forces on the various screws and bolts in simulations to ensure that sufficient safety factors are utilized. In all cases, following disciplined safety procedures will prevent potentially damaging incidents with both people and equipment.

The shimming procedure calls for ordering oversized edge shims and then grinding them down to the appropriate thickness. There is a schedule risk associated with grinding off too much material. We would then need to reorder the shims and recommence the grinding step of the shimming, which would delay meeting our shimming goals. To mitigate this we will continue to compare our simulation results with past experience to get a solid understanding of the dependence of the multipole moments on the shim thickness. We will proceed with a conservative plan to grind in a couple of iterations, so as to prevent "overshooting" the required thickness. A technique of stacking thin steel foils on the edge shims is being investigated as both an alternative to ordering new shims and as a potential mitigation technique for the possibility of overgrinding.

A schedule risk would be realized if the shimming procedure fails to achieve the required uniformity. This could occur in a variety of ways, for example if detector systems introduce large, non-symmetric distortions to the field or if the finite-size effects of surface coils limit our fine tuning ability. If we do not achieve our uniformity goals, we would have to make improvements in other areas - namely, better knowledge of the probe positioning, better absolute calibration and better temperature control. To address these issues, we will continue to study the magnet in `OPERA` and advance the simulation plans. We will get an early start on the fabrication of the printed circuit boards, and understand their requirements and technical capabilities. We will also remain involved with the other teams to ensure their systems do not introduce unmanageable distortions to the field, due to either materials or currents. A test stand with an $\approx 1.45$ T field is under development at ANL, and will be available to test proposed systems in advance. These steps will help ensure that the uniformity goals are achieved.

**Other Performance Risks**

Many of the risks that would prevent us from achieving the uncertainties outlined in Table 15.1 can be mitigated by spending enough time on trolley runs and trolley calibration so the goals are met. These activities will often conflict with data-taking which reduces the statistical uncertainties on $\omega_a$. A balance between these activities will be established that brings the uncertainties down on $a_\mu$ most efficiently. This will depend on actual event rates and magnet stability. If the storage ring dipole and quadrupole fields are at least a factor of two more stable than E821, and if the field measurement hardware and shimming performance goals outlined above are met, the target for the precision of $\omega_p$ should be achievable without major risks to the schedule.

## 15.12   Quality Assurance

It is necessary to test the NMR hardware before shimming and installation in the g-2 storage ring. This requires the development of independent test-stands that include a set of NMR probes, NMR electronics, DAQ, and a magnet. We have located at least 4 magnets suitable for these purposes, where the requirements on the magnet depend on the hardware component being tested.

To test the fixed probes requires a vector impedance meter or network analyzer and a magnet at 1.45 T with field gradients less than 20 ppm/cm. The latter is sufficient to ensure an FID of millisecond duration, sufficient to confirm the probe works. An electromagnet suitable for testing fixed probes and basic functioning of the NMR hardware has been prepared during 2013 at the University of Washington.

Precision tests of the NMR hardware - such as single shot frequency resolution, temperature dependence of NMR signals, reference frequency dependence of the electronics, aging effects, measurements of $T_2$, etc. require magnets with stability of 10-100 ppb per hour and field gradients of <200 ppb/cm. Such a magnet is available to the group at University of Michigan (with access to a large bore persistent mode MRI magnet). The University of Massachusetts group has unrestricted access for several years to a small bore (89 mm) persistent mode superconducting magnet from Cryomagnetics, with better than 0.01 ppm/hr stability and a shim set to achieve sub-ppm/cm homogeneity over an 8 cm$^3$ volume. The small bore cannot accommodate the E989 NMR probes (it can only accommodate the plunging probe), but many sensitive tests of the NMR electronics and behavior of the NMR probe samples (temperature effects etc.) can be measured at the 10 ppb level using custom probes.

A critical test magnet system has been shipped to ANL and is in the process of being commissioned. This persistant-mode, large bore superconducting MRI magnet will facilitate the testing of equipment directly related to the field measurement, as well as equipment from other groups that runs the risk of adversely affecting the magnetic field. The proximity of this test facility near Fermilab is an important step that will allow quick feedback on candidate prototypes and will see regular use during the buildup of the experiment.

Extensive early testing of the NMR hardware will allow the identification of problems and the implementation of solutions in advance of installation in the g-2 ring. By having several absolute calibration probes, repeated calibration of the trolley probes, and extensive investigations of potential systematics, we intend to produce a robust result on $\omega_p$.

# References

[1] P. J. Mohr, B. N. Taylor, and D. B. Newell, Rev. Mod. Phys. **84**(4), 1527 (2012).

[2] D. Hanneke, S. Hoogergeide, and G. Gabrielse, Phys. Rev. A **83**, 052122 (2011).

[3] W. Liu *et al.*, Phys. Rev. Lett. **82**, 711 (1999);

[4] A. Mooser *et al.*, Nature **509**, 596 (2014).

[5] R. Prigl, *et al.*, Nucl. Inst. Methods Phys. Res. **A374** 118 (1996).

[6] X. Fei, V. Hughes and R. Prigl, Nucl. Inst. Methods Phys. Res. **A394**, 349 (1997).

[7] G. Bennett, *et al.*, (Muon $(g-2)$ Collaboration), Phys. Rev. **D73**, 072003 (2006).

[8] Ralf Prigl, doctoral thesis, University of Heidelberg (1994).

[9] Alex Grossmann, doctoral thesis, University of Heidelberg (1998).

[10] Huaizhang Deng, doctoral thesis, Yale University (2002).

[11] A. Abragam, *Principles of Nuclear Magnetism* (Oxford Univ. Press, New York, 1961).

[12] C.P. Slichter, *Principle of Magnetic Resonance* (Springer-Verlag, New York, 1989).

[13] J.L. Flowers *et al.*, IEEE Trans. Instrum. Meas. **44**, 488 (1995).

[14] W.D. Phillips *et al.*, Metrologia **13**, 179 (1977).

[15] Yu. Neronov and N. Seregin, Metrologia **51**, 54 (2014).

[16] B.W. Petley *et al.*, Metrologia **20**, 81 (1984).

[17] J.A. Osborn, Phys. Rev. **67**, 351 (1945).

[18] J.L. Flowers *et al.*, Metrologia **30**, 75 (1993).

[19] P.F. Winkler, D. Kleppner, T. Myint, and F.G. Walther, Phys. Rev. **A5**, 83 (1972).

[20] W.E. Lamb Jr., Phys. Rev. **60**, 817 (1941).

[21] H. Grotch and R.A. Hegstrom, Phys. Rev. **A4**, 59 (1971).

[22] S.G. Karshenboim and V.G. Ivanov, Phys. Lett. B **566**, 27 (2003).

[23] B.W. Petley *et al.*, Metrologia **20**, 81 (1984).

[24] Y.I. Neronov and A.E. Barzakh, Sov. Phys. JETP **48**, 769 (1978).

[25] J.S. Philo and W.M. Fairbank, J. Chem. Phys. **72**, 4429 (1980).

[26] R. Hoffman, J. Magn. Reson. **178**, 237 (2006).

[27] G.T. Danby and J.W. Jackson, E821 Muon $g-2$ Internal Note No.1, 1(1987).

[28] K. Woodle, E821 Muon $g-2$ Internal Note No.44, 1(1990).

[29] S. Redin, E821 Muon $g-2$ Internal Note No.51, 1(1990).

[30] X. Fei and V.W. Hughes, E821 Muon $g-2$ Internal Note No. 86 (R), 1(1991).

[31] M.J. Fischer, E821 Muon $g-2$ Internal Note No. 114, 1(1992).

[32] Y.K. Semertzidis, C.S. Lin, and W.M. Morse, E821 Muon $g-2$ Internal Note No.155, 1(1993).

[33] E989 $g-2$ DocDB notes 345, 396, 1261, 1773, 1775.

[34] N. Kinnaird, J. Mott, B.L. Roberts, g-2 note #66, DocDB note 2864, June 2015.

[35] Energy Extraction Time Constant Revisited. E821 Note 122.

[36] Nicholas Kinnaird and James Mott, Muon g-2 Note xxx, DocDB xyzx, 2015.

[37] G.T. Danby and J.W. Jackson, E821 Muon $g-2$ Internal Note No.180, 1(1993).

[38] OPERA. Cobham Technical Services, Vector Fields Software, 1984-2012.

[39] R. Prigl, E821 Muon $g-2$ Internal Note, $g-2$ DocDB note 947.

[40] R. V. Reid, Phys. Rev. A, **11**, 403 (1975).

[41] M. A. Bouchiat, T. R. Carver, and C. M. Varnum, Phys. Rev. Lett. **5**, 373 (1960).

[42] T.E. Chupp, K.P. Coulter, Phys. Rev. Lett. **55**, 1074 (1985); M. E. Wagshul and T. E. Chupp, Phys. Rev. A **40**, 4447 (1989).

[43] F.D. Colegrove, L.D. Schearer, G.K. Walters, Phys. Rev. **132** 2561 (1963).

[44] A. Nikiel-Osuchowska *et al.*, Eur. Phys. J. D **67**, 200 (2013).

[45] M. S. Rosen, T. E. Chupp, K. P. Coulter, R. C. Welsh, S. Swanson, Rev. Sci. Instrum. **70**, 1546 (1999).

[46] S.R. Nuss-Warren et al., Nucl. Inst. Meth. A **533**, 275 (2004).

[47] S. D. Swanson, M. S. Rosen, B. W. Agranoff, K. P. Coulter, R. C. Welsh, T. E. Chupp, Magn. Reson. Med. **38**, 695 (1997).

[48] M. Abboud, A. Sinatra, X. Maitre, G. Tastevin, P.-J. Nacher, Europhys. Lett., **68**, 480 (2004).

[49] M. Abboud, PhD thesis, "Pompage optique de lhlium-3 forte pression dans un champ magntique de 1.5 Tesla", University of Paris VI (2005).

[50] G.T. Danby *et al.*, Nucl. Inst. Meth. A **457**, 151 (2001).

[51] B. Cowan, Meas. Sci. Technol. **7**, 690 (1996).

[52] S.I. Redin *et al.*, Nucl. Inst. Meth. A **473**, 260 (2001).

[53] E. Efstathiadis *et al.*, Nucl. Inst. Meth. A **496**, 8 (2003).

[54] H. Deng *et al.*, E821 Muon $g-2$ Internal Note No. 432, 1 (2003).

[55] OPERA-3D Simulation of Misalignment. $g-2$ DocDB note 1121.

[56] ARMCO Pure Iron Material Analysis. $g-2$ DocDB note 1891.

[57] DECAM Heater Controller Crate User Manual. DES DocDB note 6026.